Electronic Thesis and Dissertation Repository

4-14-2016 12:00 AM

Arthrokinematics of the Distal Radioulnar Joint in the Normal Wrist and Following Distal Radius Malunion

Braden M. Gammon
The University of Western Ontario

Supervisor
Dr. Graham King
The University of Western Ontario Joint Supervisor
Dr. James Johnson
The University of Western Ontario

Follow this and additional works at: https://ir.lib.uwo.ca/etd

Part of the Medical Biophysics Commons

Recommended Citation

Abstract

Contact patterns in the distal radioulnar joint (DRUJ) are not well understood for normal anatomy or with distal radius deformity. This thesis presents three studies which investigate the arthrokinematics of the DRUJ for these conditions. The first study compared casting and Tekscan, two standard methods for contact measurement, with a novel technique of proximity mapping termed Inter-cartilage Distance (ICD). The relative benefits, limitations and role for ICD in DRUJ contact assessment were examined and discussed. The second study used ICD to characterize contact patterns in the native DRUJ. Contact was found to be maximal in 10° of supination and the contact centroid moved volar and proximal with supination. The third and final study evaluated the effect of dorsal angulation deformity on DRUJ arthrokinematics. The contact centroid moved volarly, while simulated triangular fibrocartilage complex (TFCC) rupture reduced DRUJ contact area and caused the centroid position to become more variable in its pathway.

Keywords: Arthrokinematics, distal radioulnar joint, DRUJ, triangular fibrocartilage complex, TFCC, ulnar head, sigmoid notch, distal radius malunion, fracture, deformity, wrist, forearm, kinematics, biomechanics, Tekscan, casting, Inter-cartilage Distance, ICD, proximity mapping, *in vitro*, simulator

Co-Authorship Statement

Chapter One
Sole author – Braden Gammon
Manuscript Review – Graham King, Jim Johnson

Chapter Two
Study Design – Braden Gammon, Emily Lalone, Graham King, Jim Johnson
Specimen Preparation – Braden Gammon
Data Collection – Braden Gammon, Mark Welsh
Data Analysis – Braden Gammon, Emily Lalone, Ryan Willing
Statistical Analysis – Braden Gammon
Manuscript Preparation – Braden Gammon
Manuscript Review – Emily Lalone, Graham King, Jim Johnson

Chapter Three
Study Design – Braden Gammon, Emily Lalone, Graham King, Jim Johnson
Specimen Preparation – Braden Gammon, Masao Nishiwaki
Data Collection – Braden Gammon, Mark Welsh, Masao Nishiwaki
Data Analysis – Braden Gammon, Emily Lalone, Ryan Willing
Statistical Analysis – Braden Gammon
Manuscript Preparation – Braden Gammon
Manuscript Review – Emily Lalone, Graham King, Jim Johnson

A version of this manuscript will be submitted to the Journal of Hand Surgery (American) entitled: *In Vitro* Arthrokinematics of the Intact DRUJ
Authors: Gammon B, Lalone E, Willing R, Nishiwaki M, Johnson J, King GJW

Chapter Four
Study Design – Braden Gammon, Emily Lalone, Graham King, Jim Johnson
Specimen Preparation – Braden Gammon, Masao Nishiwaki
Data Collection – Braden Gammon, Mark Welsh, Masao Nishiwaki
Data Analysis – Braden Gammon, Emily Lalone, Ryan Willing
Statistical Analysis – Braden Gammon
Manuscript Preparation – Braden Gammon
Manuscript Review – Emily Lalone, Graham King, Jim Johnson

A version of this manuscript will be submitted to the Journal of Hand Surgery (American) entitled: The effect of Dorsal Angulation Deformities on *In Vitro* Arthrokinematics of the DRUJ
Authors: Gammon B, Lalone E, Willing R, Nishiwaki M, Johnson J, King GJW

Chapter Five
Sole author – Braden Gammon
Manuscript Review – Graham King, Jim Johnson

Acknowledgments

Dedication

This manuscript is dedicated to my beautiful, loving, patient wife Jessica and our sons Liam and Kai, who are the pride and centre of our lives. I have "refined" this thesis over the course of 3+ years and it has diverted my attention on many evenings and weekends. Throughout this time they have remained sympathetic, encouraging and supportive. Its completion is a combined achievement that we will all celebrate with pride.

I would also like to pay a sincere tribute to the late Dr. Jim Roth.   I was fortunate to train under Dr. Roth during one of the final rotations he supervised at the Roth | McFarlane Hand and Upper Limb Center. His teaching was crafted through experience from a distinguished career in hand surgery and carried an immense amount of practical importance. I owe Dr. Roth a debt of personal gratitude for admitting me to the fellowship program and facilitating my combined Master's Degree. Without this training, I would not have had the privilege or opportunity to embark upon an academic career. Of all the lessons he taught, the most profound was that it is possible to have a great impact on both the field of surgery and a loving family.

Table of Contents

List of Figures

List of Appendices

Chapter 1

1 General Introduction

This thesis focuses on the use of Inter-cartilage Distance to measure arthrokinematics of the distal radioulnar joint (DRUJ). Contact relationships between the radius and ulna at the DRUJ are evaluated in both normal conditions, and in the setting of distal radius malunion. This chapter reviews the anatomy and biomechanics of the DRUJ. Methods for assessing articular contact and the effect of malunited distal radius fractures on the DRUJ are discussed, followed by a summary of the study rationale, objectives and hypotheses.

1.1 Bony and Soft Tissue Anatomy of the DRUJ

Two bones, the radius and ulna, constitute the bony architecture of the forearm. They articulate at the proximal (PRUJ) and distal (DRUJ) radioulnar joints (Figure 1.1), and permit forearm rotation (Appendix 2 provides a list of anatomical terms and definitions for reference).
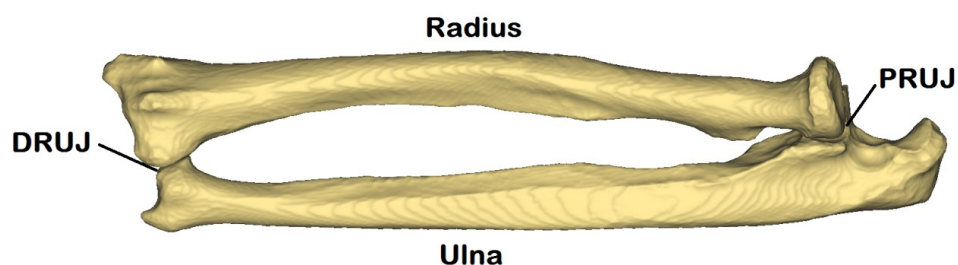
Figure 1.1: Bony anatomy of the forearm, depicting the radius, ulna and their corresponding articulations at the proximal (PRUJ) and distal (DRUJ) radioulnar joints (© B Gammon)

The radius and ulna are linked distally by a group of soft tissue structures known as the TFCC. TFCC stands for "Triangular Fibrocartilage Complex", a term originally

coined by Palmer and Werner[1]. The anatomic components include the dorsal and volar radioulnar ligaments with their superficial and deep fibers, the articular disc, meniscus homologue and extensor carpi ulnaris (ECU) subsheath (Figure 1.2). The articular disc is also referred to as the triangular fibrocartilage.
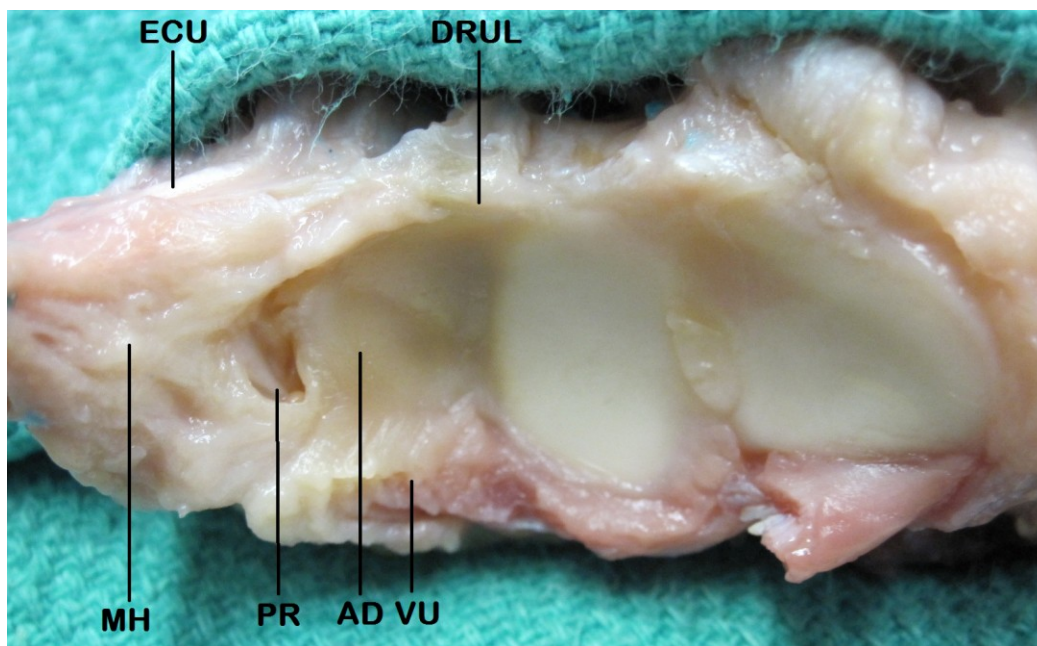
Figure 1.2: **The Triangular Fibrocartilage Complex. AD = Articular Disc, PR = Prestyloid Recess, VU = Volar Ulnocarpal Ligaments (includes ulnolunate, ulnocapitate and ulnotriquetral ligaments) arising off the Volar Radioulnar Ligament (deep and not shown), DRUL = Dorsal Radioulnar Ligament, MH = Meniscus Homologue, ECU = Extensor Carpi Ulnaris (© B Gammon)**

Other important soft tissue structures which impart a stabilizing effect on the DRUJ include the (1) DRUJ capsule (2) ulnolunate, ulnocapitate and ulnotriquetral ligaments, which arise off the volar distal radioulnar ligament (Figure 1.2) (3) Pronator Quadratus (PQ, Figure 1.3), a muscle which bridges the distal 1/3 of the radius and ulna, and has both superficial and deep heads (4) Extensor Carpi Ulnaris (ECU, Figure 1.4), one of the wrist extensor muscles, and (5) the forearm interosseous membrane (IOM, Figure 1.6), which has distal, accessory and central components. The function of these is discussed in Section 1.2.
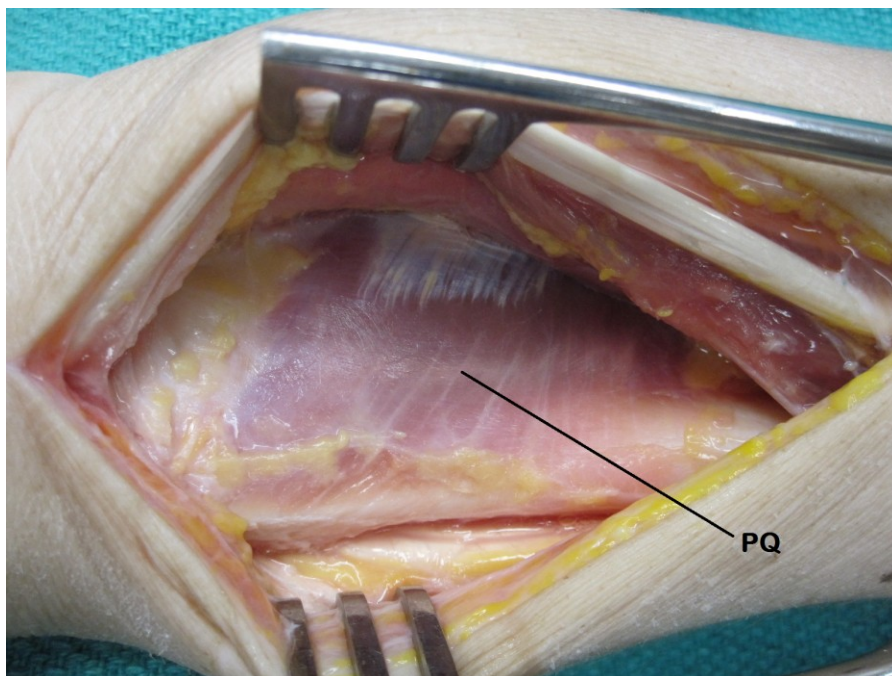
Figure 1.3: The volar surface of the forearm, flexor tendons retracted, depicting pronator quadratus (PQ) (© B Gammon)
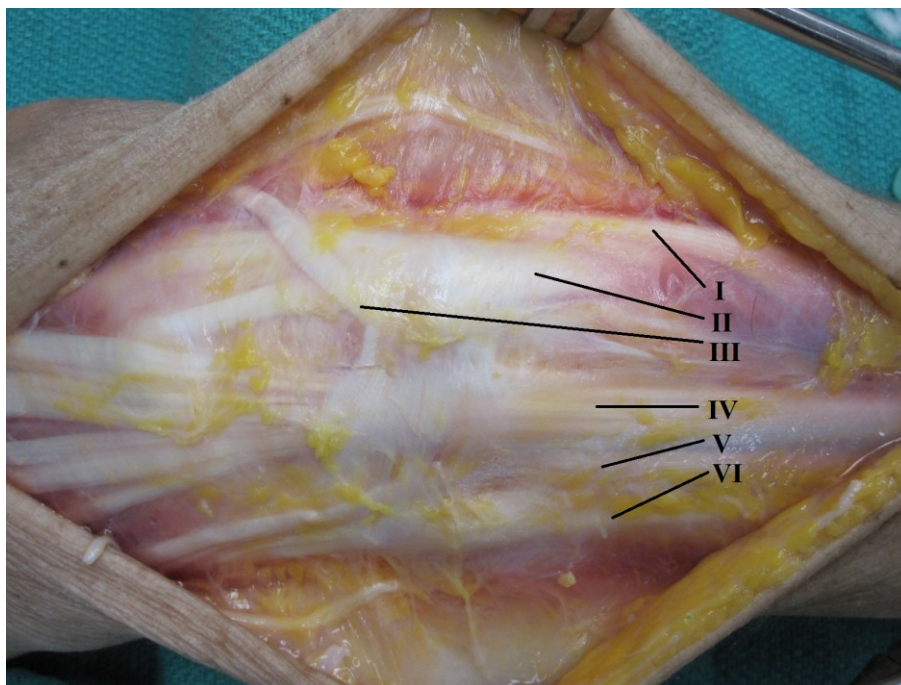
Figure 1.4: The dorsum of the wrist and overlying extensor tendons, including compartment VI, Extensor Carpi Ulnaris (ECU). Also depicted are the other wrist extensor compartments including I (Abductor Pollicis Longus and Extensor Pollicis Brevis), II (Extensor Carpi Radialis Longus and Brevis), III (Extensor Pollicis Longus), IV (Extensor Indicis and Digitorum Communis) and V (Extensor Digiti Minimi) (© B Gammon)
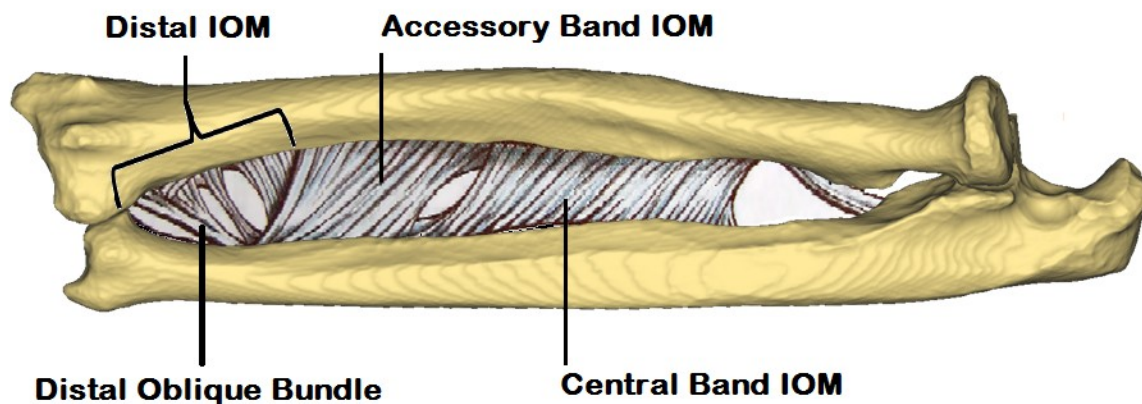
Figure 1.5: The anatomic components of the interosseous membrane (IOM), including the Distal IOM, Accessory Band and Central Band. The Distal Oblique Bundle is a sub-component of the Distal IOM and contributes to DRUJ stability when present (© B Gammon).

The DRUJ is comprised of the ulnar head and sigmoid notch. The ulnar head has an ovoid shape, which exerts a cam effect that is maximal in the neutral position. There is an area devoid of cartilage on the volar ulnar surface of the ulnar head termed the ulnar volar facet. Here the volar DRUJ capsule inserts, and this facet engages with the volar rim of the sigmoid notch in pronation (Figure 1.6)[2].
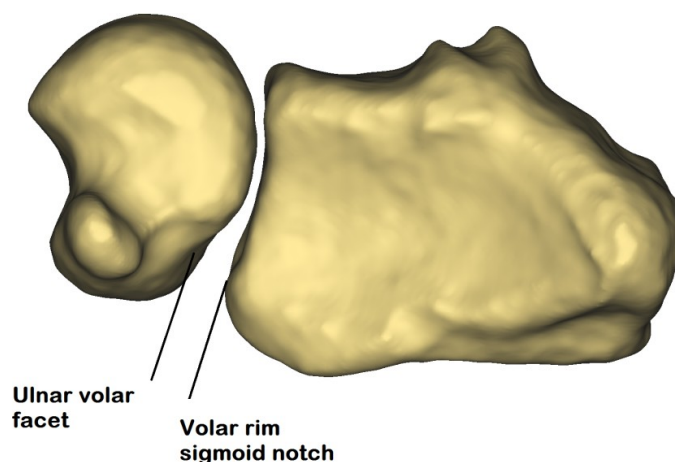
Figure 1.6: An axial representation of the DRUJ. The ulnar volar facet engages with the volar rim of the sigmoid notch at the DRUJ with the forearm in pronation (© B Gammon).

Other bony landmarks on the distal ulna include the articular dome, non-articular ulnar fovea, ulnar styloid and dorsal groove for ECU (Figure 1.7).

The distal ulnar dome sits beneath the articular disc of the TFCC complex while the fovea and styloid serve as attachment points for the superficial and deep fibers of the dorsal and volar radioulnar ligaments. The ECU tendon traverses the wrist and through part of its excursion runs in the dorsal ECU groove.

The concave sigmoid notch of the radius forms the opposing articular surface to complete this trochoid joint. The articular disc of the TFCC attaches at the distal aspect of the sigmoid notch.
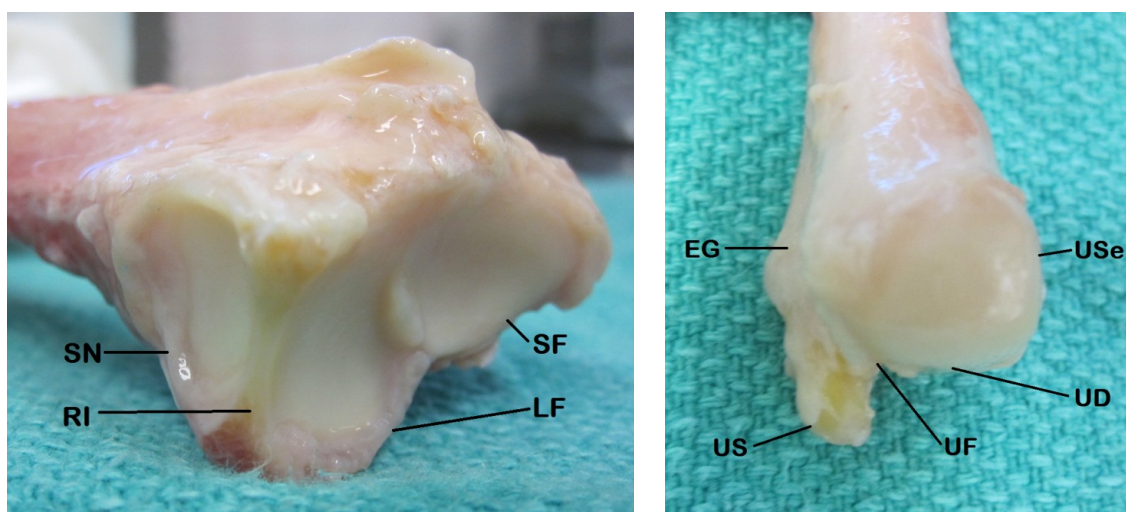
Figure 1.7: Osseous and articular anatomy of the distal radius and ulna: SN= sigmoid notch, RI = radial insertion TFCC, LF = lunate facet, SF = scaphoid facet, EG = ECU groove, US = ulnar styloid, UF = ulnar fovea, UD = ulnar dome, USe = ulnar seat (© B Gammon)

The radius of curvature of the sigmoid notch is approximately 15 mm with 47-80° of cartilaginous coverage. The ulnar head has a radius of approximately 10 mm. The convex articulating cartilage surface covers an arc of between 90-135° (Figure 1.8)[3].
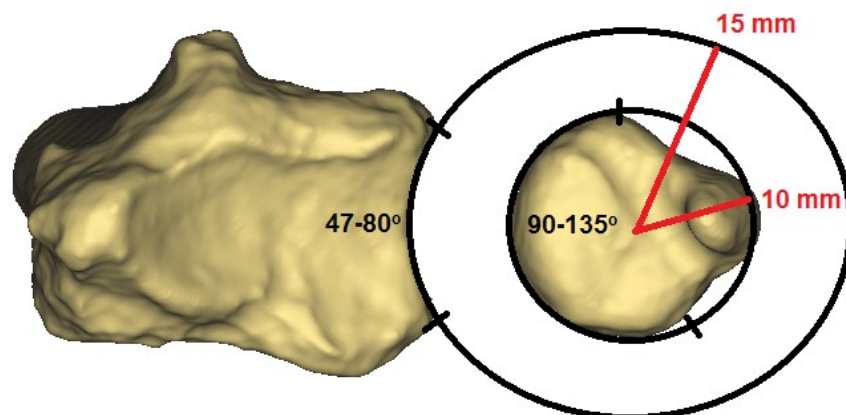
Figure 1.8: Radius of curvature and cartilaginous coverage of the ulnar head and sigmoid notch. The sigmoid notch has a larger radius of curvature relative to the ulnar seat. This lack of congruency causes a combined rolling and sliding interaction between the two surfaces during forearm rotation (© B Gammon).

The thickness of cartilage on the articulating portion of the ulnar head is relatively homogenous across its surface, while on the sigmoid notch the cartilage is thicker centrally[2]. On average only the distal aspect, comprising 69% of the sigmoid notch surface area is covered in cartilage with a normal proximal bare area[4]. The cartilage thins progressively moving from distal to proximal in the notch (Figure 1.9)[2].
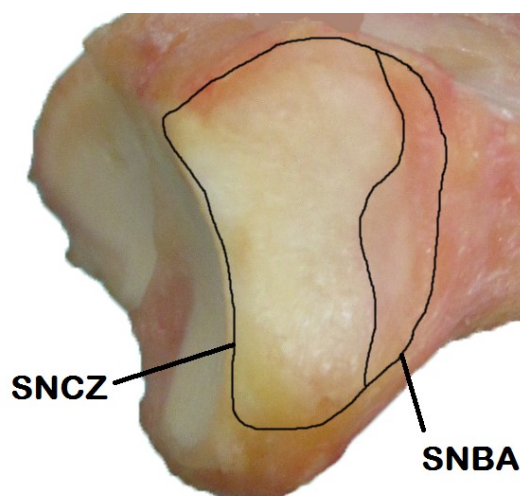
Figure 1.9: Cartilage distribution within the sigmoid notch: SNBA = sigmoid notch bare area, SNCZ = sigmoid notch cartilaginous zone. Note that approximately 69% of the sigmoid notch is covered in cartilage, while the proximal 31% is bare (© B Gammon)

Seminal work by Tolat et al.[5] defined the morphology of the sigmoid notch and its relationship to DRUJ stability. Four subtypes of morphology in the sagittal plane were described. They include, in order of descending prevalence: Flat Face, C-type, S-type and Ski Slope (Figure 1.10).

| Flat Face | C-Type | S-Type | Ski Slope |
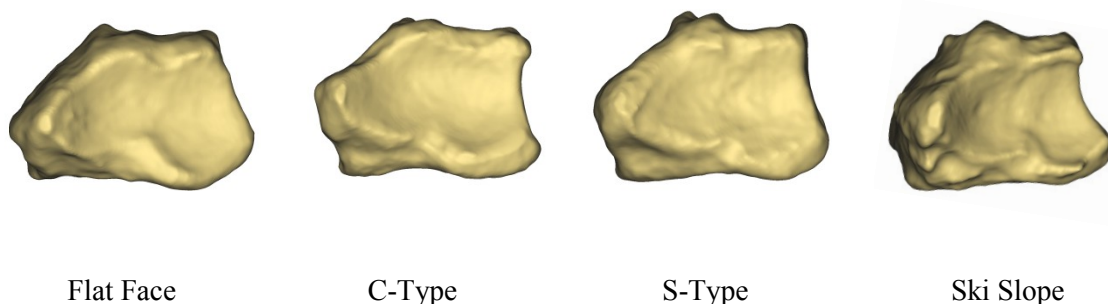
Figure 1.10: Sagittal plane morphology of the sigmoid notch: Flat Face, C-Type, S-Type and Ski Slope (© B Gammon).

In the coronal plane, the DRUJ can also vary. The articular surface slope of the sigmoid notch and ulnar head can be parallel, oblique or reverse oblique[5]. The mean inclination of the sigmoid notch has been reported to be 8° (range -24 to 27°) (Figure 1.11)[6].
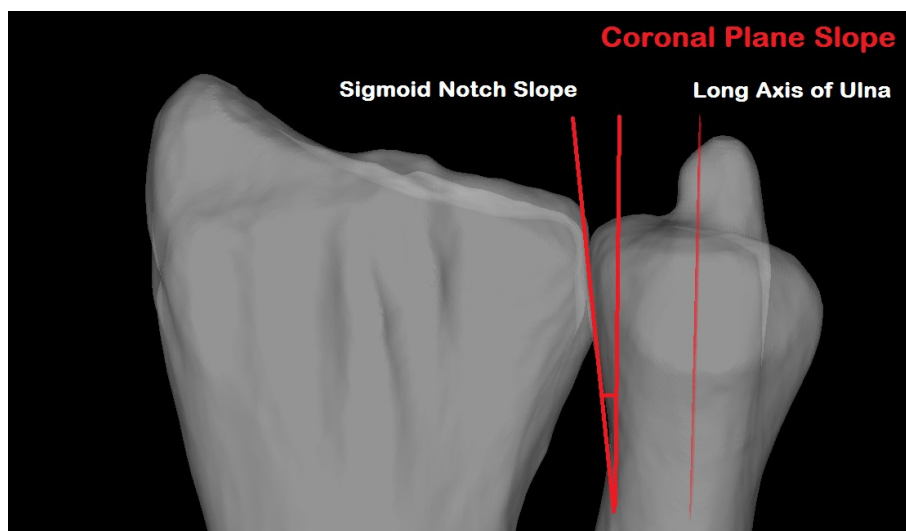
Figure 1.11: **Coronal plane morphology of the DRUJ depicting a reverse oblique sigmoid notch, whose angle is measured off a line parallel to the long axis of the ulna (© B Gammon).**

The distal ulnar diaphysis is relatively straight, with the ulnar head being laterally offset from the long axis of the shaft by approximately 20° (range -14 to 41°)[3,6]. Proximally, there is a varus bow which averages 17.7° (range 11-28°)[7], as well as an anterior bow termed the proximal ulna dorsal angulation or PUDA, which averages 5.7° (range 0-14°)[8] (Figure 1.12).
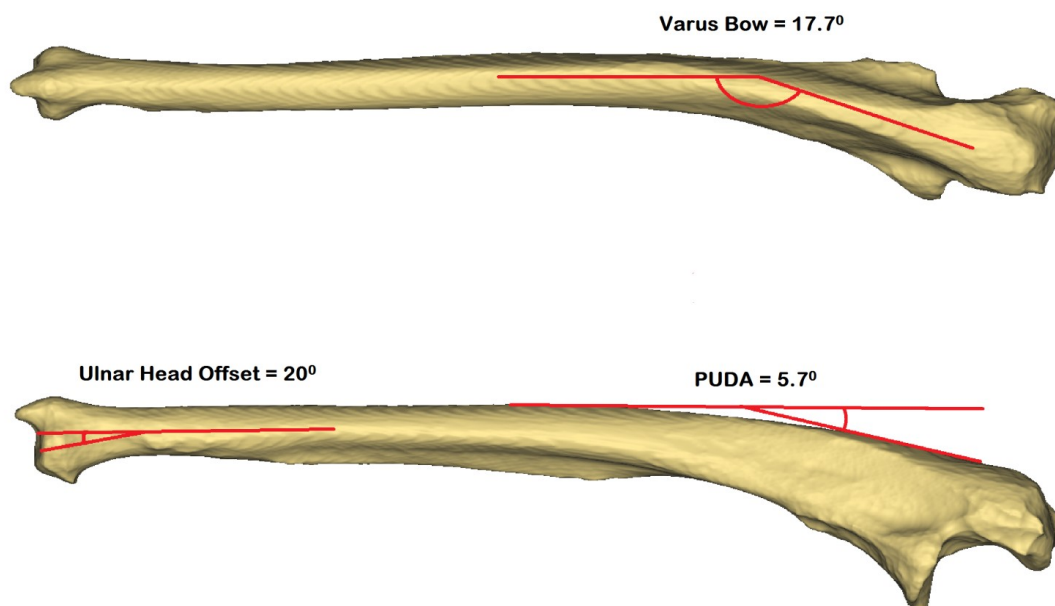
Figure 1.12: Bony anatomy of the ulna depicting the ulnar head offset, varus bow and proximal ulna dorsal angulation (PUDA) (© B Gammon).

The diaphysis of the radius is bowed in the sagittal and coronal planes, which prevents the forearm bones from impinging in pronation. In the coronal plane the bow is located in the middle third of the radius averaging 10.3° apex lateral. In the sagittal plane there is an apex dorsal bow between the tuberosity and midshaft of the radius averaging 4.7° (Figure 1.13)[9].

Apex lateral coronal bow = 10.3⁰

Apex dorsal saggital bow = 4.7⁰
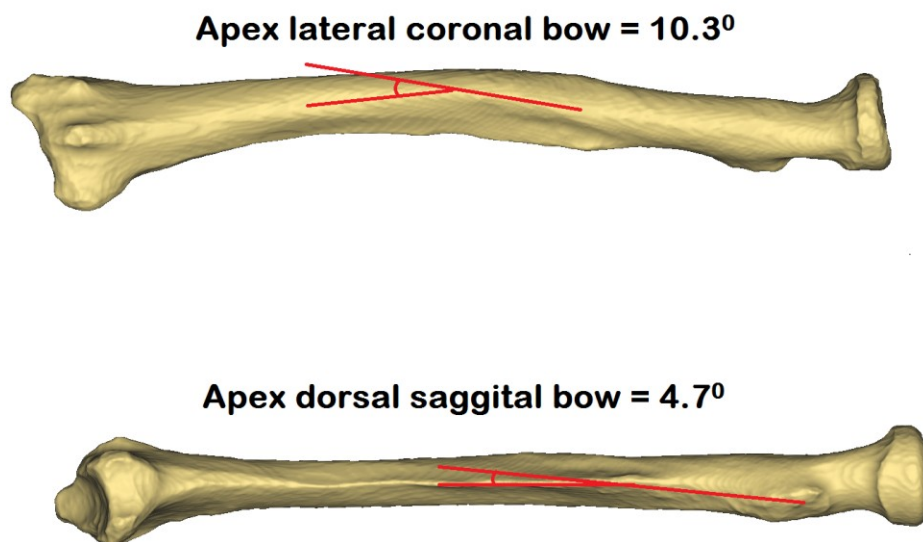
Figure 1.13: Bony anatomy of the radius depicting the apex lateral bow in the coronal plane and apex dorsal bow in the saggital plane (© B Gammon).

1.2   Stabilizers of the DRUJ

Bony anatomy plays a significant role in the stability of the DRUJ. The dorsal and volar osseous rims prevent excessive dorsal and volar translation of the ulnar head within the sigmoid notch. The palmar rim is more prominent and deficiency in this region can precipitate instability[10]. The DRUJ is inherently stable in supination, even when its associated soft tissue stabilizers have been denuded[11].

As was demonstrated in Figure 1.8 however, the DRUJ joint surfaces are relatively incongruous. Because of this articular incongruency, soft tissues also play a major role in the stabilization of this joint. DRUJ stability comes in part from the dorsal and volar radioulnar ligaments[12]. These components of the TFCC (Figure 1.2) are considered some of the most important stabilizers of the DRUJ. They have both superficial fibers which insert onto the ulnar styloid, and deep fibers which attach to the fovea of the ulnar head (Figure 1.14)
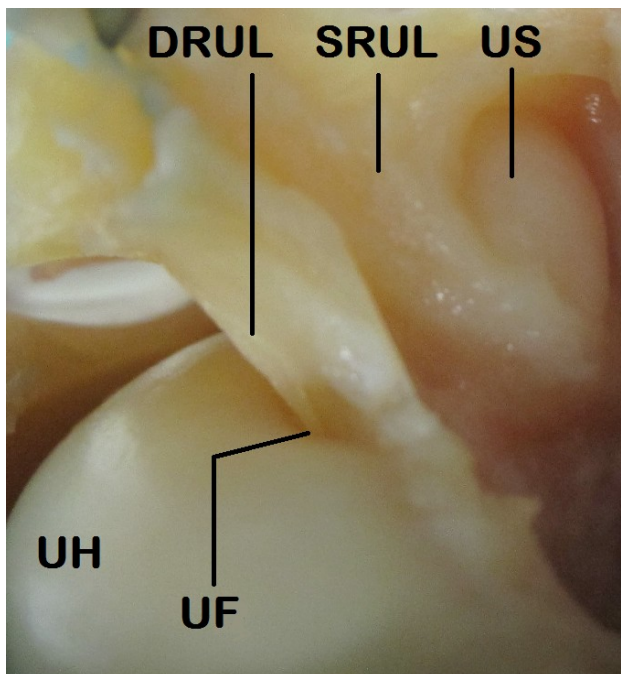
Figure 1.14: A magnified view of the superficial fibers (SRUL) and deep fibers (DRUL) of the radioulnar ligaments, which attach onto the ulnar fovea (UF) and ulnar styloid (US). The ulnar head (UH) lies beneath © B Gammon.

The dorsal ligament tensions in pronation, buttressing the ulnar head in conjunction with the dorsal rim of the sigmoid notch to prevent dorsal translation[13,14,15,16]. In pronation, the volar radioulnar ligament also acts as a checkrein to keep the ulnar head located[3,17]. Conversely, in supination the volar ligament tensions to hold the ulnar head in the sigmoid notch, acting as a buttress in concert with the volar rim of the sigmoid notch[13,14,15,16]. The dorsal radioulnar ligament acts as a checkrein to excessive volar translation of the ulnar head in supination[3,17]. The foveal attachments have been found to be the most important components conferring stability[18]. Even when all other stabilizers are sectioned, the combination of the articular disc and distal radioulnar ligaments are capable of maintaining normal DRUJ kinematics through forearm rotation[12]. Significant dorsalpalmar instability occurs when the distal radioulnar ligaments are disrupted. However, provided they are at least partially intact, further stability can be obtained with ulnar shortening osteotomy and re-tensioning of the residual tissue[19].

The ulnolunate and ulnotriquetral ligaments originate off the volar radioulnar ligament (Figure 1.2) and are in maximal tension with the forearm in supination. The ulnocarpal collateral ligament is a structure originally described by Palmer and Werner[1]. Its existence is controversial, and this tissue may consist of thickened ulnar capsule and ECU subsheath[20]. When tested as a ligament, it seems to stabilize the ulnocarpal joint in both pronation and supination[14].

The articular disc (or triangular fibrocartilage) originates on the ulnar aspect of the lunate fossa and inserts into the dorsal and volar radioulnar ligaments peripherally (Figure 1.2). The disc glides over top of the ulnar dome, functioning to extend the lunate facet's articular surface and act as part of a mobile platform for the ulnar carpus[2,21].

The meniscus homologue is a synovium-like soft tissue structure which occupies the space between the articular disc, ulnocarpal capsule and triquetrum (Figure 1.2)[22]. It helps to exert a sling effect, stabilizing the ulnar carpus. Between the meniscus homologue and articular disc lies the prestyloid recess[21]. Variability has been found with the morphology of this orifice, which was found to be narrow in 74% of specimens, wide in 11% and absent in 15%[22].

The DRUJ capsule plays an important role in stability. In fact, significant restoration of DRUJ kinematics can be achieved by capsular repair alone[23]. In histological studies the fiber orientation of the inferior capsule has suggested it has the ability to prevent axial translation. Dorsal and palmar translation is also constrained by the DRUJ capsule. The volar capsule is likely more important in this regard, with redundant oblique folds of tissue that act as a sling for the ulnar head in supination. The dorsal capsule is thinner and accommodates the ulnar head in pronation[24]. Sectioning studies have noted that the radius displaces volarly relative to the ulna in pronation when the dorsal capsule is sectioned. Similarly, the radius subluxes dorsally in supination relative to the ulna when the volar capsule is sectioned[25].

The PQ (Figure 1.3) functions as a dynamic stabilizer of the DRUJ when contracted in full pronation[26]. Dynamic stability of the DRUJ is also conferred by activation of the deep head during forearm rotation[27,28]. The PQ serves to co-apt the intact

DRUJ. In the setting where the ulnar head is excised however, authors have noted that the PQ exacerbates DRUJ instability in pronation. In this scenario, contraction of the PQ during causes radioulnar convergence and subluxation of the radius dorsally relative to the distal ulna[27]. Other authors have also noted this phenomenon, and found that ablation of the ulnar head and styloid results in significant dorsopalmar instability in addition to radioulnar convergence[29,30,31].

The ECU (Figure 1.4) and its subsheath act as a dynamic stabilizer of the DRUJ[32]. During pronation, ECU contraction causes the distal ulna to be depressed volarly relative to the ulnar carpus. The ECU actively stabilizes the DRUJ and ulnocarpal joints in neutral and supination, particularly in the setting of a sectioned TFCC.   The ECU subsheath also acts as an adjunctive static stabilizer for the DRUJ, especially in the neutral forearm position[33]

Finally, a note should be made of the IOM (Figure 1.5). It has been long established that the IOM prevents longitudinal motion between the radius and ulna. The central band is the strongest component; however in recent years more focus has been placed on the distal IOM for its contribution to secondary DRUJ stability. The distal IOM is taut in all forearm positions and has been found to prevent excessive dorsal/volar translation. It prevents volar ulnar displacement in pronation and dorsal ulnar displacement in supination[34]. The distal IOM acts to stabilize the DRUJ once the distal radioulnar ligaments have been injured[15]. Recent studies have evaluated this region of the IOM for a thickened band of tissue, now termed the Distal Oblique Bundle[35]. Biomechanical evidence suggests that specimens with a Distal Oblique Bundle have increased stability of their DRUJ[36].

1.3   DRUJ and Forearm Biomechanics

The longitudinal axis of forearm rotation passes through the center of the radial head proximally and the ulnar head distally (Figure 1.15).
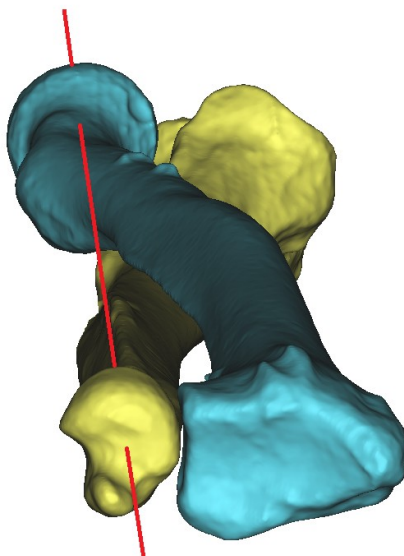
Figure 1.15: Centre of rotation of the forearm, passing through the centre of the radial head and ulnar fovea (© B Gammon).

During forearm motion, the radius rotates around the ulna distally through an arc of pronation (palm down) and supination (palm up). In most normal individuals the total arc of motion measures between 150-180°. Translational motion between the ulnar head and sigmoid notch also occurs in addition to rotation. This is due to their different radii of curvature, with the sigmoid notch having a 50-100% greater arc compared with the ulnar head[5]. The ulnar head translates dorsally relative to the distal radius in pronation, and volarly in supination[11]. Because of this obligate translation at the DRUJ, the rotational axis of the forearm changes through pro-supination. In pronation, the axis of rotation is at the radial side of the DRUJ and it moves ulnar in supination[37]. The radius also translates proximally and distally relative to the ulna during forearm rotation[37]. In pronation, ulnar length increases relative to the radius while in supination it decreases[38,39]. With load, the relative changes in ulnar length increase during forearm rotation[37]. The radiographic position of the radius and ulna in the coronal plane is termed ulnar variance (Figure 1.16), and averages -0.9 mm (range -4.2 to 2.3 mm between individuals). The net radiographic result at the wrist is that the ulnar head moves distal relative to the sigmoid notch as the forearm moves from supination to pronation[40].

Load is distributed across both the radiocarpal and ulnocarpal joints, as well as through the DRUJ. Through an arc of simulated pronation and supination the joint reaction force at the DRUJ has been found to vary between 2-10 N[41]. In supination, the ulna comes into direct alignment with the carpus and accepts more axial load than in pronation. Generally, the distal ulna is felt to bear ~18% of the axial load, with the balance supported by the distal radius[38], though some authors have reported that it supports up to 1/3 of the force placed across the wrist[42]. Varying muscle loads usually do not affect the joint reaction force at the DRUJ in the setting of an intact TFCC[41]. However, because of its load sharing properties, disruption of the distal radioulnar ligaments increases the force that must be borne across the DRUJ articulation[43].

The length of the radius relative to the ulna has also been found to play a role in force distribution across the ulnocarpal region and DRUJ. At the ulnocarpal joint, pressure increases proportionally with radial shortening and decreases with radial lengthening[44]. Shortening the ulna by 2.5 mm decreases ulnocarpal load to 4%, while increasing ulnar length by 2.5 mm increases load to 42%[38]. At the distal radioulnar joint, radial shortening (and resultant relative ulnar lengthening) had no effect on DRUJ pressure[44]. However, progressive shortening of the ulna relative to the radius has been found to increase pressures in the DRUJ[44,45]. Partial and complete sectioning of the TFCC reduced peak pressure in the DRUJ, but the effect of increased pressure with further ulnar shortening remained present[45]. This relates to the tension of the distal radioulnar ligaments, DRUJ capsule, IOM and ulnocarpal ligaments, which are stretched with relative ulnar shortening and cause an increased DRUJ compressive force.

1.4   Distal Radius Malunion and its Influence on the DRUJ

The normal geometry of the distal radius and its relationship to the distal ulna has been previously reported[46,47,48]. It is described in terms of radial inclination, radial length, ulnar variance and volar tilt based on plain radiographs. The distal radial articular surface has an average inclination of 24°, a radial length of 9-12 mm distal to the ulna, an ulnar variance of -0.9 mm and a volar tilt of 11° [46,47,48].
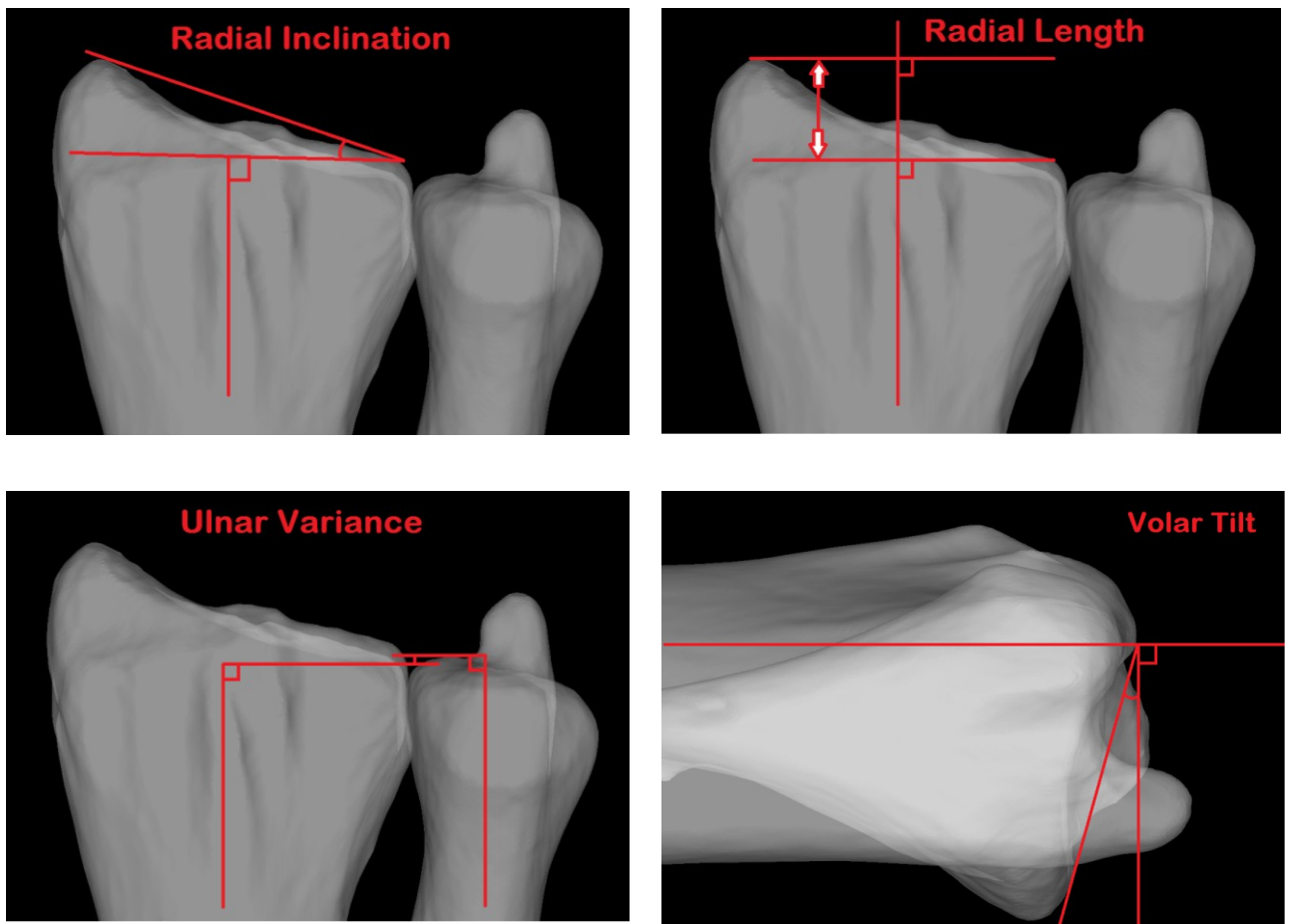
Figure 1.16: Measurement parameters for the distal radial articular surface, including radial inclination, length, ulnar variance and volar tilt (© B Gammon).

Distal radius fractures are an extremely common injury. Certain factors can predispose these to malunion, such as osteoporotic bone, significant initial fracture displacement, patient age >60, and comminution[49]. Changes in the normal orientation of the distal radius alters the kinematics of the distal radioulnar joint[50,51,52,53,54]. This relates to the abnormal soft tissue tensions created as well as incongruency of the sigmoid notch relative to the ulnar head. Increasing the degree of malunion has a progressively detrimental effect. Clinically, distal radius malunion has been associated with DRUJ dysfunction causing ulnar-sided wrist pain, restricted forearm rotation and in cases of a ruptured TFCC complex, instability[55,56].

1.5   Joint Contact at the DRUJ in Normal and Malunited Conditions

An understanding of the biomechanics of an articulation, including its contact mechanics, is an important element in the assessment of joint function. However, arthrokinematics, or the specific movement of joint surfaces[57], have not been well defined in the literature for the DRUJ.

Under normal conditions, articular contact is maximal in the neutral position, comprising up to 60% of the DRUJ surface area[58]. There is minimal contact (less than 10% of the total DRUJ surface area) between the sigmoid notch and ulna at the extremes of pronation and supination[3]. Ishii et al.[22] evaluated pressure and contact area in the DRUJ with loaded cadaveric forearm specimens using dynamic pressure sensitive film. They reported that 12.5% of the sigmoid notch or 15.7 mm^2 was in contact with the DRUJ in the neutral position. They also described a centroid which was located at the dorsum of the sigmoid notch in pronation, and the volar aspect of the sigmoid notch in supination. Shaaban et al.[59] also looked at contact area within the DRUJ using dynamic pressure sensitive film. They reported the least contact in extreme pronation, and a successive increase in contact up to 30° of supination, where contact was maximal, reducing thereafter. In the loaded scenario this was 67.5 mm^2, and there was no significant effect from DRUL sectioning and repair. Similar to the findings of Ishii et al., these authors noted that the centroid of contact in the sigmoid notch moved dorsally with pronation and volarly with supination.

Crisco et al. examined the *in vivo* effects of distal radius malunion on articular contact in the DRUJ. Their subjects were live patients with chronically malunited distal radii, whose deformities included shortening, dorsal angulation and loss of radial inclination. The authors evaluated joint congruity using an interbone distance algorithm to give measurements of interbone spacing area (a proxy for contact area) and interbone spacing centroid location (analogous to a contact centroid). A threshold distance of 5 mm was used. These authors reported a contact area of 215 mm^2 in normal individuals, and 155 mm^2 in the setting of malunion. The centroid of contact did not appear change with

forearm rotation or along the volar-dorsal axis, though contact was on average 1.3 mm more proximal in the malunited condition[60].

1.6   Methods for Assessing Joint Contact

1.6.1   Direct Methods

Techniques to evaluate and quantify the contact area between opposing articular surfaces have evolved considerably over the past 30 years. Initial attempts were invasive and involved so-called "Direct" methods. One such technique is casting, which was described by Stormont et al.[61] as the most reproducible option. Casting entails the injection of low viscosity cement into a joint, which is allowed to solidify and is subsequently extracted. The area devoid of cement is considered to represent the joint contact area (Figure 1.17).
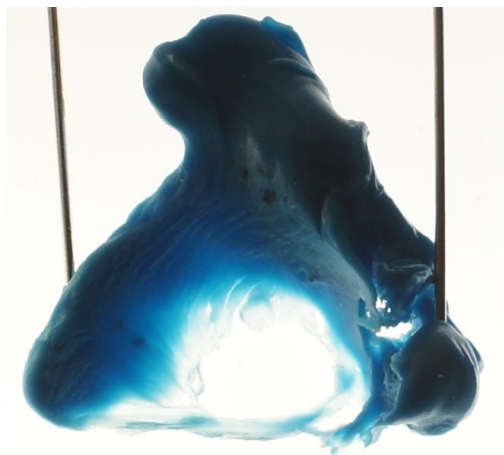
Figure 1.17: A DRUJ casting illuminated on a lightbox. Note the central area devoid of casting material, which is designated as the contact patch (© B Gammon).

There are disadvantages to casting; it is time consuming and only static joint positions can be examined. It cannot be used for dynamic *in vitro* experiments over a broad range of motion. Moreover, the introduction of casting material into a joint is destructive, and requires partial or complete sectioning of the surrounding capsule and soft tissue which may alter the joint kinematics and contact patterns. It has been used by

many authors to both quantify joint contact[61,62,63,64,65] and also to validate new techniques[66,67]. To our knowledge, it has not been used previously in the wrist.

Pressure sensitive film, such as Fujifilm Prescale (© Sensor Products Inc., Madison NJ), is another direct method of assessing joint contact area and pressure. The film is inserted into the joint, which is subsequently loaded in a single position. The distribution and magnitude of pressure created between two contacting surfaces can be ascertained from the colors displayed on the film. The film is calibrated such that a deeper pigment color reflects a higher contact pressure. Contact area can also be quantified from the film. Disadvantages include the capsular and ligamentous sectioning that must occur to place the film in the joint, as well being labor-intensive. Only static recordings are possible, and the film is prone to artifact such as shear stress, staining and crinkling, particularly with curved joint surfaces. The interposition of this material (with a thickness of 0.11 mm) may also alter joint contact pressure and area. Pressure sensitive film has previously been used in the wrist to quantify radiocarpal contact[68,69].

A dynamic pressure-sensitive film sensor represents the evolution of pressure-sensitive film. The most commonly reported version is Tekscan (© Tekscan Inc., South Boston MA) which is a thin pressure monitoring system comprised of numerous individual sensing elements. Tekscan can be used to characterize and quantify both contact area and contact pressure, and has the advantage of providing real-time data through a range of joint motion. Disadvantages include its invasive introduction and artifact from wrinkling. Moreover, Tekscan has a thickness of 0.1 mm and like pressure sensitive film exerts a mass effect that may alter the bearing surface contact when inside the joint. It has been used in both the radiocarpal joint[70] and DRUJ[22,44,45, 59,71].

1.6.2   Indirect Methods

Alternative methods of studying joint contact use indirect techniques. In this scenario, volumetric data from CT or MRI datasets can be used to generate 3-D bone and cartilage models. Contact measurements can be garnered from CT and MRI datasets directly, but the process is tedious. Authors have previously examined individual slices and extrapolated contact based on the number of overlapping pixels[72]. This method is

felt to be inaccurate particularly for complex joints with undulating surfaces. Consequently, researchers have developed methods to measure joint contact using proximity maps. These are created using the same 3-D models derived from CT[73] or MRI volumetric data sets[66,74,75,76]. Distance thresholds are set and contact area is subsequently calculated using software algorithms. This method can also be used to establish the centroid of contact and has been validated against invasive techniques for use in the wrist[77].

To further understand changes in joint function and contact, these indirect techniques can be applied in conjunction with simulated joint motion. Kinematic information can be collected directly from experimental cadaveric models (*in vitro* kinematics). Common techniques used to quantify joint kinematic data *in vitro* include biplanar fluoroscopy[78], electromagnetic tracking[79], stereophotogrammetry[80] and, most recently, optical tracking[54]. 3-D models of the joint of interest are created using CT or MRI volumetric datasets. These models are then registered, or matched, to the experimental specimen's anatomy using mathematical algorithms[81,82,83,84]. Proximity maps are made from the registered 3-D models and optical tracking kinematic data[67,85]. Thresholds for the overlap of models are used to characterize the location and area of joint contact[86,87]. This allows for joint contact area to be measured through an arc of motion using non-invasive, or indirect, methods. The dynamic evaluation of joint surfaces and the characterization of their interaction is termed Arthrokinematics[88].

Unlike *in vitro* methods where kinematics are measured directly, *in vivo* methods compare relative joint positions on CT or MRI using computational means. The changes in the position and orientation of the models are then quantified. *In vivo* techniques have also been used to characterize kinematic changes in the carpal bones under various experimental conditions[89,90,91,92,93,94].

Presented in this thesis is a novel technique which utilizes a form of proximity mapping termed Inter-cartilage Distance or ICD[86]. With ICD technique, bone and cartilage anatomy is isolated by denuding soft tissues from the arm after testing. Fiducial markers are fixated on the specimens prior to scanning, and their positions are digitized

relative to the optical trackers. The articulation is then CT scanned with air contrast, and 3-D models which include articular cartilage are subsequently generated from the volumetric scan data. Fiducial based registration[95] is then used to link the 3-D bone and cartilage models, and restore their relative position and orientation from the testing procedure. The Inter-cartilage distance algorithm is used to create proximity maps of the DRUJ, and areas with cartilage overlap between models are designated as areas of contact[86].
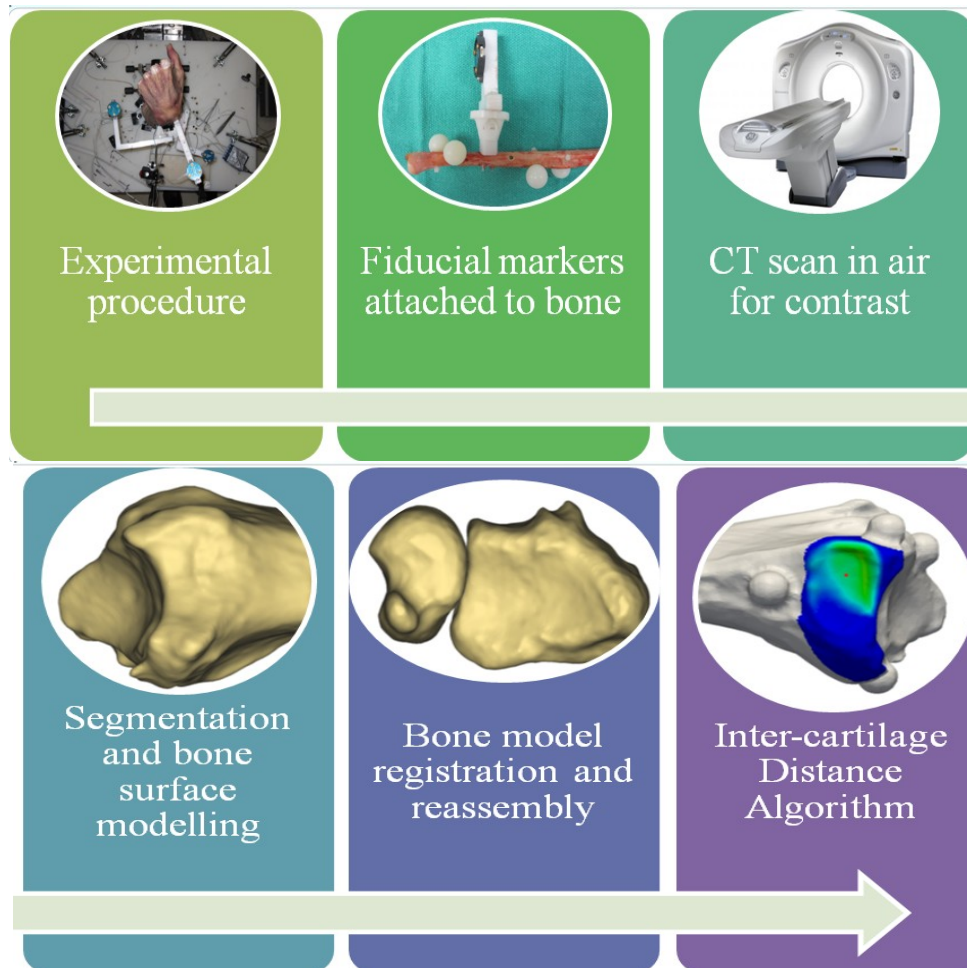
Figure 1.18: A flowchart demonstrating the methods by which contact patterns for the DRUJ can be obtained using an *in vitro* model, with fiducial based registration and an Inter-cartilage Distance algorithm for proximity mapping (© B Gammon).

This method is an important advance because unlike the previously described Inter-bone Distance (IBD) technique[96], it accounts for regional variations in cartilage thickness and location (Figure 1.19).
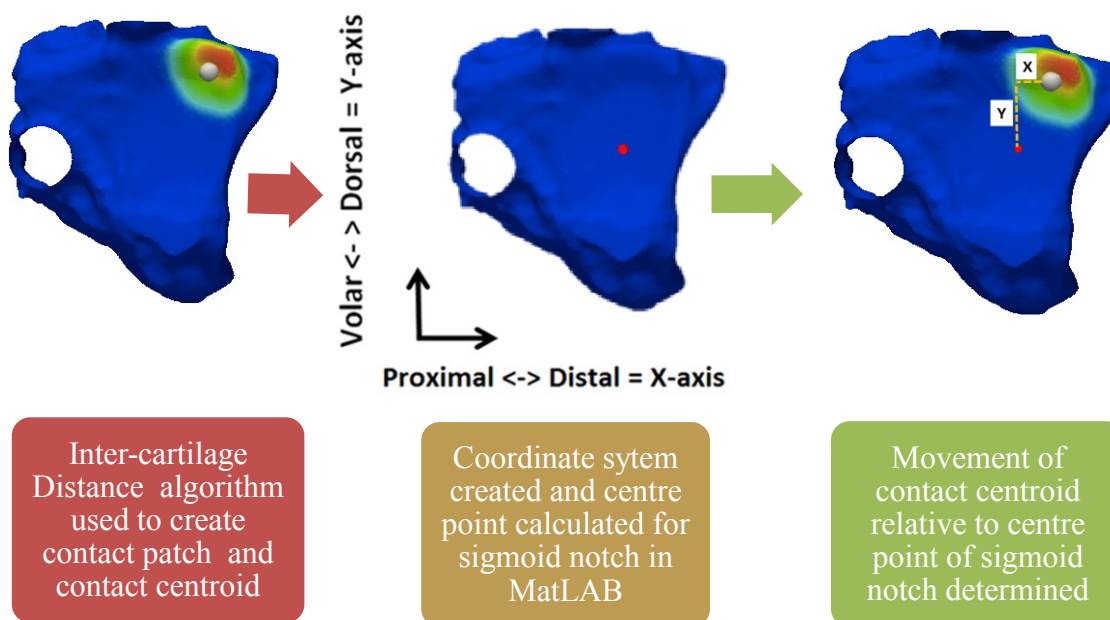
Figure 1.19: **A flowchart demonstrating the methods by which contact centoid position for the DRUJ can be described relative to a centre point, with a coordinate system for the sigmoid notch generated using MatLAB (MATLAB 8.0, The MathWorks, Inc., Natick, Massachusetts, United States) (© B Gammon).**

1.7   Rationale

Disorders of the distal radioulnar joint are a common clinical entity, and can be associated with significant disability[97]. Post-traumatic instability of the DRUJ is one such disorder, and is associated with TFCC insufficiency[98,99]. Patients often complain of ulnar-sided wrist pain, a weak grip and occasionally mechanical symptoms such as a sensation of subluxation[97]. Incongruency of the DRUJ following distal radius malunion is another common clinical presentation[100,101]. Patients again present with ulnar-sided wrist pain, decreased grip strength, restricted forearm rotation and visible deformity[97,102]. It is theorized that these disorders can progress to osteoarthritis of the DRUJ in the chronic setting, and that surgery may have a role in halting this process[97].

A variety of interventions have been described to alleviate symptoms from DRUJ instability and malalignment. Open and arthroscopic TFCC repair[103,104], DRUJ capsular plication[105], ulnar shortening osteotomy[19] and DRUJ ligament reconstruction[106,107] have all been described to address TFCC insufficiency with concomitant DRUJ instability. Distal radius osteotomy can be effective for the treatment of symptoms from DRUJ incongruency due to distal radial malunion[56]. The kinematic effect of these procedures has been previously reported[23,44,51,52,53,54,108,109,110].

Arthrokinematics examines the specific movement of joint surfaces, and new techniques have recently been developed, which accurately describe contact patterns in diarthrodial joints[57]. Using these arthrokinematic techniques to evaluate joint contact will improve our understanding of both normal joint function and effect of disorders such as ligamentous insufficiency or osseous deformity. Arthrokinematics can also be used to evaluate the effectiveness of rehabilitation protocols and surgical interventions in restoring normal joint contact patterns. The arthrokinematics of both the normal and pathologic DRUJ are poorly understood; therefore the purpose of this thesis will be to utilize the novel technique of Inter-cartilage Distance to describe and quantify these contact patterns.

1.8   Objectives and Hypotheses

Objectives:

1) To utilize the Inter-cartilage Distance algorithm to quantify joint contact at the DRUJ and compare this method to gold standard techniques such as casting and Tekscan®.
2) To employ the Inter-cartilage Distance algorithm to characterize the *in vitro* arthrokinematics of the DRUJ throughout an arc of simulated forearm supination.
3) To use Inter-cartilage Distance to describe and quantify the effect of simulated dorsally angulated distal radius malunion and TFCC rupture on *in vitro* DRUJ arthrokinematics.

Hypotheses:

1) Inter-cartilage Distance is effective at characterizing DRUJ contact patterns when compared with other standardized techniques.

2) We theorize that: a) DRUJ contact area and centroid location will change with forearm rotation and b) simulated active supination will increase contact area compared with passive supination.

3) We predict that: a) increasing dorsal angulation deformity of the distal radius will decrease the DRUJ contact area and displace the contact centroid volarly and distally at the sigmoid notch b) sectioning of the TFCC will reduce DRUJ contact area and make the pathway of the contact centroid more variable.

1.9   Thesis Overview

In Chapter 2, contact area in the DRUJ is evaluated using Tekscan, casting and Inter-cartilage Distance. A custom *in vitro* forearm positioning apparatus allows for the effect of tendon loading and forearm position to be examined. In Chapter 3, contact patterns are investigated in the native DRUJ during simulated active motion using an *in vitro* wrist simulator. Inter-cartilage Distance is used to characterize both the size of the contact patch and centroid position in the sigmoid notch across an arc of forearm rotation from 60° of pronation to 60° of supination. In Chapter 4, the effect of dorsal angulation deformities on contact patterns in DRUJ is evaluated. A custom adjustable implant is used to create 10, 20 and 30° of dorsal angulation from the intact condition. Inter-cartilage Distance yields a centroid location and contact area measurement for each interval of forearm rotation. Simulated active motion is generated using an *in vitro* wrist simulator. Chapter Five provides a summary of all three studies and indicates directions for future work.

1.10   References

1. Palmer AK, Werner FW. The triangular fibrocartilage complex of the wrist - anatomy and function. *J Hand Surg Am*. 1981;6(2):153-162.

2. Buck FM, Nico MA, Gheno R, Haghighi P, Trudell DJ, Resnick D. Morphology of the distal radioulnar joint: cadaveric study with MRI and MR arthrography with the forearm in neutral position, pronation, and supination. *AJR Am J Roentgenol*. 2010;194(2):202-207.

3. Ekenstam FA. Anatomy of the distal radioulnar joint. *Clin Orthop Relat Res*. 1992;(275):14-8.

4. Collins ED, Vossoughi F. A three-dimensional analysis of the sigmoid notch. *Orthop Rev*. 2011;3(2):e17.

5. Tolat AR, Stanley JK, Trail IA. A cadaveric study of the anatomy and stability of the distal radioulnar joint in the coronal and transverse planes. *J Hand Surg Br*. 1996;21(5):587-594.

6. Sagerman SD, Zogby RG, Palmer AK, Werner FW, Fortino MD. Relative articular inclination of the distal radioulnar joint: a radiographic study. *J Hand Surg Am*. 1995;20(4):597-601.

7. Windisch G, Clement H, Grechenig W, Tesch NP, Pichler W. The anatomy of the proximal ulna. *J Shoulder Elbow Surg*. 2007;16(5):661-6.

8. Rouleau DM, Faber KJ, Athwal GS. The proximal ulna dorsal angulation: a radiographic study. *J Shoulder Elbow Surg.* 2010;19(1):26-30.

9. Rupasinghe SL, Poon PC. Radius morphology and its effects on rotation with contoured and noncontoured plating of the proximal radius. *J Shoulder Elbow Surg*. 2012;21(5):568-73.

10. Wallwork NA, Bain GI. Sigmoid notch osteoplasty for chronic volar instability of the distal radioulnar joint: a case report. *J Hand Surg Am*. 2001;26(3):454-9.

11. King GJ, Ogston NG, McMurtry RY, Rubenstein JD. Computerized tomography of the distal radioulnar joint: correlation with ligamentous pathology in a cadaveric model. *J Hand Surg Am*. 1986;11(5):711-717.

12. Gofton WT, Gordon KD, Dunning CE, Johnson JA, King GJ. Soft-tissue stabilizers of the distal radioulnar joint: an in vitro kinematic study. *J Hand Surg Am*. 2004;29(3):423-431.

13. Acosta R, Hnat W, Scheker L. Distal radio-ulnar ligament motion during supination and pronation. *J Hand Surg Br*. 1993;18(4):502-505.

14. DiTano O, Trumble TE, Tencer AF. Biomechanical function of the distal radioulnar and ulnocarpal wrist ligaments. *J Hand Surg Am*. 2003;28(4):622-627.

15. Kihara H, Short WH, Werner FW, Fortino MD, Palmer AK. The stabilizing mechanism of the distal radioulnar joint during pronation and supination. *J Hand Surg Am*. 1995;20(6):930-6.

16. Schuind F, An KN, Berglund L, Rey R, Cooney WP 3rd, Linscheid RL, Chao EY. The distal radioulnar ligaments: a biomechanical study. *J Hand Surg Am*. 1991;16(6):1106-14.

17. Stuart PR, Berger RA, Linscheid RL, An K. The dorsopalmar stability of the distal radioulnar joint. *J Hand Surg Am*. 2000;25(4):689-699.

18. Haugstvedt J, Berger RA, Nakamura T, Neale P, Berglund L, An K. Relative contributions of the ulnar attachments of the triangular fibrocartilage complex to the dynamic stability of the distal radioulnar joint. *J Hand Surg Am*. 2006;31(3):445-451.

19. Nishiwaki M, Nakamura T, Nakao Y, Nagura T, Toyama Y. Ulnar shortening effect on distal radioulnar joint stability: a biomechanical study. *J Hand Surg Am*. 2005;30(4):719-726.

20. Nakamura T, Takayama S, Horiuchi Y, Yabe Y. Origins and insertions of the triangular fibrocartilage complex: a histological study. *J Hand Surg Br*. 2001;26(5):446-54.

21. Nakamura T, Yabe Y, Horiuchi Y. Dynamic changes in the shape of the triangular fibrocartilage complex during rotation demonstrated with high resolution magnetic resonance imaging. *J Hand Surg Br.* 1999;24(3):338-41.

22. Ishii S, Palmer AK, Werner FW, Short WH, Fortino MD. An anatomic study of the ligamentous structure of the triangular fibrocartilage complex. *J Hand Surg Br*. 1998;23(6):977-85.

23. Gofton WT, Gordon KD, Dunning CE, Johnson JA, King GJ. Comparison of distal radioulnar joint reconstructions using an active joint motion simulator. *J Hand Surg Br*. 2005;30(4):733-742.

24. Kleinman W, Graham T. The distal radioulnar joint capsule: clinical anatomy and role in posttraumatic limitation of forearm rotation. *J Hand Surg Am*. 1998 23(4):588-99

25. Watanabe H, Berger RA, An K, Berglund LJ, Zobitz ME. Stability of the distal radioulnar joint contributed by the joint capsule. *J Hand Surg Am*. 2004;29(6):1114-1120.

26. Linscheid RL. Biomechanics of the distal radioulnar joint. *Clin Orthop Relat Res.* 1992;(275):46-55.

27. Gordon KD, Dunning CE, Johnson JA, King GJ. Influence of the pronator quadratus and supinator muscle load on DRUJ stability. *J Hand Surg Am*. 2003;28(6):943-950.

28. Stuart PR. Pronator quadratus revisited. *J Hand Surg Br*. 1996;21(6):714-22.

29. Gordon KD, Dunning CE, Johnson JA, King GJ. Kinematics of ulnar head arthroplasty. *J Hand Surg Br*. 2003;28(6):551-558.

30. Sauerbier M, Fujita M, Hahn ME, Neale PG, Berger RA. The dynamic radioulnar convergence of the darrach procedure and the ulnar head hemiresection interposition arthroplasty: a biomechanical study. *J Hand Surg Br.* 2002;27(4):307-316.

31. Sauerbier M, Hahn ME, Berglund LJ, An K, Berger RA. Biomechanical evaluation of the dynamic radioulnar convergence after ulnar head resection, two soft tissue stabilization methods of the distal ulna and ulnar head prosthesis implantation. *Arch Orthop Trauma Surg.* 2011;131(1):15-26.

32. Spinner M, Kaplan EB. Extensor carpi ulnaris. Its relationship to the stability of the distal radio-ulnar joint. *Clin Orthop Relat Res*. 1970;68:124-9.

33. Iida A, Omokawa S, Akahane M, Kawamura K, Takayama K, Tanaka Y. Distal radioulnar joint stress radiography for detecting radioulnar ligament injury. *J Hand Surg Am*. 2012;37(5):968-974.

34. Watanabe H, Berger RA, Berglund LJ, Zobitz ME, An K. Contribution of the Interosseous Membrane to Distal Radioulnar Joint Constraint. *J Hand Surg Am*. 2005;30(6):1164-1171.

35. Noda K, Goto A, Murase T, Sugamoto K, Yoshikawa H, Moritomo H. Interosseous membrane of the forearm: an anatomical study of ligament attachment locations. *J Hand Surg Am*. 2009;34(3):415-422.

36. Kitamura T, Moritomo H, Arimitsu S, Berglund LJ, Zhao KD, An KN, Rizzo M. The biomechanical effect of the distal interosseous membrane on distal radioulnar joint stability: a preliminary anatomic study. *J Hand Surg Am*. 2011;36(10):1626-1630.

37. Tay SC, van Riet R, Kazunari T, Koff MF, Amrami KK, An KN, Berger RA. A method for in-vivo kinematic analysis of the forearm. *J Biomech*. 2008;41(1):56-62.

38. Palmer AK, Werner FW, Glisson RR, Murphy DJ. Partial excision of the triangular fibrocartilage complex. *J Hand Surg Am*. 1988;13(3):391-394.

39. Tay SC, van Riet R, Kazunari T, Amrami KK, An KN, Berger RA. In-vivo kinematic analysis of forearm rotation using helical axis analysis. *Clin Biomech*. 2010;25(7):655-659.

40. Tomaino MM. The importance of the pronated grip x-ray view in evaluating ulnar variance. *J Hand Surg Am*. 2000;25(2):352-7.

41. Gordon KD, Kedgley AE, Ferreira LM, King GJ, Johnson JA. Design and implementation of an instrumented ulnar head prosthesis to measure loads in vitro. *J Biomech*. 2006;39(7):1335-1341.

42. Shaaban H, Giakas G, Bolton M, Williams R, Wicks P, Scheker LR, Lees VC. The load-bearing characteristics of the forearm: pattern of axial and bending force transmitted through ulna and radius. *J Hand Surg Br*. 2006;31(3):274-279.

43. Shaaban H, Giakas G, Bolton M, Williams R, Scheker LR, Lees VC. The distal radioulnar joint as a load-bearing mechanism - a biomechanical study. *J Hand Surg Am*. 2004;29(1):85-95.

44. Miura T, Firoozbakhsh K, Cheema T, Moneim MS, Edmunds M, Meltzer S. Dynamic effects of joint-leveling procedure on pressure at the distal radioulnar joint. *J Hand Surg Am*. 2005;30(4):711-718.

45. Nishiwaki M, Nakamura T, Nagura T, Toyama Y, Ikegami H. Ulnar-shortening effect on distal radioulnar joint pressure: a biomechanical study. *J Hand Surg Am*. 2008;33(2):198-205.

46. Jung JM, Baek GH, Kim JH, Lee YH, Chung MS. Changes in ulnar variance in relation to forearm rotation and grip. *J Hand Surg Br*. 2001;83(7):1029-33.

47. Medoff RJ. Essential radiographic evaluation for distal radius fractures. *Hand Clin*. 2005;21(3):279-288.

48. Schuind FA, Linscheid RL, An KN, Chao EY. A normal data base of posteroanterior roentgenographic measurements of the wrist. *J Bone Joint Surg Am*. 1992;74(9):1418-29.

49. Bhattacharyya R, Morgan BS, Mukherjee P, Royston S. Distal radial fractures: the significance of the number of instability markers in management and outcome. *Iowa Orthop J.* 2014;34:118-22.

50. Adams BD. Effects of radial deformity on distal radioulnar joint mechanics. *J Hand Surg Am*. 1993;18(3):492-8.

51. Kihara H, Palmer AK, Werner FW, Short WH, Fortino MD. The effect of dorsally angulated distal radius fractures on distal radioulnar joint congruency and forearm rotation. *J Hand Surg Am*. 1996;21(1):40-7.

52. Fraser GS, Ferreira LM, Johnson JA, King GJ. The effect of multiplanar distal radius fractures on forearm rotation: in vitro biomechanical study. *J Hand Surg Am*. 2009;34(5):838-848.

53. Hirahara H, Neale PG, Lin Y, Cooney WP, An K. Kinematic and torque-related effects of dorsally angulated distal radius fractures and the distal radial ulnar joint. *J Hand Surg Am*. 2003;28(4):614-621.

54. Nishiwaki M, Welsh M, Gammon B, Ferreira LM, Johnson JA, King GJ. Distal radioulnar joint kinematics in simulated dorsally angulated distal radius fractures. *J Hand Surg Am*. 2014;39(4):656-663.

55. Brogren E, Wagner P, Petranek M, Atroshi I. Distal radius malunion increases risk of persistent disability 2 years after fracture: a prospective cohort study. *Clin Orthop Relat Res*. 2013;471(5):1691-1697.

56. Prommersberger K, Pillukat T, Mühldorfer M, van Schoonhoven J. Malunion of the distal radius. *Arch Orthop Trauma Surg*. 2012;132(5):693-702.

57. Baeyens J, van Glabbeek F, Goossens M, Gielen J, van Roy P, Clarys JP. In vivo 3D arthrokinematics of the proximal and distal radioulnar joints during active pronation and supination. *Clin Biomech*. 2006;21 Suppl 1:S9-12.

58. Ekenstam FA, Hagert CG. Anatomical studies on the geometry and stability of the distal radio ulnar joint. *Scand J Plast Reconstr Surg.* 1985;19(1):17-25.

59. Shaaban H, Giakas G, Bolton M, et al. Contact area inside the distal radioulnar joint: effect of axial loading and position of the forearm. *Clin Biomech.* 2007;22(3):313-318.

60. Crisco JJ, Moore DC, Marai GE, Laidlaw DH, Akelman E, Weiss AP, Wolfe SW. Effects of distal radius malunion on distal radioulnar joint mechanics - an in vivo study. *J Orthop Res*. 2007;25(4):547-555.

61. Stormont TJ, An KN, Morrey BF, Chao EY. Elbow joint contact study: comparison of techniques. *J Biomech*. 1985;18(5):329-36.

62. Eckstein F, Löhe F, Müller-Gerbl M, Steinlechner M, Putz R. Stress distribution in the trochlear notch. A model of bicentric load transmission through joints. *J Bone Joint Surg Br*. 1994;76(4):647-53.

63. Eckstein F, Löhe F, Hillebrand S, Bergmann M, Schulte E, Milz S, Putz R. Morphomechanics of the humero-ulnar joint: I. Joint space width and contact areas as a function of load and flexion angle. *Anat Rec*. 1995;243(3):318-26.

64. Liew VS, Cooper IC, Ferreira LM, Johnson JA, King GW. The effect of metallic radial head arthroplasty on radiocapitellar joint contact area. *Clin Biomech*. 2003;18(2):115-8.

65. Moungondo F, El Kazzi W, van Riet R, Feipel V, Rooze M, Schuind F. Radiocapitellar joint contacts after bipolar radial head arthroplasty. *J Shoulder Elbow Surg*. 2010;19(2):230-235.

66. Wan L, Deasla R, Rubash H, Li G. Determination of in-vivo articular cartilage contact areas of human talocrural joint under weightbearing conditions. *Osteoarthritis Cartilage*. 2006;14(12):1294-1301.

67. Lalone EA, Peters TM, King GW, Johnson JA. Accuracy assessment of an imaging technique to examine ulnohumeral joint congruency during elbow flexion. *Comput Aided Surg*. 2012;17(3):142-152.

68. Viegas SF, Tencer AF, Cantrell J, Chang M, Clegg P, Hicks C, O'Meara C, Williamson JB. Load transfer characteristics of the wrist. Part I. The normal joint. *J Hand Surg Am*. 1987;12(6):971-978.

69. Pogue DJ, Viegas SF, Patterson RM, Peterson PD, Jenkins DK, Sweo TD, Hokanson JA. Effects of distal radius fracture malunion on wrist joint mechanics. *J Hand Surg Am*. 1990;15(5):721-7.

70. Short WH, Werner FW, Green JK, Masaoka S. Biomechanical evaluation of ligamentous stabilizers of the scaphoid and lunate. *J Hand Surg Am*. 2002;27(6):991-1002.

71. Deshmukh SC, Shanahan D, Coulthard D. Distal radioulnar joint incongruity after shortening of the ulna. *J Hand Surg Br*. 2000;25(5):434-8.

72. Van Ginckel AV, Van Ginckel A, Roosen P, Almqvist KF, Verstraete K, Witvrouw E. Effects of in vivo exercise on ankle cartilage deformation and recovery in healthy volunteers: an experimental study. *Osteoarthritis Cartilage*. 2011;19(9):1123-1131.

73. Marai GE, Laidlaw DH, Demiralp C, Andrews S, Grimm CM, Crisco JJ. Estimating Joint Contact Areas and Ligament Lengths From Bone Kinematics and Surfaces. *IEEE Trans Biomed Eng*. 2004;51(5):790-799.

74. Cohen ZA, McCarthy DM, Kwak SD, Legrand P, Fogarasi F, Ciaccio EJ, Ateshian GA. Knee cartilage topography, thickness, and contact areas from MRI: in-vitro calibration and in-vivo measurements. *Osteoarthritis Cartilage*. 1999 Jan;7(1):95-109.

75. Goto A, Moritomo H, Murase T, Oka K, Sugamoto K, Arimura T, Nakajima Y, Yamazaki T, Sato Y, Tamura S, Yoshikawa H, Ochi T. In vivo elbow biomechanical analysis during flexion: three-dimensional motion analysis using magnetic resonance imaging. *J Shoulder Elbow Surg*. 2004;13(4):441-447.

76. Boyer PJ, Massimini DF, Gill TJ, Papannagari R, Stewart SL, Warner JP, Li G. In vivo articular cartilage contact at the glenohumeral joint: preliminary report. *J Orthop Sci*. 2008;13(4):359-365.

77. Fischer KJ, Johnson JE, Waller AJ, McIff TE, Toby EB, Bilgen M. MRI-based modeling for radiocarpal joint mechanics: validation criteria and results for four specimen-specific models. *J Biomech Eng*. 2011;133(10):101004.

78. Smith DK, Cooney WP 3rd, An KN, Linscheid RL, Chao EY. The effects of simulated unstable scaphoid fractures on carpal motion. *J Hand Surg Am*. 1989;14(2 Pt. 1):283-91.

79. Dunning CE, Duck TR, King GJ, Johnson JA. Simulated active control produces repeatable motion pathways of the elbow in an in vitro testing system. *J Biomech*. 2001;34(8):1039-48.

80. Soslowsky LJ, Flatow EL, Bigliani LU, Pawluk RJ, Ateshian GA, Mow VC. Quantitation of in situ contact areas at the glenohumeral joint: a biomechanical study. *J Orthop Res*. 1992;10(4):524-34.

81. Maurer CR Jr, Maciunas RJ, Fitzpatrick JM. Registration of head CT images to physical space using a weighted combination of points and surfaces. *IEEE Trans Med Imaging*. 1998;17(5):753-61.

82. Ma B, Ellis RE. Robust registration for computer-integrated orthopedic surgery: Laboratory validation and clinical experience. *Med Image Anal*. 2003;7(3):237-250.

83. Besl P, McKay ND. A method for registration of 3-D shapes. *IEEE Trans. on Pattern Analysis and Machine Intelligence*. 1992; 14(2): 239–256.

84. Mcdonald CP, Brownhill JR, King GW, Johnson JA, Peters TM. A comparison of registration techniques for computer- and image-assisted elbow surgery. *Comput Aided Surg*. 2007;12(4):208-214.

85. Lalone EA, McDonald CP, Ferreira LM, Peters TM, King GW, Johnson JA. Development of an image-based technique to examine joint congruency at the elbow. *Comput Methods Biomech Biomed Engin*. 2013;16(3):280-290.

86. Willing R, Lapner M, Lalone EA, King GW, Johnson JA. Development of a computational technique to measure cartilage contact area. *J Biomech*. 2014;47(5):1193-7.

87. Lalone EA, Giles JW, Alolabi B, Peters TM, Johnson JA, King GW. Utility of an image-based technique to detect changes in joint congruency following simulated joint injury and repair: an in vitro study of the elbow. *J Biomech*. 2013;46(4):677-82.

88. Baeyens J, van Glabbeek F, Goossens M, Gielen J, van Roy P, Clarys J. In vivo 3D arthrokinematics of the proximal and distal radioulnar joints during active pronation and supination. *Clin Biomech*. 2006;21 Suppl 1:S9-12.

89. Wolfe S, Crisco J, Katz L. A non-invasive method for studying in vivo carpal kinematics. *J Hand Surg Br*. 1997;22(2):147-152.

90. Moritomo H, Murase T, Goto A, Oka K, Sugamoto K, Yoshikawa H. Capitate-based kinematics of the midcarpal joint during wrist radioulnar deviation: an in vivo three-dimensional motion analysis. *J Hand Surg Am*. 2004;29(4):668-675.

91. Goto A, Moritomo H, Murase T, Oka K, Sugamoto K, Arimura T, Masumoto J, Tamura S, Yoshikawa H, Ochi T. In vivo three dimensional wrist motion analysis using magnetic resonance imaging and volume based registration. *J Orthop Res*. 2005;23(4):750-6.

92. Johnson JE, Lee P, McIff TE, Toby EB, Fischer KJ. Scapholunate ligament injury adversely alters in vivo wrist joint mechanics: An MRI-based modeling study. *J Orthop Res*. 2013;31(9):1455-1460.

93. Rainbow MJ, Kamal RN, Leventhal E, Akelman E, Moore DC, Wolfe SW, Crisco JJ. In vivo kinematics of the scaphoid, lunate, capitate and third metacarpal in extreme wrist flexion and extension. *J Hand Surg Am*. 2013;38(2):278-288.

94. Rainbow MJ, Kamal RN, Leventhal E, Akelman E, Moore DC, Wolfe SW, Crisco JJ. In vivo 3-dimensional analysis of dorsal intercalated segment instability deformity secondary to scapholunate dissociation: a preliminary report. *J Hand Surg Am*. 2013;38(7):1346-1355.

95. Kaufmann R, Pfaeffle J, Blankenhorn B, Stabile K, Robertson D, Goitz R. Kinematics of the midcarpal and radiocarpal joints in radioulnar deviation: an in vitro study. *J Hand Surg Am*. 2005;30(5):937-942.

96. Lalone EA, McDonald CP, Ferreira LM, Peters TM, King GW, Johnson JA. Development of an image-based technique to examine joint congruency at the elbow. *Comput Methods Biomech Biomed Engin*. 2013;16(3):280-290.

97. Murray PM, Adams JE, Lam J, Osterman AL, Wolfe S. Disorders of the distal radioulnar joint. *Instr Course Lect*. 2010;59:295-311.

98. Ehman EC, Hayes ML, Berger RA, Felmlee JP, Amrami KK. Subluxation of the distal radioulnar joint as a predictor of foveal triangular fibrocartilage complex tears. *J Hand Surg Am*. 2011;36(11):1780-1784.

99. Moriya T, Aoki M, Iba K, OzasaY, Wada T, Yamashita T. Effect of triangular ligament tears on distal radioulnar joint instability and evaluation of three clinical tests: a biomechanical study. *J Hand Surg Br*. 2009;34(2):219-223.

100. Fujitani R, Omokawa S, Akahane M, Iida A, Ono H, Tanaka Y. Predictors of distal radioulnar joint instability in distal radius fractures. *J Hand Surg Am*. 2011;36(12):1919-1925.

101. Kim JP, Park MJ. Assessment of distal radioulnar joint instability after distal radius fracture: comparison of computed tomography and clinical examination results. *J Hand Surg Am*. 2008;33(9):1486-1492.

102. Kleinman WB. Distal radius instability and stiffness: common complications of distal radius fractures. *Hand Clin*. 2010;26(2):245-264.

103. Shinohara T, Tatebe M, Okui N, Yamamoto M, Kurimoto S, Hirata H. Arthroscopically assisted repair of triangular fibrocartilage complex foveal tears. *J Hand Surg Am*. 2013;38(2):271-277.

104. Atzei A, Rizzo A, Luchetti R, Fairplay T. Arthroscopic foveal repair of triangular fibrocartilage complex peripheral lesion with distal radioulnar joint instability. *Tech Hand Up Extrem Surg*. 2008;12(4):226-35.

105. Manz S, Wolf MB, Leclère FM, Hahn P, Bruckner T, Unglaub F. Capsular imbrication for posttraumatic instability of the distal radioulnar joint. *J Hand Surg Am*. 2011;36(7):1170-1175.

106. Lawler E, Adams BD. Reconstruction for DRUJ Instability. *Hand (N Y)*. 2007;2(3):123-126.

107. Adams B, Berger R. An anatomic reconstruction of the distal radioulnar ligaments for posttraumatic distal radioulnar joint instability. *J Hand Surg Am*. 2002;27(2):243-51.

108. Petersen MS, Adams BD. Biomechanical evaluation of distal radioulnar reconstructions. *J Hand Surg Am*. 1993;18(2):328-34.

109. Saito T, Nakamura T, Nagura T, Nishiwaki M, Sato K, Toyama Y. The effects of dorsally angulated distal radius fractures on distal radioulnar joint stability: a biomechanical study. *J Hand Surg Br*. 2013;38(7):739-745.

110. Ferreira LM, Greeley GS, Johnson JA, King GW. Load transfer at the distal ulna following simulated distal radius fracture malalignment. *J Hand Surg Am*. 2015;40(2):217-23.

2   Comparison of Inter-cartilage Distance as a Method for Assessing Arthrokinematics of the Distal Radioulnar Joint

2.1   Overview

This chapter presents an in-vitro cadaveric study examining the accuracy of Inter-cartilage Distance as a tool for measuring contact area in the distal radio-ulnar joint. It is compared to other direct methods of contact area measurement including Casting and Tekscan®.

2.2   Introduction

As documented in Chapter 1, the distal radioulnar joint (DRUJ) is a complex, diarthrodial articulation which, in conjunction with the proximal radioulnar joint (PRUJ), allows for the radius to rotate around the ulna during forearm pronation and supination. There is a combined rolling and sliding motion that occurs as the radius glides over the ulnar head[1]. The area of ulnar head contacting the sigmoid notch changes depending on the position of forearm rotation[2].

The joint contact pattern between the radius and ulna at the DRUJ is of interest, as it gives insight into how the radius and ulna interact during normal and pathological conditions. Ulnar-sided wrist pain is a common complaint in patients with a malunion of the distal radius[3]. Incongruence at the DRUJ may contribute to these symptoms. Thus, it is important to be able to quantify changes in the arthrokinematics of this articulation so this phenomenon can be further studied.

As described previously in Chapter 1 (Section 1.6), there are both direct and indirect methods described to assess joint contact. Direct methods include casting, pressure sensitive film and piezoresistive array pressure sensors (Tekscan®). The "direct" gold standard for accuracy is considered to be casting[4]. This reference standard technique is limited in its applicability as the joint capsule must be sectioned to remove the cast, and only static positions can be examined. Piezoresistive array pressure sensors represent an evolution, permitting dynamic evaluation of contact area and pressure during joint motion. This film is prone to deformation when placed inside a joint and also by virtue

of the thickness of the sensors introduces error in the measurements[5]. Additionally, joint capsule and potentially other stabilizing structures have to be sectioned to interpose film within the joint. In response to this, non-destructive techniques have been developed to study joint contact. Indirect methods involve the creation of 3-dimensional models from CT or MRI volumetric datasets. A proximity map can be made from these models using software algorithms, and joint contact can be extrapolated[6,7,8,9].

Previous authors have investigated the contact relationship between the radius and ulna at the DRUJ. Malone et al.[10] utilized Tekscan to characterize *in vitro* contact changes in the DRUJ throughout an arc of forearm rotation. Contact area was maximal from neutral to 30° of supination and ranged from 20-50 mm^2 under 10 kg of axial load. Non-invasive methods for investigating joint contact continue to be developed. Chen et al.[11] examined the centre of contact *in vivo*, between the radius and ulna at the DRUJ throughout complete pro-supination, using CT models and an inter-bone distance algorithm. In pronation, the contact centre was dorsal and distal in the sigmoid notch. During the transition to supination the contact centre moved volarly and proximally. The total distance travelled by the contact centre on the sigmoid notch during a 180° arc of forearm rotation was 6.8 mm along the volar-dorsal axis and 2.3 mm along the proximal-distal axis. The authors did not report on absolute contact area measurements in this study. This study highlights the need for further investigation into non-invasive measurements of DRUJ contact area.

A novel indirect technique, Inter-cartilage Distance (ICD), has been recently developed. ICD has been validated in the elbow[12], but not against a gold standard for the DRUJ. Its advantage compared with other indirect techniques which rely on distances between osseous structures lies in the use of cartilage-bearing models. The cartilage morphology is derived from CT scans performed with air contrast. These models incorporate regional variations in cartilage thickness This technique has been shown to be highly accurate with a thickness error of only 0.3 mm[13]. The models are registered using fiducials to the experimental specimens which have had their kinematics quantified using an optical tracking system. Contact maps are then created using different thresholds for

proximity between the models, allowing for values of contact area and location to be ascertained during motion.

In this study of DRUJ contact, we sought to compare ICD with two accepted direct techniques: casting and piezoresistive array pressure sensors (Tekscan®). These modalities were used to evaluate cartilage contact area in the DRUJ of an *in vitro* model. Our hypothesis was that Inter-cartilage Distance (ICD) would be able to reproducibly characterize contact area in the DRUJ, while being responsive to the effect of load and forearm position. We also hypothesized that casting and Tekscan would produce similar measurements for DRUJ contact area.

2.3 Methods

2.3.1 Experimental Protocol – Specimen Preparation

Testing was performed on one (29-year-old female) cadaveric forearm specimen with no clinical or CT evidence of osteoarthritis. The specimen was amputated at the mid-humeral level and stored at -20 °C. It was thawed for 18 hours at room temperature (22 °C) and then prepared for mounting in a custom-designed testing apparatus. The apparatus was CT-compatible and permitted reproducible forearm positioning in pronation with the metacarpals clamped in a calibrated ring (Figure 2.1).

Pulley Suspension System

**Forearm
Positioning
Ring**

Infrared Marker Triad
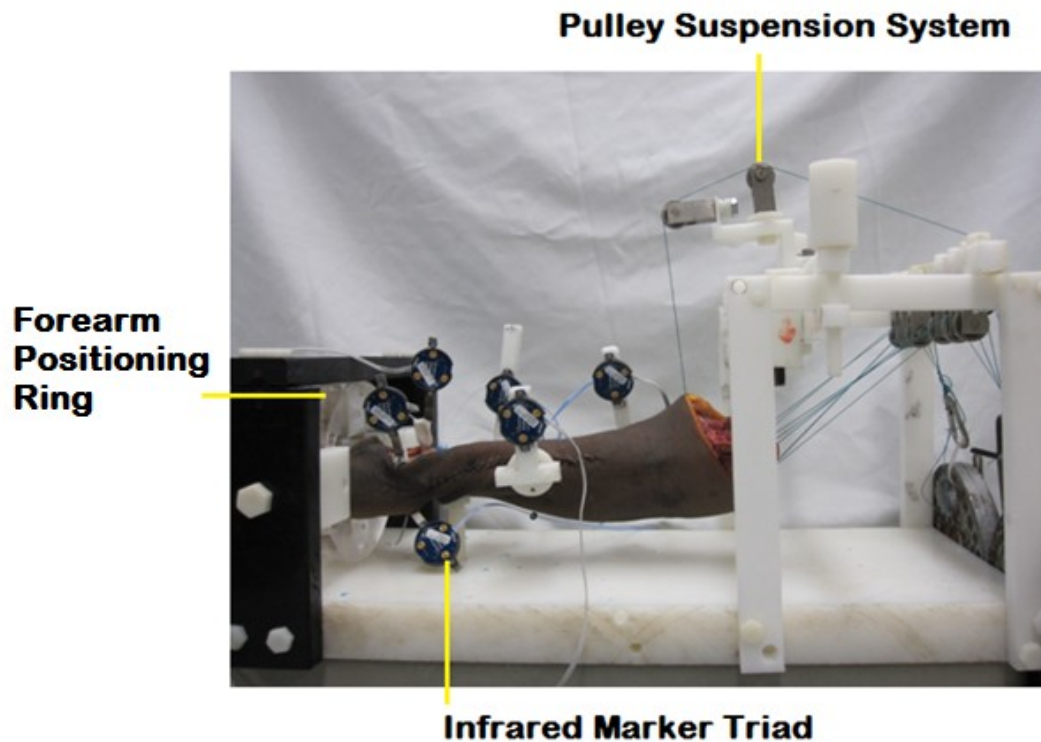
Figure 2.1 Specimen mounted in custom forearm testing apparatus with tendons loaded using a pulley suspension system. Infrared marker triads are mounted on the radius and ulna © Braden Gammon.

Static tendon loading was made possible through a pulley suspension system attached to the posterior aspect of the device which allowed the weights to be kept out of the gantry during CT imaging (Figure 2.2).
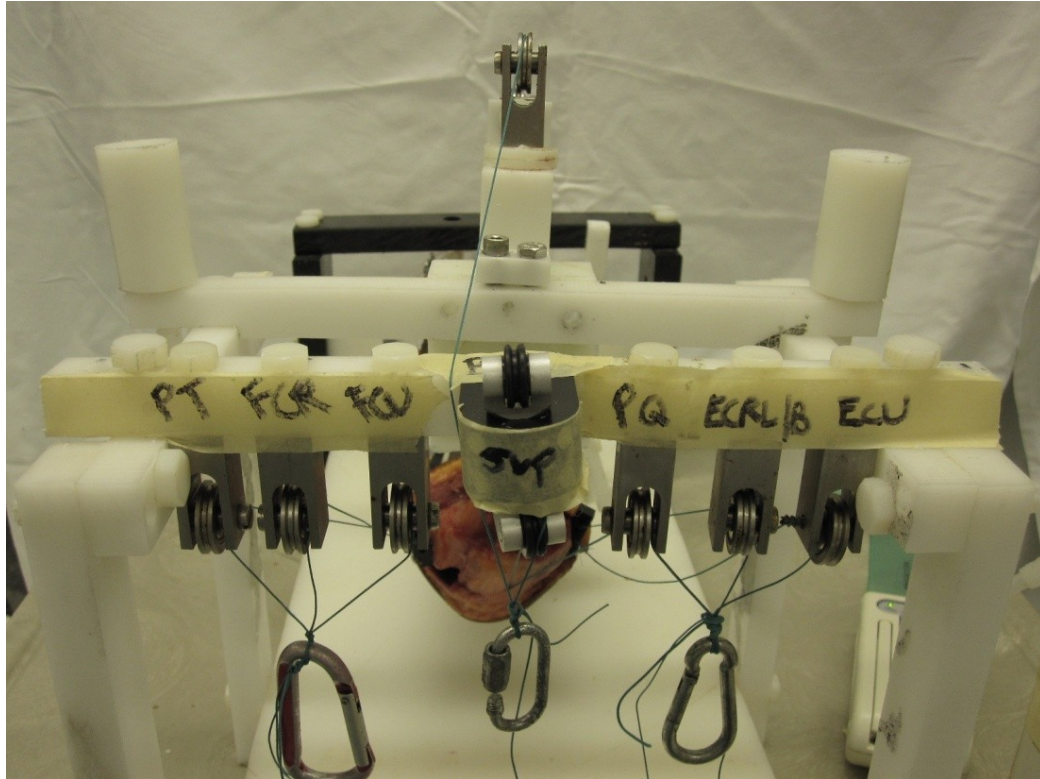
Figure 2.2 **The pulley suspension system of the apparatus, which allowed for tendon loading and the weights to be kept outside the zone of CT scanning © Braden Gammon**

The distal tendons of the wrist extensors (extensor carpi radialis longus and brevis [ECRL/B], extensor carpi ulnaris [ECU]), wrist flexors (flexor carpi radialis [FCR], flexor carpi ulnaris [FCU]), pronator teres [PT] and biceps [BI] were then sutured using #2 Ethibond (Ethibond Excel, Ethicon Inc., Somerville, NJ, USA). Sutures were passed through alignment guides that were appropriately placed to reproduce the physiologic line of action of each muscle. ECRL/B and ECU were routed through a lateral epicondyle sleeve, while PT, FCR and FCU were routed through a medial epicondyle sleeve. The supinator [SUP] muscle was modeled by placing a suture anchor in the radial tuberosity and routing the attached suture through a drill hole in the radial aspect of the ulna, through an intraosseous tunnel in the ulnar canal to exit the proximal olecranon. The action of pronator quadratus [PQ] was reproduced by placing a transosseous bone bridge at its radial origin which served as an anchor point for suture. The #2 Ethibond was then

routed through a Delrin® sleeve in the ulnar insertion and out the posterior aspect of the olecranon. The humerus was secured to the apparatus using a clamp. The fingers were amputated and the denuded metacarpal heads were clamped in a calibrated positioning ring.

Contact area in the DRUJ was quantified using Casting, Tekscan and ICD. The cadaveric specimen was tested in the following conditions: 1) tendons loaded in 45° forearm pronation 2) tendons loaded in 80° forearm pronation 3) tendons unloaded in 80° forearm pronation. 3 trials were performed with each contact area measurement method. The specific protocol for each measurement method is detailed below.

2.3.2 Experimental Protocol – Non-invasive contact measurement

The apparatus was positioned such that the long axis of the forearm was in line with the CT scanner gantry. During testing, the specimen was CT-scanned using a GE Discovery CT750 HD scanner (GE Health care, Pewaukee, WI, USA) at 120 kV and 292 mAs with a slice thickness of 0.625 mm (in-plane pixel size 0.320 mm). Baseline test conditions were created at the DRUJ by sectioning the dorsal and proximal joint capsule, which were then sutured anatomically using #2 Ethibond. Volumetric data was obtained of the specimen in the following conditions: intact state, DRUJ capsule sectioned and repaired: 45° forearm pronation-loaded, 80° forearm pronation-unloaded, and 80° forearm pronation-loaded.

2.3.3 Experimental Protocol – Invasive contact measurement

Once CT scanning was complete, infrared marker triads were affixed to the radius and ulna, (Figure 2.1c) and were tracked using an Optotrak Certus (Northern Digital Inc, Waterloo, Ontario, Canada) optical motion capture system with a 3D accuracy of 0.1 mm[14]. Two forearm positions (45° and 80° of pronation) were tested, in either the loaded or unloaded condition. When loaded, the sutured tendons were tensioned to 20 N using free weights suspended via pulleys (Figure 2.3).

Infrared Marker Triad

Pulley Suspension System with Weights

Medial Epicondyle Alignment Guide
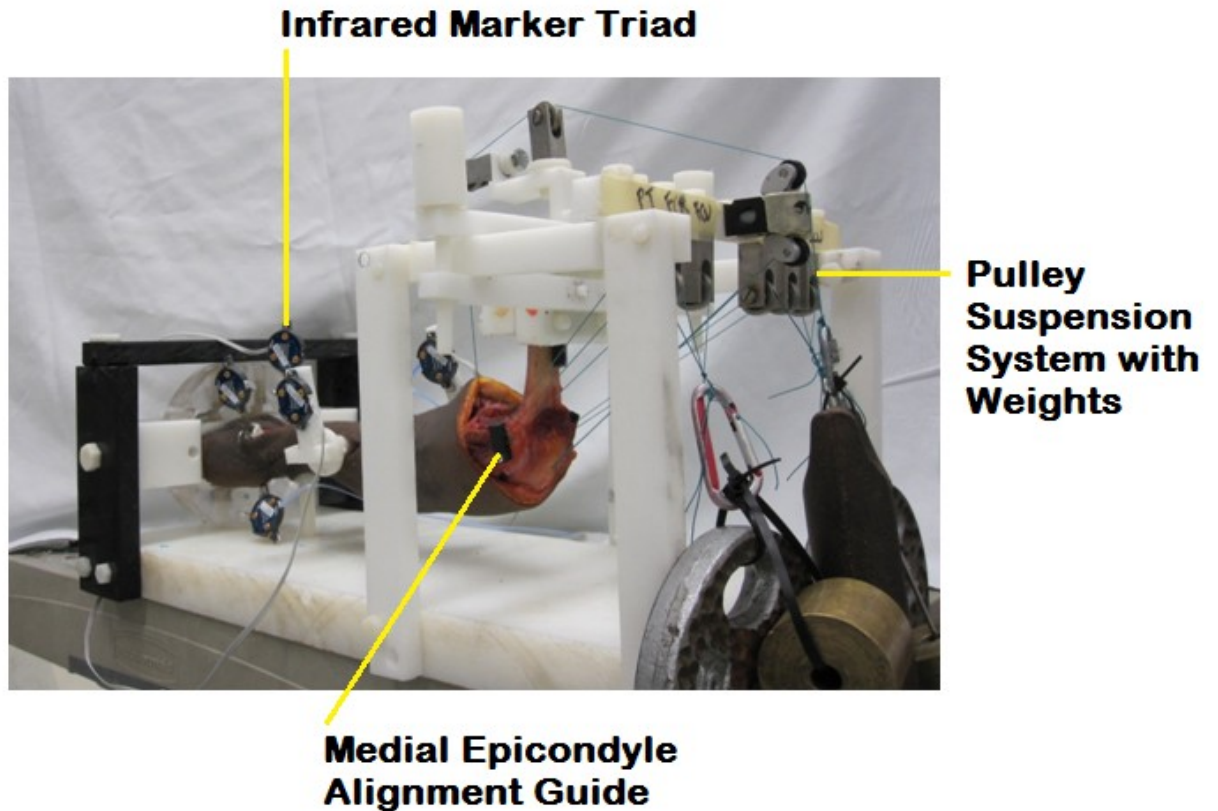
Figure 2.3 Forearm specimen mounted in the custom positioning apparatus with tendons loaded © Braden Gammon.

For each testing condition of forearm position and loading state, the DRUJ sutures were removed, and approximately 2.5 mL of casting material (Reprosil® Vinyl Polysiloxane Impression Material, DENTSPLY International Inc., Milford, DE, USA) was evenly distributed across the contact surfaces of the distal radius and ulna in the DRUJ using a syringe. The capsule was re-sutured and loads were applied (Figure 2.4).
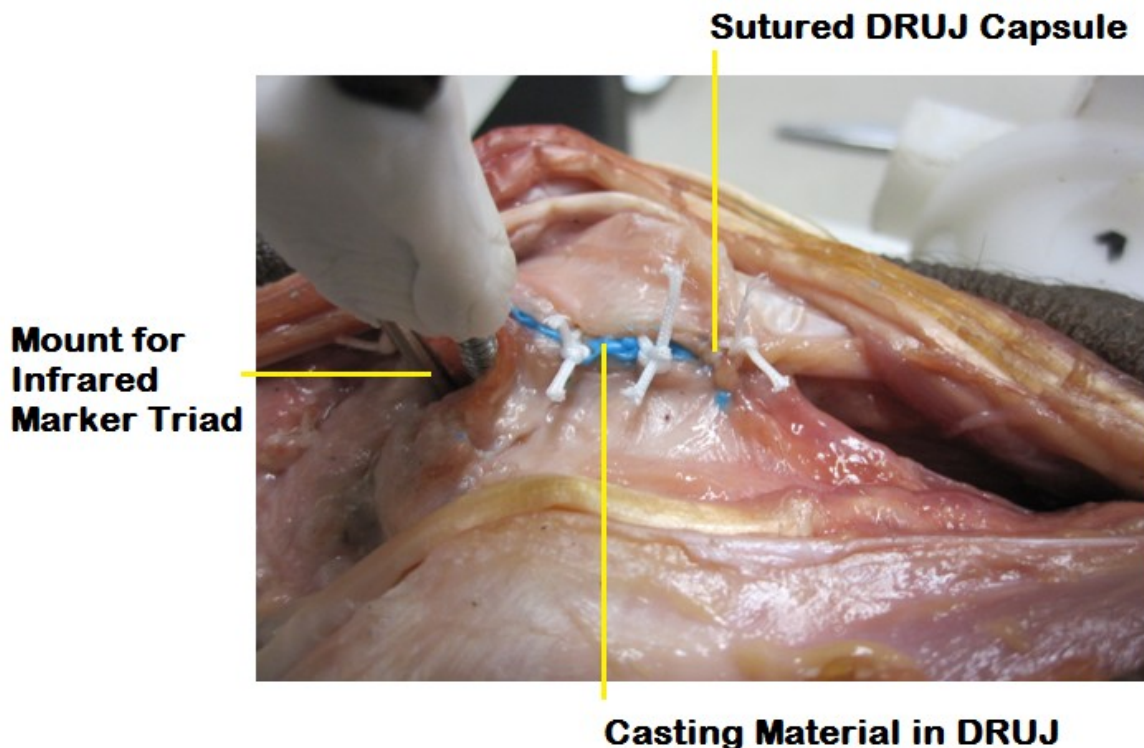
Figure 2.4 Demonstrating casting material inside the distal radioulnar joint with the DRUJ capsule sutured © Braden Gammon.

The positions of the radius and ulna were recorded using the optical tracking system. The forearm was kept in a static pronated position for approximately 20 minutes, allowing the casting material to fully cure. The loads were disconnected, the DRUJ was distracted and the solidified casting was removed. 3 castings were performed for each testing condition, with optical position data captured during each casting session with and without casting material in the joint. The contact area was also measured for each test condition with every casting session using a high resolution pressure and force measurement sensor (4000 series Tekscan sensor, TekScan Inc., South Boston, MA, Figure 2.5). The sensor was equilibrated at 2 points (1 bar and 3 bar) with mid-1 sensitivity (I-Scan version 5.76I; TekScan Inc.) on a custom air pressure sensor equilibrator. Total matrix area was 2480 mm^2 (24 × 64 sensels, 30.5 mm × 81.3 mm), with a spatial resolution of 1.612 mm^2 per sensel.
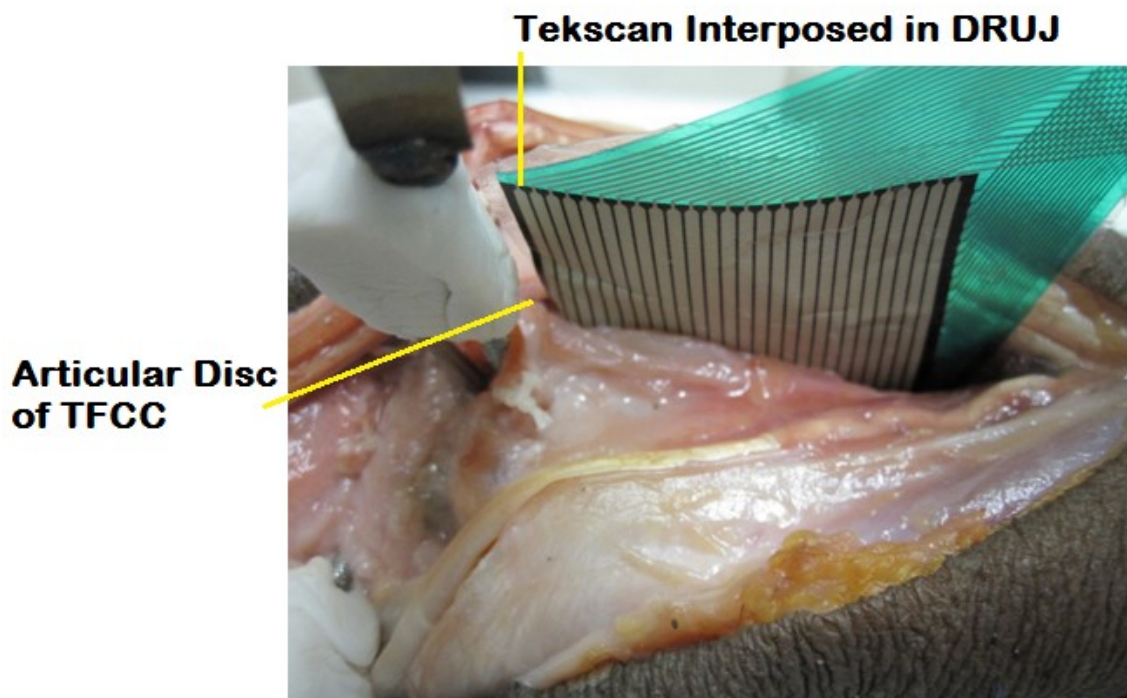
Figure 2.5 The Tekscan® sensor inserted in the DRUJ and abutting the articular disc of the TFCC distally for measurement of contact area © Braden Gammon.

Following the testing protocol, the radius and ulna were separated and denuded (Figure 2.6).

Figure 2.6 The radius and ulna, denuded of soft tissue with mounted infrared optical marker triads © Braden Gammon.

Four spherical nylon fiducial markers were attached to each bone. 19 mm fiducials were attached to non-articular regions of the ulna using #10-24 threaded nylon rods, while 4.76 mm fiducials were used for the distal radius using #2-56 threaded nylon rods (Figure 2.7).
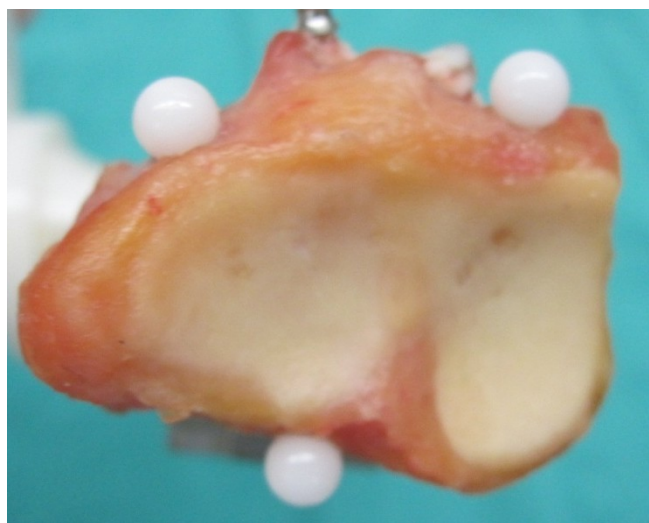
Figure 2.7 **The distal radius with spherical nylon fiducial markers mounted using buried intraosseous threaded nylon rods © Braden Gammon.**

Their locations were digitized with respect to that bone's corresponding motion tracker using an appropriately-sized calibrated cupped stylus. The articular surfaces of the distal radius and ulna were also digitized with respect to their corresponding motion trackers using a pointed stylus tool.

2.3.4 Measurement of DRUJ Contact Area – Casting

The denuded radius and ulna were re-approximated in both 45° and 80° of pronation using a goniometer, re-creating their position in the apparatus. The appropriate casts were then interposed, fit congruently to the distal ulna and then pinned in place (Figure 2.8).

Figure 2.8 **The casting of the DRUJ affixed to the ulnar head with pins © Braden Gammon**

Regions devoid of casting material were deemed to be areas of contact and were digitized as 3D point clouds using a calibrated stylus and previously described technique[15,16] (Figure 2.9). The denuded bones were then CT scanned in air using the imaging parameters described in section 2.3.2[12], to ascertain the specimen's cartilage thickness and permit the creation of 3-D bone models.
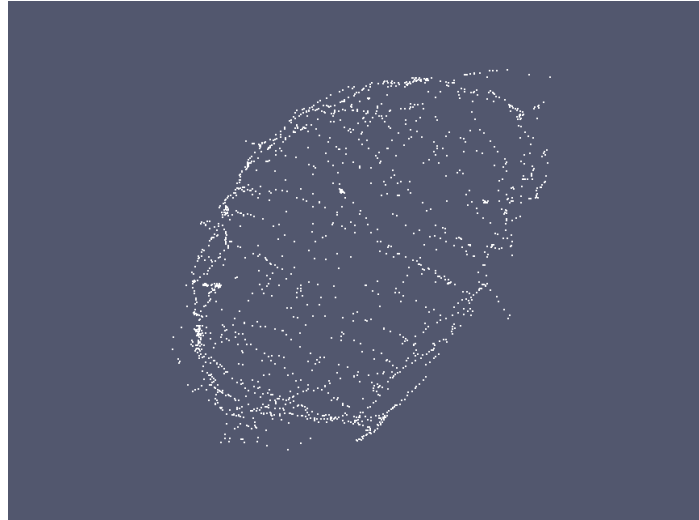
Figure 2.9 **A sample 3-D point cloud of the area devoid of cast material, designated as the contact patch, as digitized on the distal ulna and depicted in ParaView (Paraview 4.0.1 Parallel Visualization Application, open source) © Braden Gammon.**

The digitized 3-D point cloud was used as an overlay template on the registered ulna model in Meshlab (Meshlab v 1.3.2, Visual Computing Laboratory) to create a registered contact patch from which a final contact area was derived in mm^2 (Figure 2.10).
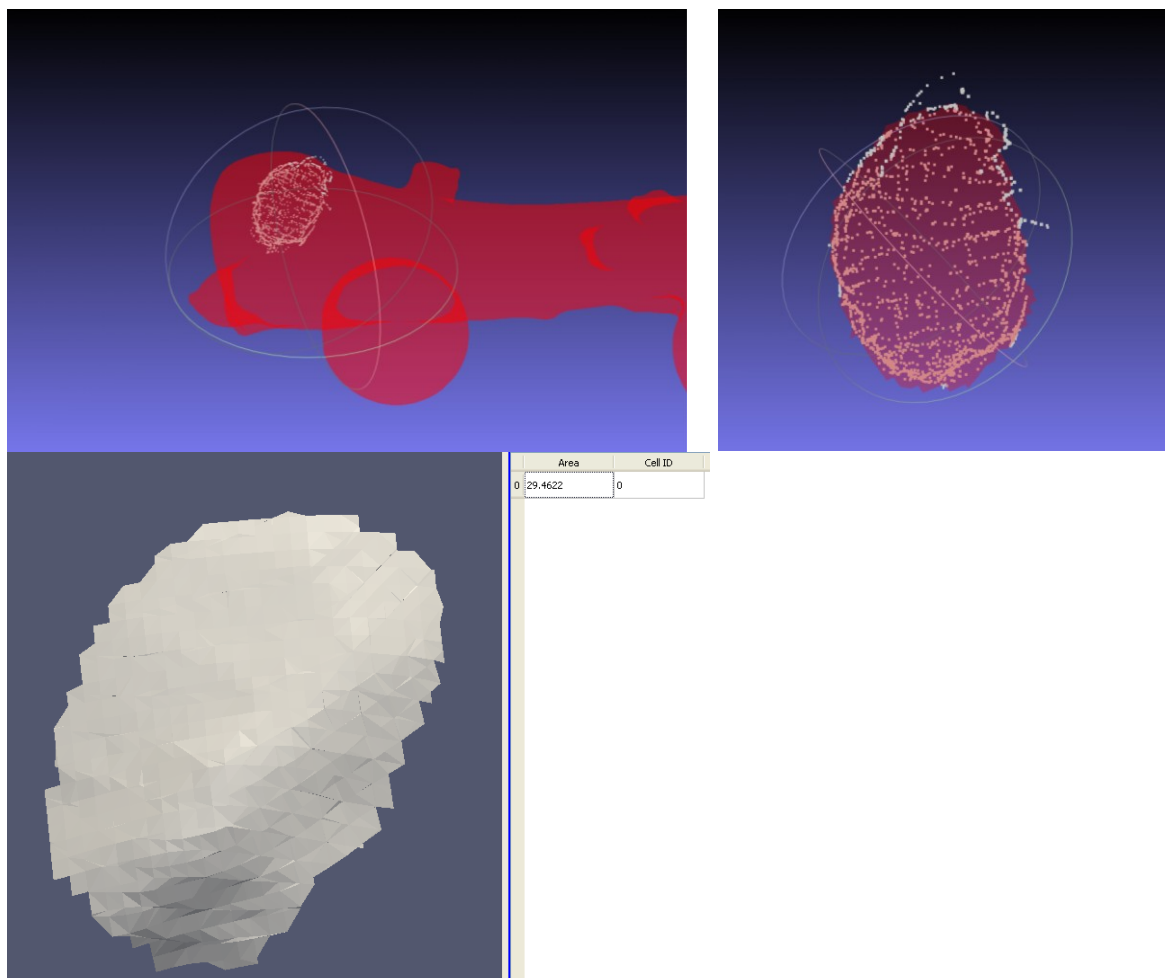
Figure 2.10 **The digitized point cloud derived from the cast contact area was superimposed on the registered ulna model (top left and right). That area of model was isolated in MeshLab and its contact area was subsequently calculated using ParaView (bottom) © Braden Gammon.**

2.3.5 Measurement of DRUJ Contact Area – Inter-cartilage Distance Algorithm (ICD)

2.3.5.1 ICD: Segmentation and Bone Surface Modelling

CT image data of the denuded bones with fiducials were imported for manipulation into Mimics (version 15.1, Materialise, Leuven, Belgium). Cartilage geometries were determined using minimum threshold-based segmentation (cartilage

models = –700 HU). Models were wrapped, resulting in sealed hollow shell models that were exported in the stereolithography (.STL) format[13].

2.3.5.2   ICD: Cartilage Model Registration

The models were repositioned from CT images to anatomic-based coordinate systems using a rigid-body registration algorithm. This registration procedure used the fiducials digitized during the experiment as well as the fiducials imaged using CT after the experimental protocol as homologous points[17].

2.3.5.3   ICD: Joint Contact Area Measurement Based on Cartilage Overlap

Using the optical tracking data recorded during the experiment, the 3D models were re-assembled to their corresponding positions and orientations. The contact surfaces were then analyzed for regions of cartilage model overlap. These areas were assumed to be the regions where contact occurred (Figure 2.11).
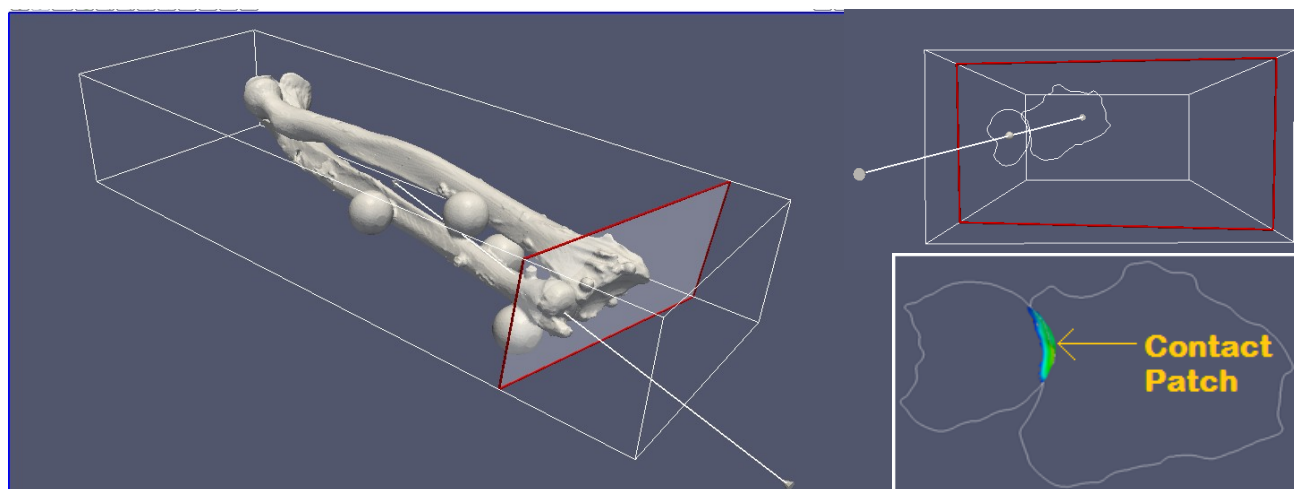
Figure 2.11 Registered 3-D bone models depicted in Paraview. A cross-sectional slice is obtained perpendicular to the axis of forearm rotation at level of the contact centroid (calculated by ICD) demonstrating regions of cartilage-cartilage overlap © Braden Gammon.

2.3.5.4   Data Analysis

The effect of measurement method, forearm position and loading on contact area in the DRUJ was examined. Trials were matched for forearm position and loading, and a one-way repeated measures ANOVA was performed, with the independent variable of measurement method (Tekscan vs. Casting vs. ICD). The effect of forearm rotation angle was examined using a two-way ANOVA, with trials matched for loading and independent variables of measurement method and degree of pronation (45° vs. 80°). The effect of loading was evaluated using a two-way ANOVA, with trials matched for forearm position and independent variables of measurement method and loading (loaded vs. unloaded). A Greenhouse-Geisser correction was applied. Statistical significant was set at $p < 0.05$. We used a Bonferroni correction for multiple comparisons to compare main effects.

2.4   Results

Contact area in the DRUJ was quantified using Casting, Tekscan and ICD. Figure 2.12 displays the typical output of each modality for contact measurement. Data presented is the mean DRUJ contact area ± standard deviation unless otherwise specified. There was no measureable contact in the 45° pronated unloaded condition; thus it was not included in our final analysis.
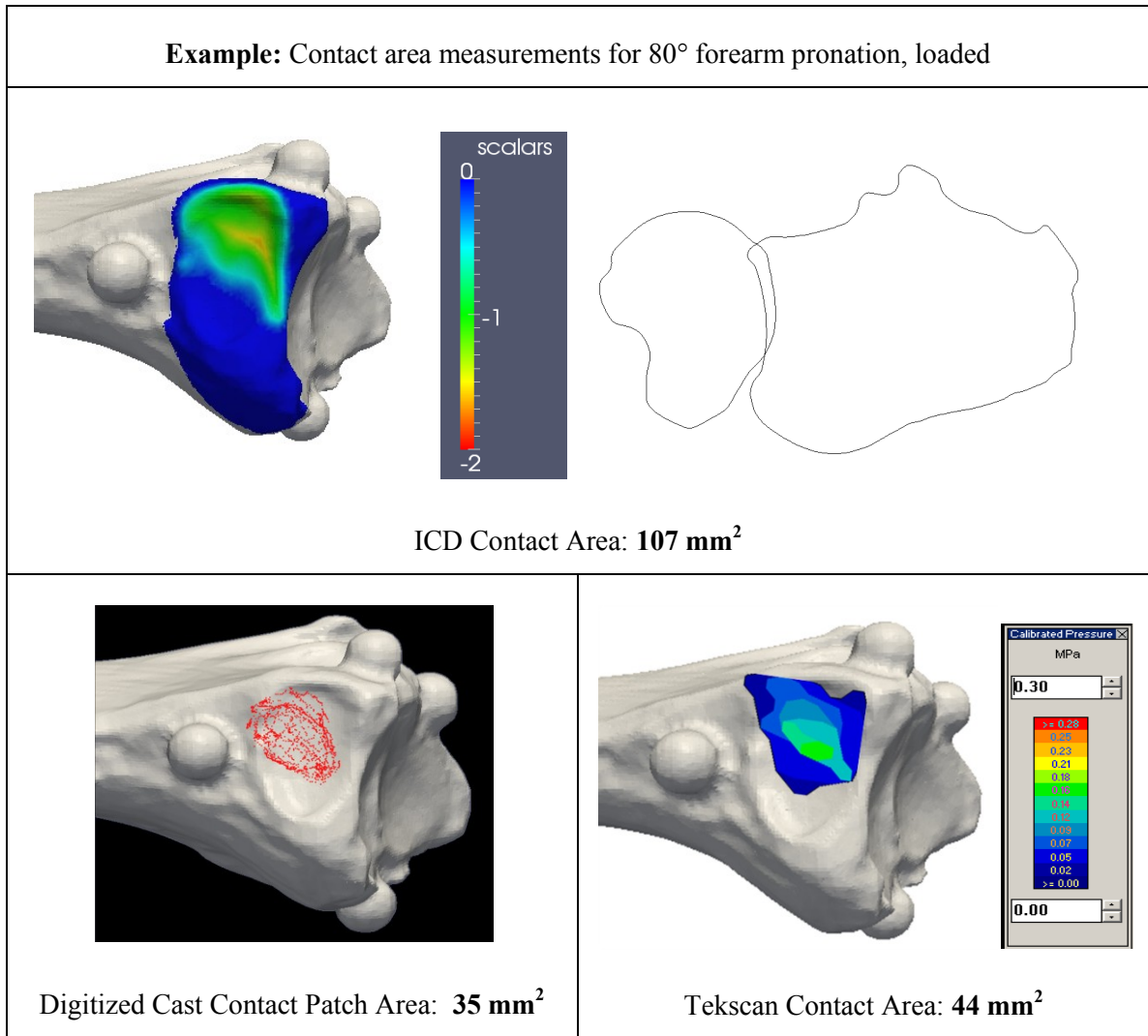
Figure 2.12 **The output for each modality used to measure contact area in the distal radioulnar joint, including Inter-cartilage Distance (top), Casting (bottom left), and Tekscan (bottom right) © Braden Gammon.**

With the forearm loaded in 45° of pronation, contact area in the DRUJ was measured as 35 ± 9 mm^2 using Tekscan, 33 ± 4 mm^2 using casting, and 99 ± 3 mm^2 using ICD (Figure 2.13).
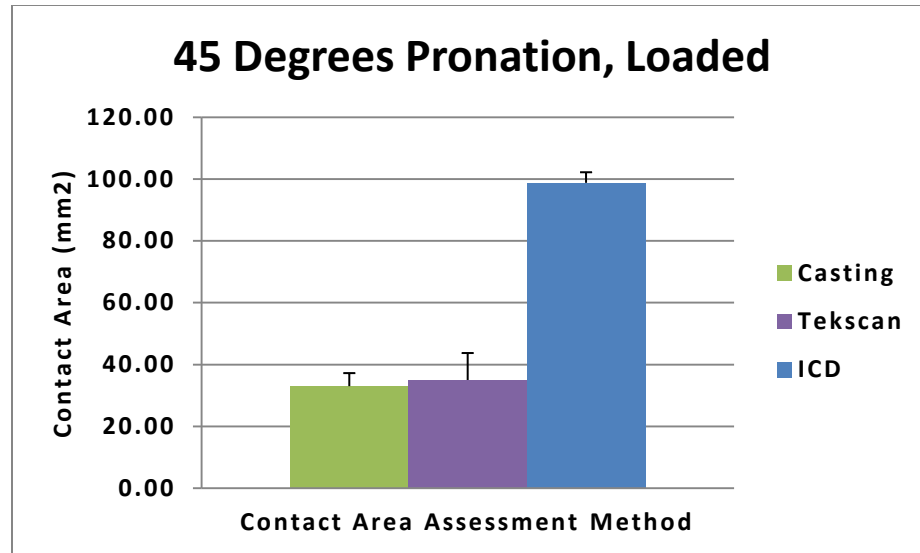
Figure 2.13 **Mean (+1 SD) of DRUJ contact area in the loaded condition with the forearm 45°**
pronated for Casting, Tekscan and ICD. **© Braden Gammon**

With the forearm loaded in 80° of pronation, contact area in the DRUJ was measured as
42 ± 7 mm^2 using Tekscan, 34 ± 2 mm^2 using casting, and 99 ± 7 mm^2 using ICD (Figure
2.14).
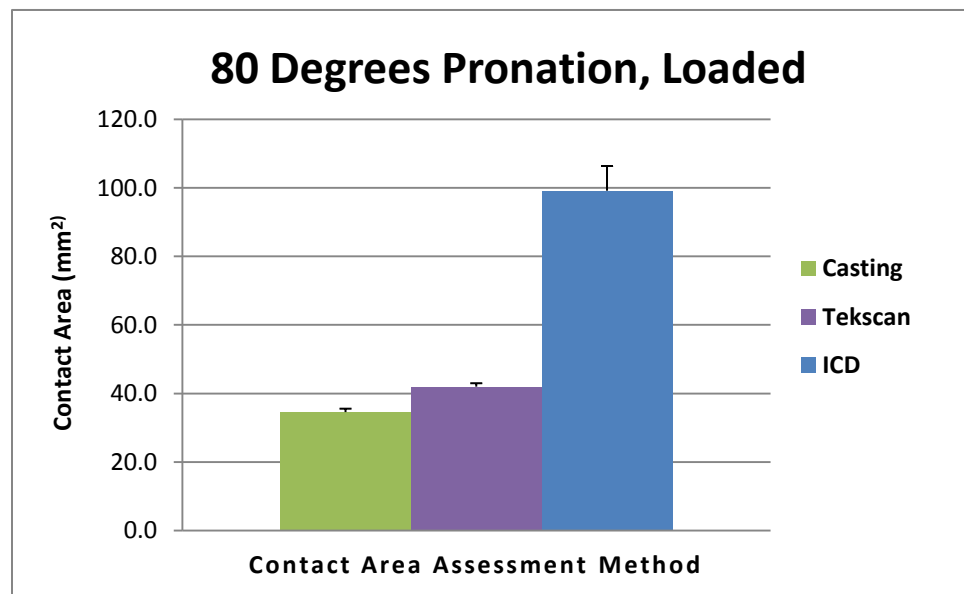
Figure 2.14 **Mean (+1 SD) of DRUJ contact area in the loaded condition with the forearm 80°**
pronated for Casting, Tekscan and ICD. **© Braden Gammon**

With the forearm unloaded in 80° of pronation, contact area in the DRUJ was measured as 26 ± 7 mm^2 using Tekscan, 15 ± 1 mm^2 using Casting, and 100 ± 4 mm^2 using ICD (Figure 2.15).
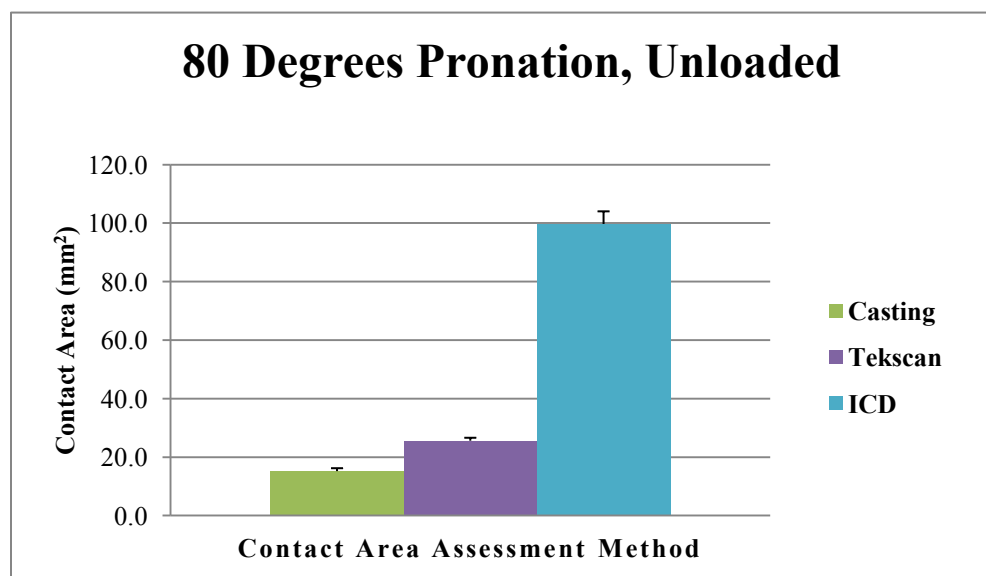
Figure 2.15 **Mean (+1 SD) of DRUJ contact area in the unloaded condition with the forearm 80° pronated for Casting, Tekscan and ICD. © Braden Gammon**

There was no significant difference between DRUJ contact area values comparing Tekscan to Casting (p=0.25). Both methods demonstrated significantly lower values for mean DRUJ contact area when compared with ICD (p=<0.0001). There was no significant effect observed from forearm rotation angle (p=0.73). Loading had a significant effect on contact area values in the DRUJ measured by Tekscan and Casting, with higher values under loaded conditions (p=0.024). The standard deviation values calculated for Tekscan, Casting and ICD were all low, indicating that each contact area measurement was reproducible.

2.5   Discussion

To date, Casting has been considered the gold standard for quantifying joint contact area[18]. Tekscan represents an alternative modality, which has been used previously in the DRUJ[10]. Tekscan has been shown to activate the entire sensel in areas of marginal contact and artificially expand contact patches[5]. This study however, noted no significant

difference between mean values for contact area derived from Tekscan compared with Casting.

Both Casting and Tekscan noted a significant increase in contact between the loaded and unloaded conditions. The increase in contact area seen between loaded and unloaded states is likely secondary to increased force transmission across the DRUJ[19], which subsequently compresses the cartilaginous surfaces together. Cartilage deforms at areas of contact *in vivo*[20] and this deformation/flattening of cartilage is likely responsible for the greater contact area seen with increased load. We did not identify a significant change in the ICD contact area with increased load. Over the loads tested, the cartilage may have deformed at the level of the articulation, without changing the position of the bones or trackers significantly. Thus, the ICD calculation, which is based on position data, may not have reflected the increased load. Alternatively, both Casting and Tekscan interposed material in the joint which may have distracted the articulation. This might have artificially reduced the contact area measured in the unloaded condition, and with load this effect would have been negated. Finally, this may relate to our low sample size.

Forearm rotation angle did not have a significant effect on contact area values in the DRUJ when controlling for measurement method. This was unanticipated, as other studies have noted a significant effect of forearm rotation on DRUJ contact area[10]. It is difficult to know why a difference was not detected here, but likely relates to only 2 angles being tested, which are both in pronation and relatively close in position. We may have detected a difference if a greater number of angles were tested in more specimens.

The most striking outcome was the quantitative difference between contact area measurements derived from ICD when compared with Tekscan and Casting. ICD results were over three-fold higher on average when compared to other modalities. This was surprising, as a recent study revealed close agreement between Casting and ICD with cartilage models[12]. There are many reasons that could explain the difference in contact area measurement seen between modalities. Discrepancies in the ICD contact measurement can be broadly related to the methods used to create the CT-based models,

the techniques used in the registration of these models and subsequent proximity mapping with the ICD algorithm.

First, the models are based off CT imaging in air of the denuded specimens at the end of the test day. These have been in contact with silicone cast material and bathed in saline over a period of 12 hours, which may have caused swelling of the cartilage. This may have expanded the cartilage thickness of the model and artificially increased the contact area from the ICD measurement (Figure 2.16). Moreover, the slice thickness of the CT scan at 0.625 mm introduces the possibility of volume averaging artifact at the periphery of the joint surfaces, which could also expand the model size. The net result is that the accuracy of cartilage models is reported to be 0.3 mm in the literature, and this margin of difference would affect the ICD contact area measurements[13].

Second, the registration of the model to the specimen can be inaccurate (Figure 2.16), with a registration error up to 0.88 mm[17]. This can result from subtle changes in positioning of the fiducial markers over the course of testing, in the case of fiducial based registration.

Third, ICD accuracy is contingent upon the optical tracking system used for characterizing the position and orientation of the radius and ulna *in vitro*. If a direct line of sight between the camera and the position sensors is maintained and kept within 2.5 m, then reported accuracy is up to 0.1 mm[13,14]. Error can be higher however, if conditions vary from this scenario (Figure 2.16).

Fourth, the cartilage models used for proximity mapping were captured via CT in an un-deformed state. The sigmoid notch and ulnar head have different radii of curvature (Chapter 1, Figure 1.8). When the radius and ulna models are reassembled during the ICD algorithm and overlapped in an un-deformed state (Figure 2.12, top right), the pattern of contact and morphology/area of the contact patch may different from how they truly interact *in vivo*, where the cartilage is flattened/deformed[20].

| 54.7mm^2 | 91.1mm^2 | 116.8mm^2 |
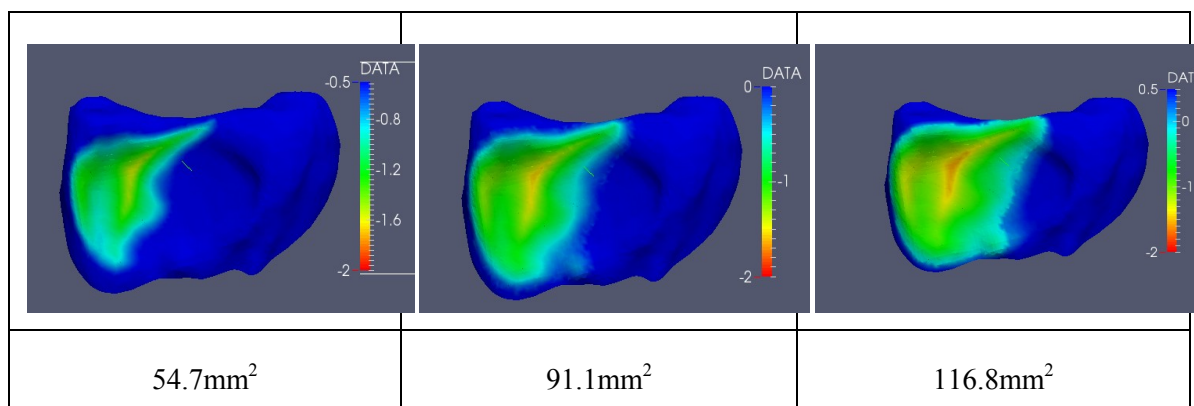
Figure 2.16 **The radius and ulna models are re-assembled during the ICD algorithm, where cartilage overlap is measured. Error in the thickness of the models will change this measurement, as will error in their position which may result from inaccurate registration or optical tracking. The effect of these errors can be significant on the magnitude of the contact patch measured. This figure demonstrates how an increase or decrease in 0.5 mm of model overlap affects the contact measurement.**

It should be noted that Casting and Tekscan have inherent limitations as well. The sectioning of capsuloligamentous structures to introduce the casting material or Tekscan film may reduce the forces approximating the DRUJ and diminish the measured contact area. Moreover, the introduction of material into the joint with an inherent stiffness and thickness could distract the articular surfaces apart, leading to an underestimation of joint contact. Tekscan is prone to other aspects which affect its reliability as well, including incorrect calibration, liquid saturation, migration of the sensor position and shear stress across the film causing deformation[21]. These all could have played a role in our study.

This study was limited by its use of one specimen for the trials performed. Different conclusions may have been reached with higher numbers of specimens and trials, as our results are underpowered.

Qualitatively, we noted good agreement between the morphology of contact patches derived from Tekscan, Casting and ICD. This is reassuring, and points to the quantitative differences in contact patch size being related to error in the proximity of the models caused by registration or tracking with ICD, or error inherent to the invasive techniques as described above. Figure 2.14 characterizes these observations. The original contact

patch is depicted in A. The area completely devoid of cast material is designated as the contact patch, but is smallest in magnitude. The calculated ICD patch is shown in B. If a very thin (0.5 mm) region of central cast material is removed (C), both the size and shape of the contact patch are similar when compared with ICD (D). This shows the impact of how a small degree of error in the proximity of the models could dramatically change the contact area values.

To summarize, Inter-cartilage distance is effective in producing reproducible contact area measurements for the distal radio-ulnar joint through non-invasive measures. ICD values were higher than those noted with invasive methods for contact assessment, and this may relate to error from 3-D modeling, registration or optical tracking, as well as the sensitivity of the DRUJ to the interposition of materials to measure contact. Further investigation is warranted to optimize the accuracy of ICD by minimizing error in these domains. Inter-cartilage Distance remains a robust tool for measuring arthrokinematics, and has proven valid for use in the wrist. Having assessed its efficacy in measuring contact area in static positions, we propose future *in vitro* evaluation of the DRUJ using ICD in a dynamic capacity and also study how soft tissue and osseous injuries of the wrist may affect arthrokinematics.

A

Cast Void Contact Area: **34 mm^2**

B

ICD Contact Area: **96 mm^2**

C

Thin and Void Cast Contact Area: **105 mm^2**

D
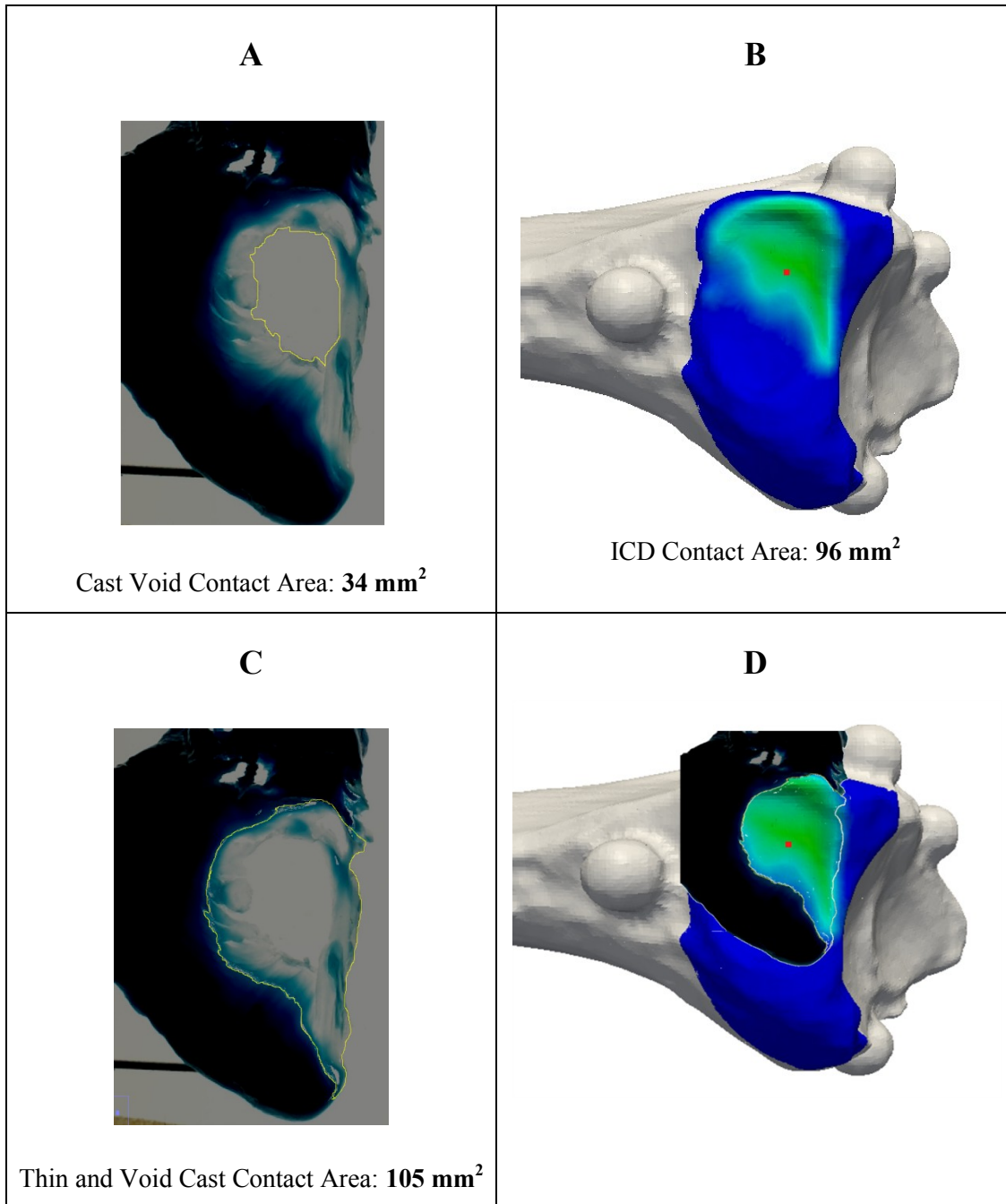
Figure 2.17 A DRUJ casting and its corresponding ICD contact map from the loaded, 45° forearm pronated condition are shown. In A, the original casting is depicted and the central area devoid of cast is designated as the contact patch. In B, the ICD contact patch is shown. In C, the original cast is depicted, but surrounding casting material with a thickness less than 0.5 mm has been subtracted from the image. In D, this modified thin and void cast overlies the ICD contact patch, showing excellent agreement in the size (ICD: 96 mm^2 vs. Thin and Void Cast: 105 mm^2) and shape © Braden Gammon.

2.6   References

1. Ekenstam FA, Hagert CG. Anatomical studies on the geometry and stability of the distal radio ulnar joint. *Scand J Plast Reconstr Surg.* 1985;19(1):17-25.

2. Ekenstam FA. Anatomy of the distal radioulnar joint. *Clin Orthop Relat Res.* 1992;(275):14-8.

3. Brogren E, Wagner P, Petranek M, Atroshi I. Distal radius malunion increases risk of persistent disability 2 years after fracture: a prospective cohort study. *Clin Orthop Relat Res.* 2013;471(5):1691-1697.

4. Stormont TJ, An KN, Morrey BF, Chao EY. Elbow joint contact study: comparison of techniques. *J Biomech.* 1985;18(5):329-36.

5. Drewniak EI, Crisco JJ, Spenciner DB, Fleming BC. Accuracy of circular contact area measurements with thin-film pressure sensors. *J Biomech.* 2007;40(11):2569-72.

6. Marai GE, Crisco JJ, Laidlaw DH. A kinematics-based method for generating cartilage maps and deformations in the multi-articulating wrist joint from CT images. *Conf Proc IEEE Eng Med Biol Soc.* 2006;1:2079-82.

7. Goto A, Moritomo H, Murase T, Oka K, Sugamoto K, Arimura T, Nakajima Y, Yamazaki T, Sato Y, Tamura S, Yoshikawa H, Ochi T. In vivo elbow biomechanical analysis during flexion: three-dimensional motion analysis using magnetic resonance imaging. *J Shoulder Elbow Surg.* 2004;13(4):441-447.

8. Anderst WJ, Tashman S. A method to estimate in vivo dynamic articular surface interaction. *J Biomech.* 2003;36(9):1291-9.

9. Wan L, Deasla R, Rubash H, Li G. Determination of in-vivo articular cartilage contact areas of human talocrural joint under weightbearing conditions. *Osteoarthritis Cartilage.* 2006;14(12):1294-1301.

10. Malone PS, Cooley J, Morris J, Terenghi G, Lees CV. The biomechanical and functional relationships of the proximal radioulnar joint, distal radioulnar joint, and interosseous ligament. *J Hand Surg Br.* 2015 Jun;40(5):485-93.

11. Chen YR, Tang JB. In vivo gliding and contact characteristics of the sigmoid notch and the ulna in forearm rotation. *J Hand Surg Am*. 2013;38(8):1513-1519.

12. Willing R, Lapner M, Lalone EA, King GW, Johnson JA. Development of a computational technique to measure cartilage contact area. *J Biomech*. 2014;47(5):1193-7.

13. Lalone EA, Willing RT, Shannon HL, King GW, Johnson JA. Accuracy assessment of 3D bone reconstructions using CT: an intro comparison. *Med Eng Phys*. 2015;37(8):729-38

14. Certus O. Research-Grade Motion Capture. *Manufacturer's Manual*. 2011:1-8.

15. Lalone EA, Peters TM, King GW, Johnson JA. Accuracy assessment of an imaging technique to examine ulnohumeral joint congruency during elbow flexion. *Comput Aided Surg*. 2012;17(3):142-52

16. Willing RT, Lalone EA, Shannon H, Johnson JA, King GW. Validation of a finite element model of the human elbow for determining cartilage contact mechanics. *J Biomech*. 2013;46(10):1767-71.

17. Lalone EA, Peters TM, King GW, Johnson JA. Accuracy assessment of an imaging technique to examine ulnohumeral joint congruency during elbow flexion. *Comput Aided Surg*. 2012;17(3):142-52.

18. Stormont TJ, An KN, Morrey BF, Chao EY. Elbow joint contact study: comparison of techniques. *J Biomech*. 1985;18(5):329-36.

19. Shaaban H, Giakas G, Bolton M, Williams R, Wicks P, Scheker LR, Lees VC. The load-bearing characteristics of the forearm: pattern of axial and bending force transmitted through ulna and radius. *J Hand Surg Br*. 2006;31(3):274-279.

20. Wan L, Deasla R, Rubash H, Li G. Determination of in-vivo articular cartilage contact areas of human talocrural joint under weightbearing conditions. *Osteoarthritis Cartilage*. 2006;14(12):1294-1301.

21. Wilharm A, Hurschler C, Dermitas T, Bohnsack M. Use of Tekscan K-scan sensors for retropatellar pressure measurement avoiding errors during implantation and the effects of shear forces on the measurement precision. *Biomed Res Int*. 2013;2013:829171

3   Arthrokinematics of the distal radioulnar joint measured using Inter-cartilage Distance in an *in vitro* model

3.1   Overview

This chapter presents an in-vitro cadaveric study examining changes in contact patterns at the DRUJ using Inter-cartilage Distance (previously described in Chapter 2) as a measurement tool. Both the contact area and contact centroid for intact specimens are reported during simulated active and passive forearm rotation.

3.2   Introduction

Much of the current research examining contact mechanics of the distal radioulnar joint focuses on the effect of joint mal-alignment[1,2,3]. Altered DRUJ contact mechanics are thought to cause degenerative changes and arthritis following injury[4]. Kinematic studies have determined that under normal conditions the radius both rotates and translates relative to the ulna[5]. In supination, the ulnar head sits volar and proximal within the sigmoid notch, and in pronation it is relatively dorsal and distal[6,7]. Less is known about native cartilage contact mechanics of the distal radioulnar joint.

Previous techniques used to measure joint contact mechanics have relied on invasive procedures and are often limited to static positions. Common "direct" methods are joint casting[8,9,10], pressure sensitive film[11,12] and Tekscan[®13,14,15] . Tekscan[®] has been used to investigate contact relationships in the DRUJ during forearm rotation[13,14,15]. However, the utility of "direct" techniques is limited, as they may change the normal articular mechanics due to the need to section capsulo-ligamentous structures to access the joint's interior, and by virtue of the inherent thickness of the material interposed[9]. Novel, indirect methods of assessing joint contact have also been developed. "Indirect" techniques are non-invasive, and compare relative positions of CT or MRI-generated joint models using computational means and proximity mapping[16,17,18,19]. The interaction between the model surfaces can be calculated and used to characterize joint contact[20,21,22,23,24,25].

Inter-cartilage Distance (ICD), as introduced in Chapter 2, is a validated *in vitro* technique for assessing joint contact area which utilizes CT-based bone and cartilage

models, fiducial-based registration and optical tracking motion capture data[26]. It has not been previously used to examine distal radioulnar joint contact mechanics. The advantage of *in vitro* methodology is that experimental conditions are controlled and more permutations can be explored[27].

The purpose of this study was to use Inter-cartilage Distance to examine native distal radioulnar joint contact mechanics during simulated active and passive forearm rotation. Our hypotheses were: 1) the contact area and centroid location would change during forearm rotation; and 2) there would be a difference in the contact patterns between simulated active and passive motion.

3.3   Materials and Methods

3.3.1   Specimen Preparation

Testing was performed on 8 fresh frozen left cadaveric forearm specimens (mean age 60 years; range 29 to 75 years; 6 men and 2 women) with no clinical or CT evidence of osteoarthritis. The specimens were amputated at the mid-humeral level and stored at -20 °C. They were thawed for 18 hours at room temperature (22 °C) and then prepared for mounting. The fingers were disarticulated at the metacarpal-phalangeal joints. The distal tendons of the wrist extensors (extensor carpi radialis longus [ECRL], extensor carpi ulnaris [ECU]), wrist flexors (flexor carpi radialis [FCR], flexor carpi ulnaris [FCU]), pronator teres [PT] and biceps [BIC] were then sutured using #2 Ethibond (Ethibond Excel, Ethicon Inc., Piscataway, NJ, USA).

Sutures were passed through alignment guides that were appropriately placed to reproduce the physiologic line of action of each muscle. ECRL and ECU were routed through a lateral epicondyle sleeve, while PT, FCR and FCU were routed through a medial epicondyle sleeve. The supinator [SUP] was modeled by placing a suture anchor in the radial tuberosity and routing the attached suture through a Delrin® sleeve which traversed the supinator crest to the posterolateral aspect of the ulna.

Specimens were tested in a simulator capable of producing forearm rotation with simulated muscle loading (Figure 3.1). The humerus was rigidly secured to the simulator

using a clamp. The elbow was placed in 90° of flexion, and the ulna was transfixed to a static post on the simulator using two 2 mm partially threaded pins. A 3.5 mm partially threaded pin was inserted in the third metacarpal along the long axis of rotation of the forearm. This was centered in a ring affixed to the simulator, permitting pro-supination while preventing extremes of wrist flexion and extension. The sutures of ECRL, ECU, FCR, FCU and SUP were routed through alignment pulleys and attached to individual pneumatic actuators (Airpot Corporation, Norwalk, CT).

3.3.2   Simulation of Motion

Passive motion was tested first by manually rotating the forearm through a full arc of motion from pronation to supination. Active supination was initiated by attaching BIC to the servo motor (SM2315D; Animatic, Santa Clara, CA) set to motion control at a constant tendon velocity of 5 mm/sec. As the prime mover for supination, BIC provided 67% of the supination load while SUP was loaded simultaneously at 33% of the BIC load via a pneumatic actuator. PT was loaded at 20 N to provide a counterforce using an actuator. Supination trials began with the specimen in full forearm pronation, progressing to full supination. This muscle loading ratio was based on a previous investigation of forearm muscle EMG and cross-sectional area[28]. Constant tone loads of 10 N were applied to the FCU, FCR, ECU and ECRL to stabilize the wrist. Simultaneous pneumatic actuator loads were regulated by proportional pressure controllers (PPC, MAC Valves, Wixon, MI, USA) under computer control using custom programmed software (LabVIEW, National Instruments, Texas, USA).

3.3.3   Motion Tracking and Kinematic Data Acquisition

The specimens were tested with the wrist and DRUJ intact. Infrared marker triads ("optical tracking markers") were rigidly affixed to the distal radius, proximal radius and ulna using custom Delrin® pedestals and the arc of simulated active supination was tracked using an Optotrak Certus (Northern Digital Inc, Waterloo, Ontario, Canada) optical motion capture system with a 3D accuracy of 0.1 mm[29]. For each test condition, kinematic data was recorded for all motion trials.
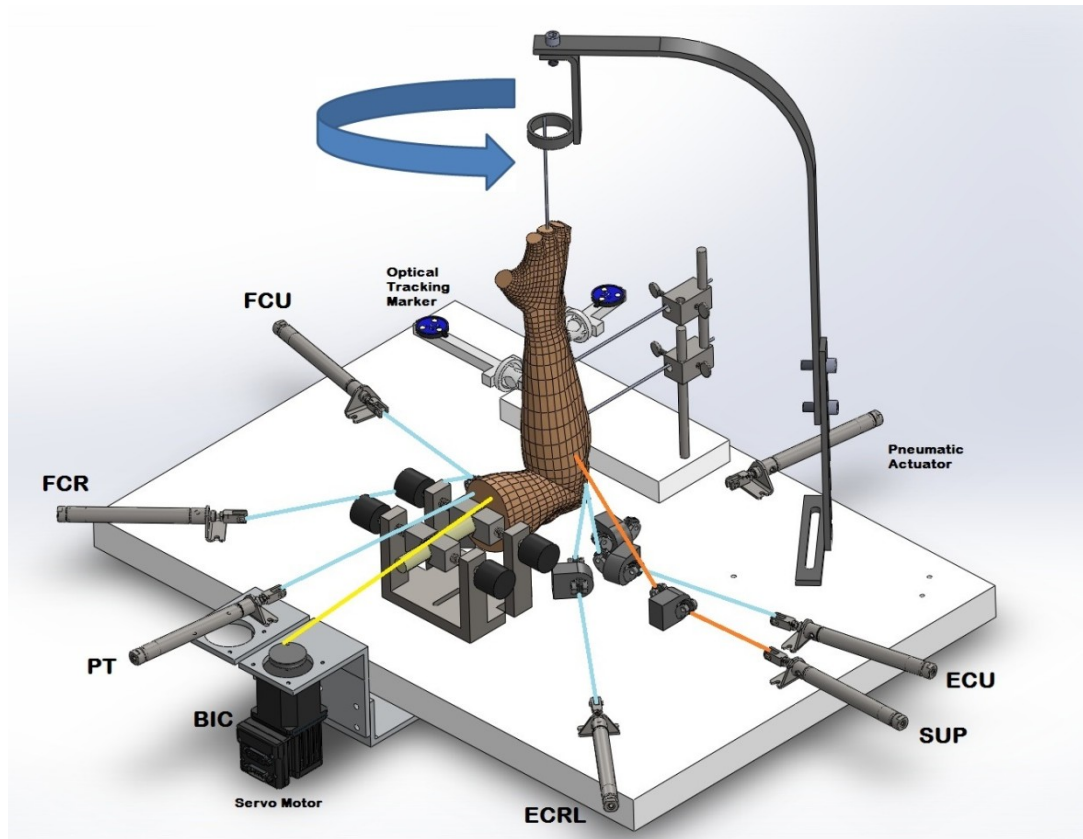
Figure 3.1 **Depicting a cadaveric specimen mounted in a custom forearm motion simulator. The outrigger stabilizes a third metacarpal pin holding the radiocarpal joint in a neutral position. Optical tracking markers are mounted on delrin posts affixed to the radius and ulna. Pneumatic actuators and the servo motor are attached to a delrin base. Tone loads are being applied to ECU, ECRL, FCU, FCR and PT through the sutures designated as blue. Load to exert an active supination force is being applied through BIC (yellow) and SUP (orange) © Braden Gammon.**

3.3.4   ICD Measurement Technique

At the conclusion of the testing protocol, the forearm was dissected, disarticulated and the bones were denuded of soft tissue. Landmarks on the distal radius, implant, proximal radius and ulna were digitized relative to the attached motion trackers. This permitted the creation of a three-dimensional anatomic coordinate system so the kinematic data could be transformed to describe the position of the radius relative to the ulna.

Once the digitization of these landmarks was complete, four spherical nylon fiducial markers were attached to each bone. Nineteen mm fiducials were attached to non-articular regions of the ulna and proximal radius using #10-24 threaded nylon rods, while 4.76 mm fiducials were used for the distal radius using #2-56 threaded nylon rods (Figure 3.2). Their locations were digitized with respect to that bone's corresponding motion tracker using an appropriately-sized calibrated cupped stylus. The articular surfaces of the distal radius and ulna were also digitized with respect to their corresponding motion trackers using a pointed ball-tipped stylus tool. Articular surface digitizations were 3D point clouds created using a previously described technique[10,26]. The denuded cartilage-bone components were then CT scanned in air[26] to ascertain the specimen's cartilage thickness and allow for the creation of 3-D cartilage models.
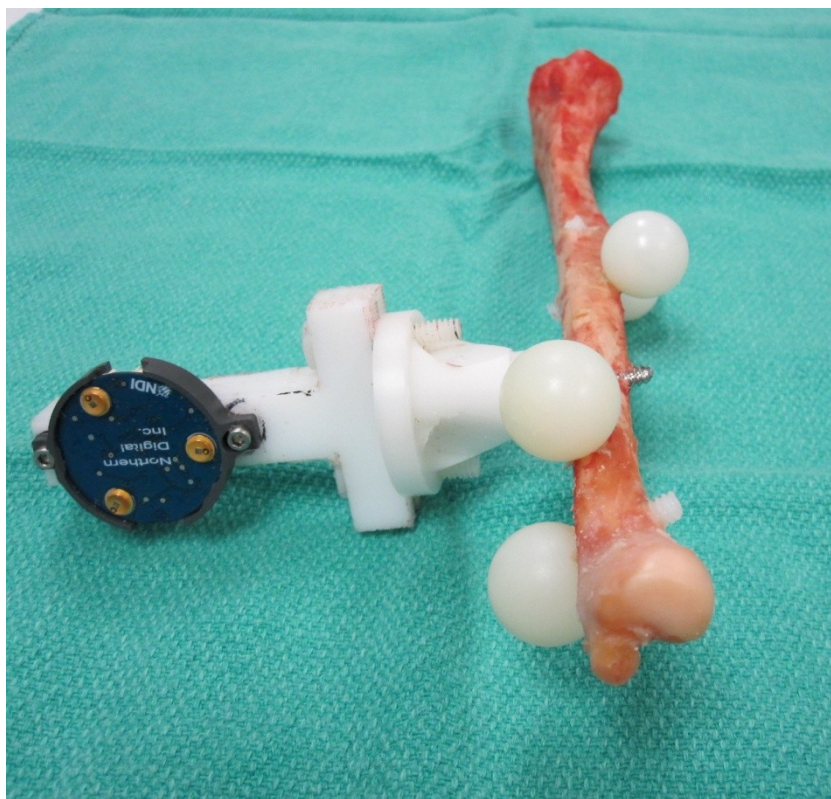
Figure 3.2 **The denuded ulna of a specimen with a delrin-mounted optical tracker and four nylon fiducial spheres. The location of the spheres were digitized relative to the optical tracker. Once digitization was complete, the tracking mount was removed so the bone and fiducials could be CT-scanned © Braden Gammon.**

Volumetric data was obtained of the denuded bone fragments and associated fiducials. CT scanning was performed using a GE Discovery CT750 HD scanner (GE Health care, Pewaukee, WI, USA) at 120 kV and 292 mAs with a slice thickness of 0.625 mm (in-plane pixel size 0.320 mm). The specimen was positioned on a radiolucent jig such that the long axis of the bone fragments and jig were in line with the CT scanner gantry.

CT image data of the denuded bones with fiducials was imported for manipulation into Mimics (version 15.1, Materialise, Leuven, Belgium). Bone and cartilage geometries were determined using minimum threshold-based segmentation (cartilage models = –700 HU, bone models = +250 HU). Models were wrapped, resulting in sealed hollow shell models that were exported in the stereolithography (.STL) format.

The models were repositioned from CT images to anatomic-based coordinate systems using a rigid-body registration algorithm. This registration procedure used the fiducials digitized during the experiment as well as the fiducials imaged using CT after the experimental protocol as homologous points[30].

Using the optical motion tracker data recorded from the radius and ulna, the 3D models were reassembled to their corresponding positions and orientations over the arc of simulated active and passive supination. The Inter-cartilage Distance mathematical algorithm was applied using custom software from the Paraview VTK toolkit (Paraview 4.0.1 Parallel Visualization Application, open source), and regions with cartilage-cartilage overlap between models were deemed to be areas of contact (Figure 3.3).
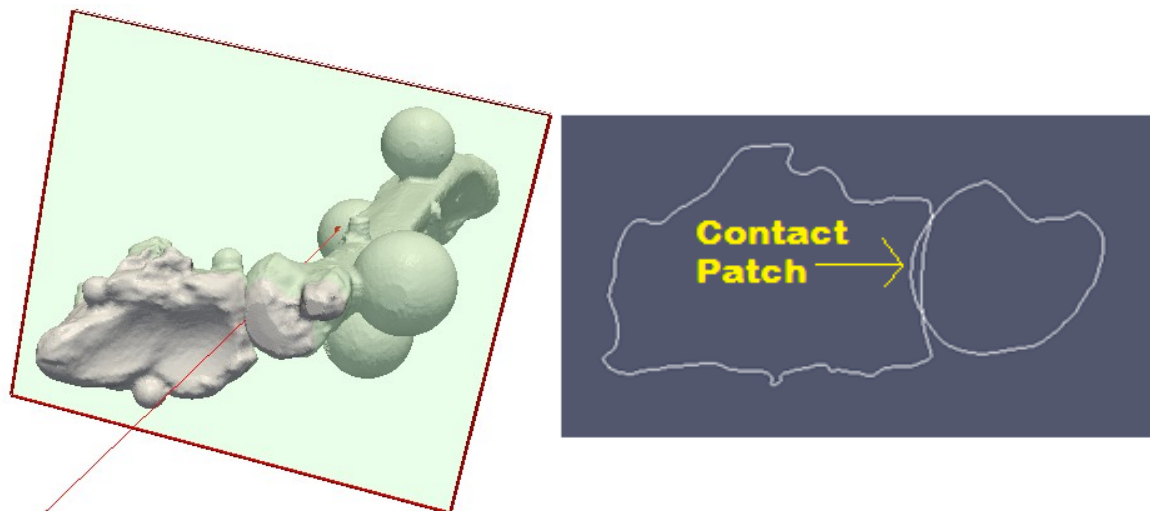
Figure 3.3 **The distal radius and ulna cartilage models with fiducial markers. These have been reassembled using fiducial based-registration to their original position and orientation. Note in cross-section the cartilage-cartilage overlap between models. This area of overlap is designated as the contact patch © Braden Gammon.**

As described in Chapter 1, Section 1.6.2, an anatomical coordinate system was generated for the sigmoid notch of the distal radius using MatLAB (MATLAB 8.0, The MathWorks, Inc., Natick, Massachusetts, United States). An anatomical coordinate system was assigned to the sigmoid notch of the distal radius, with a point designated as its centre. The centroid of the contact patch was then determined, and its movement was described relative to the centre point of the sigmoid notch (Figure 3.4). Contact centroid position relative to the sigmoid notch centre was calculated in mm for both the volar-dorsal and proximal-distal axes.
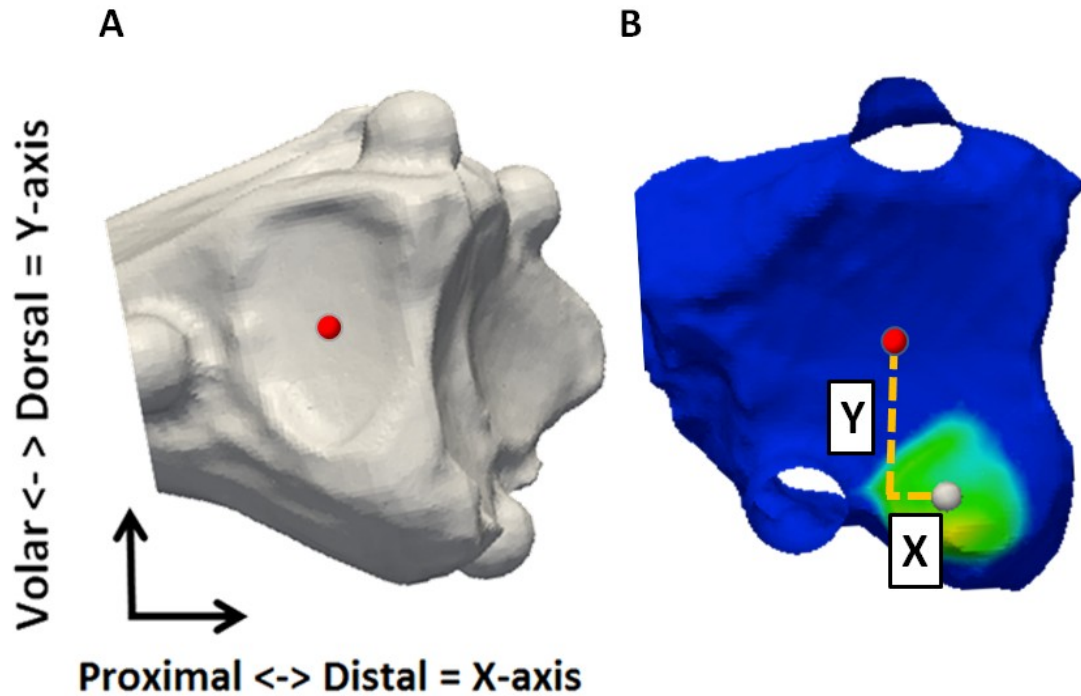
Figure 3.4 Demonstrates the sigmoid notch of the distal radius and its centre point in red (A). Movement of the white contact centroid was described relative to this position (B), with directionality as depicted by anatomical axes shown. "X" and "Y" represents the distance the contact centroid moved along their respective X and Y axes in mm. © Braden Gammon.

3.3.5   Data Analysis

All 8 specimens were used for ICD contact analysis. The optical tracking system was unable to capture the extremes of forearm rotation due to loss of tracker visualization, so an arc from 60° of supination to 60° of pronation was available for analysis. A contact patch and centroid position was measured for each 10° interval of forearm rotation.

The effect of forearm movement method (i.e. simulated active versus passive motion) and the effect of rotation angle on DRUJ contact area were examined. A two-way repeated measures ANOVA was performed, with independent variables of forearm rotation angle and forearm movement method. The data was also analyzed to ascertain whether there was a difference between the magnitudes of contact area in supination compared with pronation across specimens. For matched pairs of forearm rotation angle

(eg. 10° of supination compared with 10° of pronation), a two-way repeated measures ANOVA was performed, with independent variables of forearm rotation angle and forearm position (supination versus pronation). Both simulated active and passive supination were examined.

Centroid coordinate data from 8 specimens was also analyzed. The effect of simulated active versus passive forearm movement on the pathway of the DRUJ contact centroid was analyzed. A two-way repeated measures ANOVA was performed, with independent variables of forearm rotation angle and forearm movement method. To determine if the passive contact pathway was more variable relative to the active pathway, the standard deviation values for each 10° interval of forearm rotation were compared using a paired T-test. Both the x and y axes were evaluated.

Data imputation using a linear regression model was used to reconstitute missing contact area and centroid coordinate values. A Greenhouse-Geisser correction was applied. Statistical significance was set at $p < 0.05$. Data presented is the mean DRUJ contact area ± standard deviation unless otherwise specified. We used a Bonferroni correction for multiple comparisons to compare main effects.

3.4   Results

At each interval of forearm rotation evaluated, DRUJ contact area measurements during simulated active supination were compared with passive supination. Though there appeared to be increased overlap on the contact maps created for simulated active supination (Figure 3.5), there was no significant difference between the absolute size of the contact patches comparing the two forearm rotation methods (p=0.55).
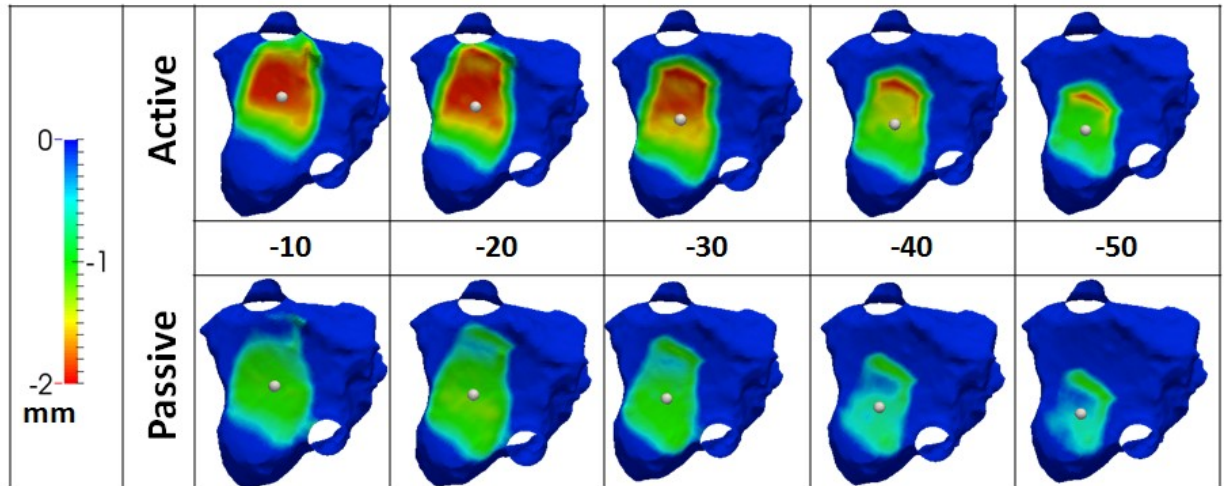
Figure 3.5 The ulnar head is removed and the sigmoid notch is viewed *en face*, with a typical contact map output shown over a short arc of supination. The contact patch is represented by a scalar color map in Paraview (Paraview 3.8.1 Parallel Visualization Application) which delineates the degree of overlap between the cartilage models. A white spherical contact centroid is also shown, and is noted to move from dorsal to volar as the forearm rotates from pronation to supination © Braden Gammon.

There was a statistically significant effect of forearm rotation angle on DRUJ contact area (p=0.002, Figure 3.6). The mean contact area during simulated active supination rose from 65.0 ± 44.6 mm^2 in 60° of supination to its highest at 87.6 ± 52.8 mm^2 in 10° of supination. Beyond this, there was a decline in DRUJ contact area during pronation, with the lowest measurement in 60° of forearm pronation at 2.8 ± 7.6 mm^2. Similar trends were noted for passive supination.
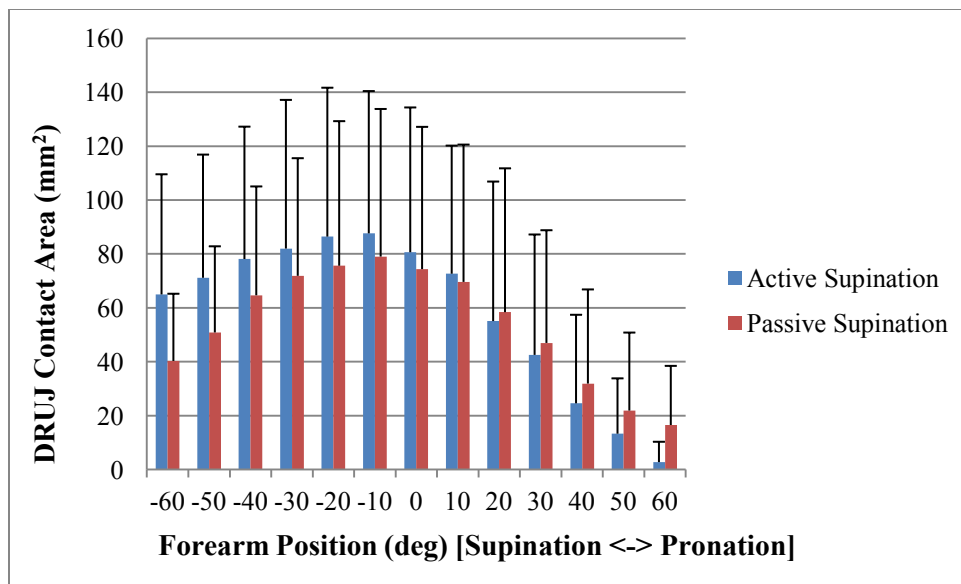
Figure 3.6 **Mean (+ 1 SD) contact area measurement for the distal radioulnar joint across an arc of forearm rotation from -60 of supination to 60° of pronation. Simulated active and passive supination results are displayed © Braden Gammon.**

The contact area for supination was significantly higher compared to pronation ($p<0.005$) during simulated active forearm rotation. The mean contact area in supination was 78.4 ± 46.4 mm^2 versus 35.2 ± 32.0 mm^2 in pronation. There was a mean difference of 43.2 ± 30.5 mm^2 between pronation and supination contact area values for matched forearm rotation angles, with higher differences at more extreme positions. Findings were similar during passive forearm rotation, where again, the contact area values for supination were significantly higher ($p<0.027$). The mean contact area in supination was 63.7 ± 37.1 mm^2 versus 40.9 ± 35.9 mm^2 in pronation during passive motion. There was a mean difference 22.8 ± 23.2 mm^2 between pronation and supination contact area values for matched forearm rotation angles, with higher differences at more extreme positions.

The contact centroid moved 10.5 ± 2.6 mm volar along the volar-dorsal axis during simulated active supination during the arc of forearm rotation examined (60° of supination to 60° of pronation, Figure 3.7). With passive motion the contact centroid moved 8.5 ± 2.6 mm volar (95% CI, 6.6 to10.5 mm volar). Both forearm rotation angle ($p<0.0001$) and method of forearm rotation ($p=0.012$) had a significant effect on the

position of the contact centroid along the volar-dorsal axis. The passive contact centroid pathway was not significantly more variable compared to the active pathway along the volar-dorsal axis (p=0.222).

   Along the proximal-distal axis, the contact centroid moved 5.7±2.4 mm proximal during simulated active supination and 0.2±3.1 mm distal (Figure 3.7) during passive motion. Forearm rotation angle had a significant effect on the position of the contact centroid along the proximal-distal axis (p=0.045).   There was no significant difference between the position of the contact centroid along the proximal-distal axis comparing method of forearm movement (simulated active vs. passive motion) (p=0.136). The passive contact centroid pathway was significantly more variable compared to the active pathway along the proximal-distal axis (p=0.007).
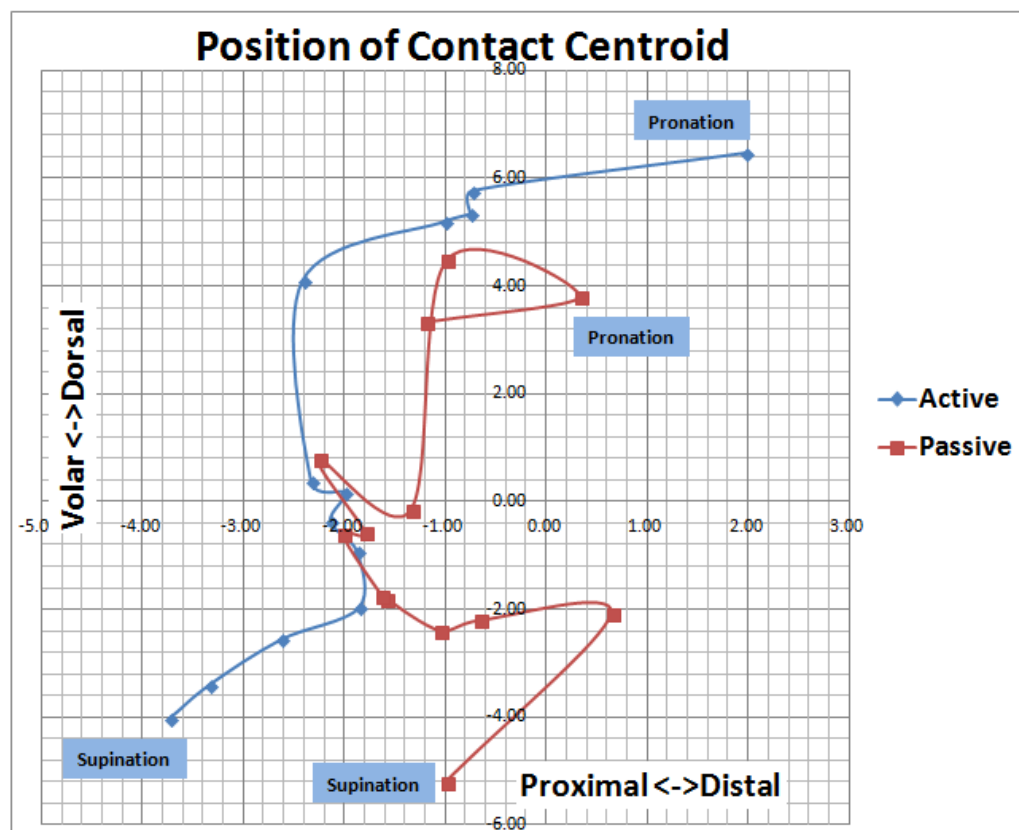
Figure 3.7 The mean position of the contact centroid on the face of the sigmoid notch during forearm rotation. © Braden Gammon.

3.5   Discussion

This study noted a range of values for DRUJ contact area in the intact state, whose magnitude was contingent on the degree of forearm rotation. Contact area in the DRUJ was highest in 10° of supination and lowest in 60° of pronation during both simulated active and passive forearm rotation. Overall, there was more contact in supination than in pronation when comparing analogous forearm rotation angles.

These findings correlate favorably with the current literature. Other authors have noted higher levels of contact area in supination compared with pronation, with the minimum contact in full pronation[13,14,15]. In Shaaban's study, mean maximal contact was 67.5 mm^2 at 30° of supination in their series with a 10 kg axial load applied[15]. Malone et al.[13] noted maximal contact in neutral to 30° of supination, with areas between 50-60 mm^2 at 10 kg of axial load[13]. Our mean maximum contact area of 87.6±52.8 mm^2 in 10° of supination may be slightly larger because it was measured in the intact DRUJ, compared with the other measurements taken using Tekscan with the DRUJ capsule sectioned and the sensor interposed in the articulation.

The angle of forearm rotation also had a significant effect on the centroid position along both the volar-dorsal and proximal-distal axes. This was consistent with previous kinematic studies, which have reported that the radius/sigmoid notch moves dorsally[6] and distally[7,31] relative to the 'static' ulnar head during forearm supination. Movement of the contact centroid should theoretically reflect these kinematic patterns, with contact at the sigmoid notch moving volarly and proximally with progressive supination. As predicted, the centroid location in the current study moved volarly with supination, with magnitudes of 10.5±2.6 mm volar for simulated active motion and 8.5±2.6 mm volar for passive motion. Our contact centroid also moved 5.7±2.4 mm proximal during simulated active motion, which was expected. The pathway followed by our contact centroid during *in vitro* forearm rotation correlated similarly to *in vivo* contact data published by Chen *et al*., which described the sliding motion of the sigmoid notch over the ulnar head through forearm rotation[25]. They noted that the most movement of the contact site occurred from 60° of supination to 30° of pronation. Over a 180° arc of forearm rotation, the contact site at the sigmoid notch moved 2.3 mm proximal and 7 mm volar from full pronation to

full supination. Overall, our magnitudes were slightly higher than those reported by Chen et al., which may relate to differences in measurement technique as well as differences in muscle activation between *in-vivo* motion and *in-vitro* simulated motion.   In our study, the centroid moved 0.2±3.1 mm distal during passive motion, which was unexpected. The unexpected movement of the passive centroid along the proximal-distal axis is likely secondary to the significant variability of its pathway. This same variability was not seen with simulated active movement, and may be a result of the operator manually applying variable forces and moments to rotate the forearm.

We found that there was no significant difference in DRUJ contact area between simulated active and passive forearm rotation. It is difficult to directly compare results with other authors, as other studies examined static loaded positioning instead of dynamic simulated motion. Nevertheless, Shabaan noted a significant change in the DRUJ contact area between loaded and unloaded conditions[15]. There was no difference however, in contact area between 5 kg and 10 kg of load, and the authors suggested that contact area reaches a plateau beyond this threshold. Malone noted a similar effect beyond 2 kg of axial load[13]. In our series of arms, 10 N tone loads were applied to wrist flexors and extensors even during simulated passive forearm rotation. Thus, a steady state in contact area may have already been achieved, which could account for why additional forces applied to rotate the forearm during simulated active motion had no further effect on contact area. Second, we did not simulate the action of pronator quadratus and a lack of force coapting the DRUJ may explain why there was no change in contact area between active and passive motion. Third, we may be underpowered with our sample size to show a difference for this outcome measure.

The position of the contact centroid along the volar-dorsal axis was significantly different between simulated active and passive motion. The higher magnitudes of change in the centroid's position with active motion were expected, as higher forces were likely being applied to rotate the forearm. The position of the contact centroid along the proximal-distal axis was not significantly different between simulated active and passive motion. This may relate to the increased variability in the pathway of the passive

centroid, for the reasons described above as well as the relatively small displacements compared to volar-dorsal axis.

Between specimens, there was a range of sizes for the contact patch area measurement for any given interval of forearm rotation (eg. 5.3 versus 161.3 mm^2 for two different specimens, each at 20° of supination). This was reflected in the broad confidence intervals presented. This range may have been influenced by: gender differences, size of the specimens, or anatomic variability in the shape of the ulnar head/sigmoid notch with congruency differences at the DRUJ.

This study gives new insight into arthrokinematic changes of the intact distal radioulnar joint during forearm motion. It further supports the finding that contact area between ulnar head and sigmoid notch changes according to the angle of forearm rotation. Moreover, the contact centroid on the sigmoid notch moves volarly and proximally with supination. This study also suggests that the DRUJ is most congruently reduced at 10° of supination, where contact area is the highest. Further investigation is required to determine if this is the optimal position to splint the forearm after injury or surgical intervention to optimize proximity of the joint surfaces. This data can also be used as a baseline to study changes in arthrokinematics following osseous or ligamentous injuries to the wrist and forearm.

3.6   References

1. Xing SG, Chen YR, Xie RG, Tang JB. In vivo contact characteristics of distal radioulnar joint with malunited distal radius during wrist motion. *J Hand Surg Am*. 2015;40(11):2243-8

2. Crisco JJ, Moore DC, Marai GE, Laidlaw DH, Akelman E, Weiss AP, Wolfe SW. Effects of distal radius malunion on distal radioulnar joint mechanics - an in vivo study. *J Orthop Res*. 2007;25(4):547-555.

3. Moore DC, Hogan KA, Crisco JJ, Akelman E, DaSilva MF, Weiss AC. Three-dimensional in vivo kinematics of the distal radioulnar joint in malunited distal radius fractures. *J Hand Surg Am*. 2002 Mar;27(2):233-42

4. Murray PM, Adams JE, Lam J, Osterman AL, Wolfe S. Disorders of the distal radioulnar joint. *Instr Course Lect*. 2010;59:295-311.

5. Ekenstam FA, Hagert CG. Anatomical studies on the geometry and stability of the distal radio ulnar joint. *Scand J Plast Reconstr Surg*. 1985;19(1):17-25.

6. King GJ, McMurtry RY, Rubenstein JD, Gertzbein SD. Kinematics of the distal radioulnar joint. *J Hand Surg Am*. 1986 Nov;11(6):798-804.

7. Linscheid RL. Biomechanics of the distal radioulnar joint. *Clin Orthop Relat Res*. 1992;(275):46-55.

8. Liew VS, Cooper IC, Ferreira LM, Johnson JA, King GW. The effect of metallic radial head arthroplasty on radiocapitellar joint contact area. *Clin Biomech*. 2003;18(2):115-8.

9. Stormont TJ, An KN, Morrey BF, Chao EY. Elbow joint contact study: comparison of techniques. *J Biomech*. 1985;18(5):329-36.

10. Lalone EA, Peters TM, King GW, Johnson JA. Accuracy assessment of an imaging technique to examine ulnohumeral joint congruency during elbow flexion. *Comput Aided Surg*. 2012;17(3):142-152.

11. Viegas SF, Tencer AF, Cantrell J, Chang M, Clegg P, Hicks C, O'Meara C, Williamson JB. Load transfer characteristics of the wrist. Part I. The normal joint. *J Hand Surg Am*. 1987;12(6):971-978.

12. Viegas SF, Tencer AF, Cantrell J, Chang M, Clegg P, Hicks C, O'Meara C, Williamson JB. Load transfer characteristics of the wrist. Part II. Perilunate instability. *J Hand Surg Am*. 1987 Nov;12(6):978-85.

13. Malone PS, Cooley J, Morris J, Terenghi G, Lees VC. The biomechanical and functional relationships of the proximal radioulnar joint, distal radioulnar joint, and interosseous ligament. *J Hand Surg Br*. 2015 Jun;40(5):485-93

14. Nishiwaki M, Nakamura T, Nagura T, Toyama Y, Ikegami H. Ulnar-shortening effect on distal radioulnar joint pressure: a biomechanical study. *J Hand Surg Am*. 2008;33(2):198-205.

15. Shaaban H, Giakas G, Bolton M, et al. Contact area inside the distal radioulnar joint: effect of axial loading and position of the forearm. *Clin Biomech.* 2007;22(3):313-318.

16. Goto A, Leng S, Sugamoto K, Cooney WP, Kakar S, Zhao K. In Vivo Pilot Study Evaluating the Thumb Carpometacarpal Joint During Circumduction. *Clin Orthop Relat Res*. 2014;472(4):1106-13.

17. Goto A, Moritomo H, Murase T, Oka K, Sugamoto K, Arimura T, Nakajima Y, Yamazaki T, Sato Y, Tamura S, Yoshikawa H, Ochi T. In vivo elbow biomechanical analysis during flexion: three-dimensional motion analysis using magnetic resonance imaging. *J Shoulder Elbow Surg.* 2004;13(4):441-7.

18. Li G, DeFrate LE, Park SE, Gill TJ, Rubash HE. In Vivo Articular Cartilage Contact Kinematics of the Knee: An Investigation Using Dual-Orthogonal Fluoroscopy and Magnetic Resonance Image-Based Computer Models. *Am J Sports Med*. 2005;33(1):102-7.

19. Goto A, Moritomo H, Murase T, Oka K, Sugamoto K, Arimura T, Masumoto J, Tamura S, Yoshikawa H, Ochi T. In vivo three dimensional wrist motion analysis using

magnetic resonance imaging and volume based registration. *J Orthop Res*. 2005;23(4):750-6.

20. Marai GE, Crisco JJ, Laidlaw DH. A kinematics-based method for generating cartilage maps and deformations in the multi-articulating wrist joint from CT images. *Conf Proc IEEE Eng Med Biol Soc.* 2006;1:2079-82.

21. Pillai RR, Thoomukuntla B, Ateshian GA, Fischer KJ. MRI-based modeling for evaluation of in vivo contact mechanics in the human wrist during active light grasp. *J Biomech.* 2007;40(12):2781-7.

22. Omori S, Moritomo H, Omokawa S, Murase T, Sugamoto K, Yoshikawa H. In vivo 3-dimensional analysis of dorsal intercalated segment instability deformity secondary to scapholunate dissociation: a preliminary report. *J Hand Surg Am.* 2013;38(7):1346-55.

23. Tang JB, Chen YR. Changes contact radiocarpal joint wrist hyperextension. *J Hand Surg Am*. 2012;37(11):2257-62.

24. Chen YR, Tang JB. Changes in contact site of the radiocarpal joint and lengths of the carpal ligaments in forearm rotation: an in vivo study. *J Hand Surg Am*. 2013;38(4):712-20.

25. Chen YR, Tang JB. In vivo gliding and contact characteristics of the sigmoid notch and the ulna in forearm rotation. *J Hand Surg Am*. 2013;38(8):1513-9.

26. Willing R, Lapner M, Lalone EA, King GW, Johnson JA. Development of a computational technique to measure cartilage contact area. *J Biomech*. 2014;47(5):1193-7.

27. Lalone EA, Giles JW, Alolabi B, Peters TM, Johnson JA, King GW. Utility of an image-based technique to detect changes in joint congruency following simulated joint injury and repair: an in vitro study of the elbow. *J Biomech*. 2013;46(4):677-82.

28. Gordon KD, Dunning CE, Johnson JA, King GJ. Influence of the pronator quadratus and supinator muscle load on DRUJ stability. *J Hand Surg Am*. 2003;28(6):943-950.

29. Certus O. Research-Grade Motion Capture. *Manufacturer's Manual*. 2011:1-8.

30. Lalone EA, Peters TM, King GW, Johnson JA. Accuracy assessment of an imaging technique to examine ulnohumeral joint congruency during elbow flexion. *Comput Aided Surg*. 2012;17(3):142-152.

31. Schuind FA, Linscheid RL, An KN, Chao EY. A normal data base of posteroanterior roentgenographic measurements of the wrist. *J Bone Joint Surg Am*. 1992;74(9):1418-29.

4 The effect of dorsal angulation deformities on arthrokinematics of the DRUJ measured using Inter-cartilage Distance

4.1 Introduction

Distal radius fractures are the most common type of upper extremity fracture in the United States[1]. Factors such as osteopenia, comminution, age over 60 and a high degree of initial displacement may predispose these to malunion[2]. Residual dorsal angulation is the most common deformity, and the consequences of this have been the most widely studied. Specifically, residual dorsal angulation can alter forearm mechanics, with effects on both the range/axis of forearm rotation[3,4,5] and torque required for pro-supination[6,7]. Moreover, increased dorsal angulation may cause dorsal intercalated segmental instability (DISI)[8] and change the excursion and moment arms of the wrist muscles[9,10].

The consequences of distal radius malunion on the distal radioulnar joint (DRUJ) have been the subject of further enquiry. Dorsal angulation of the distal radius has a significant effect on the DRUJ, causing incongruity[11], instability[12], and abnormal load transfer across the joint[13]. Persistent disability from malunion has been observed clinically, with symptoms including ulnar-sided wrist pain, deformity, restricted forearm rotation and limitations in grip strength[14,15]. Dysfunction related to these may be exacerbated in the setting of associated TFCC rupture, and DRUJ instability[16]. These symptoms may, in part, relate to the biomechanical effects of distal radius malunion on the DRUJ.

Arthrokinematics, or the specific movement of joint surfaces[17], are not well understood for the DRUJ in the setting of distal radius malunion. Using *in vivo* methods, previous authors have documented a reduction in the contact area between the ulnar head and sigmoid notch with malunion[18,19]. *In vivo* methods use live subjects with multiplanar distal radius deformities of variable severity. *In vitro* techniques use cadaveric specimens and allow for individual deformities to be isolated and different conditions to be simulated, such as TFCC rupture. This permits a categorical analysis of the effects of each parameter on the arthrokinematics of the DRUJ.

As described in Chapter 2, accurate indirect measurement of joint contact can also be achieved using *in vitro* techniques. Inter-cartilage Distance is one such technique, which utilizes CT-based bone and cartilage models, fiducial-based registration and optical tracking motion capture data[20].

The purpose of this *in vitro* study was to utilize Inter-cartilage Distance to examine the effects of dorsal angulation deformity on DRUJ contact patterns throughout simulated active forearm rotation. Our hypothesis was that the contact area would decrease with progressive dorsal angulation, and that the centroid of contact would become more volar and distal in the sigmoid notch with increasing deformity. We also hypothesized that simulated TFCC rupture would decrease contact area at the sigmoid notch and increase the variability of the contact path of the centroid.

4.2   Materials and Methods

4.2.1   Specimen Preparation

The methods proposed in Section 3.3 are similar to those herein but are re-summarized below. Testing was performed on 8 fresh frozen left cadaveric forearm specimens (mean age 60 years; range 29 to 75 years; 6 men and 2 women) with no clinical or CT evidence of osteoarthritis. The specimens were amputated at the mid-humeral level and stored at -20 °C. They were thawed for 18 hours at room temperature (22 °C) and then prepared for mounting. The fingers were disarticulated at the metacarpal-phalangeal joints. The distal tendons of the wrist extensors (extensor carpi radialis longus [ECRL], extensor carpi ulnaris [ECU]), wrist flexors (flexor carpi radialis [FCR], flexor carpi ulnaris [FCU]), pronator teres [PT] and biceps [BIC] were then sutured using #2 Ethibond (Ethibond Excel, Ethicon Inc., Piscataway, NJ, USA).

Sutures were passed through alignment guides that were appropriately placed to reproduce the physiologic line of action of each muscle. ECRL and ECU were routed through a lateral epicondyle sleeve, while PT, FCR and FCU were routed through a medial epicondyle sleeve. The supinator [SUP] was modeled by placing a suture anchor in the radial tuberosity and routing the attached suture through a Delrin® sleeve which traversed the supinator crest to the posterolateral aspect of the ulna.

The humerus was rigidly secured to the simulator using a clamp (Figure 4.1). The elbow was placed in 90° of flexion, and the ulna was transfixed to a static post on the simulator using two 2 mm partially threaded pins. A 3.5 mm partially threaded pin was inserted in the third metacarpal along the long axis of rotation of the forearm. This was centered in a ring affixed to the simulator, permitting pro-supination while preventing extremes of wrist flexion and extension. The sutures of ECRL, ECU, FCR, FCU and SUP were routed through alignment pulleys and attached to individual pneumatic actuators (Airpot Corporation, Norwalk, CT).

4.2.2   Simulation of Motion

A servo motor (SM2315D; Animatic, Santa Clara, CA) was used to simulate active motion, with a resistive counterforce provided by a pneumatic actuator. Active supination was initiated by attaching BIC to the servo motor set to motion control at a constant tendon velocity of 5 mm/sec. As the prime mover for supination, BIC provided 67% of the supination load while SUP was loaded simultaneously at 33% of the BIC load via a pneumatic actuator. PT was loaded at 20 N to provide a counterforce. Supination runs began with the specimen in full forearm pronation, progressing through an arc of motion to full supination. This muscle loading ratio was based on a previous investigation of forearm muscle EMG and cross-sectional area[21]. Constant tone loads of 10 N were applied to the FCU, FCR, ECU and ECRL. Simultaneous pneumatic actuator loads were regulated by proportional pressure controllers (PPC, MAC Valves, Wixon, MI, USA) under computer control using custom programmed software (LabVIEW, National Instruments, Texas, USA).

4.2.3   Motion Tracking and Kinematic Data Acquisition

Infrared marker triads were rigidly affixed to the proximal radius and ulna using custom Delrin® pedestals and the arc of simulated active supination was tracked using an Optotrak Certus (Northern Digital Inc, Waterloo, Ontario, Canada) optical motion capture system with a 3D accuracy of 0.1 mm[22].
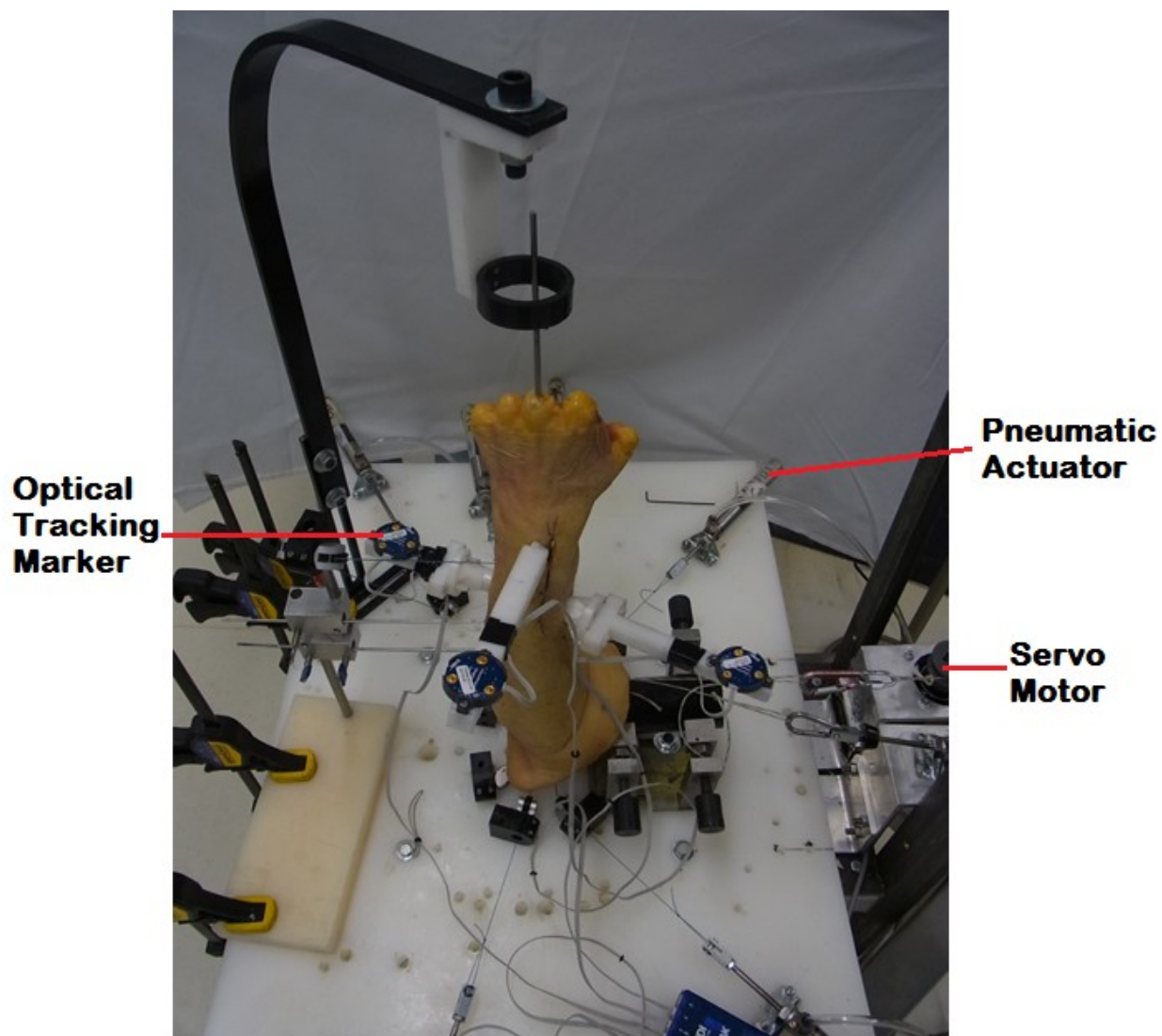
Figure 4.1 Depicting a cadaveric specimen mounted in a custom forearm motion simulator. The outrigger stabilizes a third metacarpal pin holding the radiocarpal joint in a neutral position. Optical tracking markers are mounted on delrin posts affixed to the radius and ulna. Pneumatic actuators and the servo motor are attached to a delrin base © Braden Gammon.

4.2.4   Simulation of Distal Radius Deformity

A previously described, custom-engineered adjustable implant was applied to the volar aspect of the distal radius for each specimen[23]. This permitted the creation of simulated dorsal angulation deformities. The central appliance of the implant was

removable and exchanged for each deformity condition. To install the device, a 20 mm corticocancellous segment of volar distal radius was removed 2 mm proximal to the DRUJ using an oscillating saw. The dorsal cortex was left intact as a bone bridge. Medullary bone from the distal radius metaphysis and shaft was curetted away and cavities were filled with polymethylmethacrylate cement. The adjustable implant was then fixated using bone screws in a neutral position (Figure 4.2).
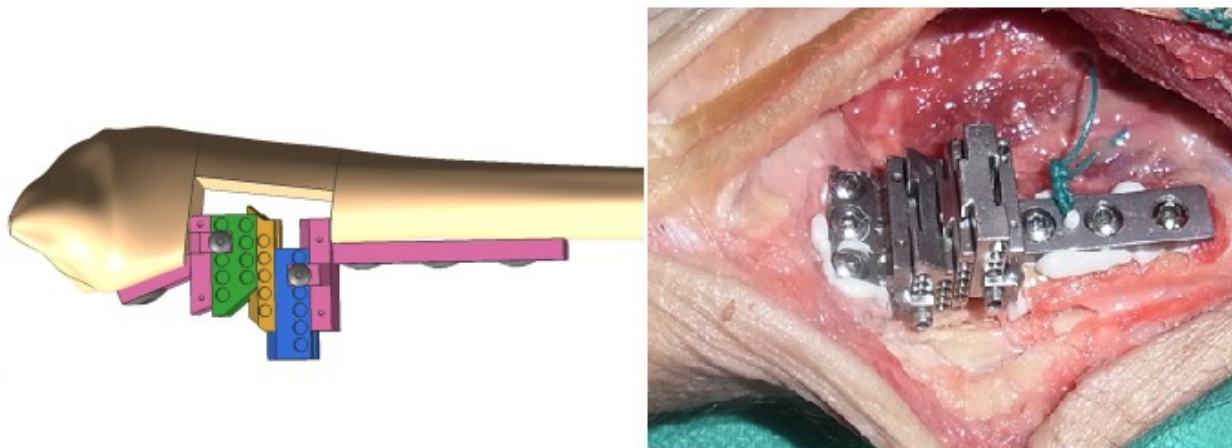
Figure 4.2 The custom adjustable implant is inset into the distal radius osteotomy with a dorsal intact bone bridge. Depicted is a schematic and clinical photo, with the implant's fixation augmented by intramedullary cement © Gillian Fraser and Braden Gammon.

Four (4) different deformity conditions were tested: No deformity (Straight Wedge - SW), dorsal angulation of 10° (DA10), 20° (DA20) and 30° (DA30). The straight wedge configuration of the adjustable implant kept the proximal and distal radius fragments in their original anatomic alignment, while the dorsal angulation configurations introduced progressive dorsal tilt of the articular surface relative to the original anatomy (Figure 4.3).

Straight Wedge

Dorsal Angulation 10⁰

Dorsal Angulation 20⁰

Dorsal Angulation 30⁰
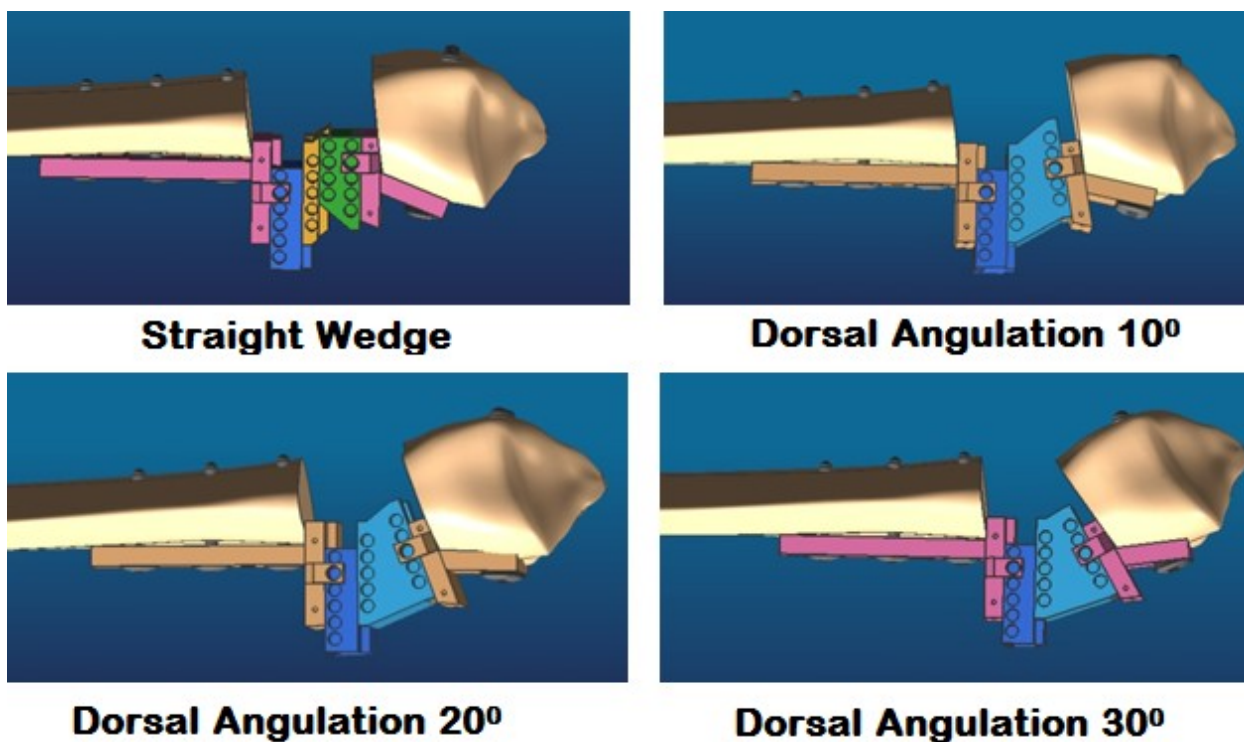
Figure 4.3 Depicting the four different deformity conditions including the straight wedge (SW), dorsal angulation of 10° (DA10), 20° (DA20) and 30° (DA30). Note that the deformities are angulated relative to the original anatomy and do not represent the absolute dorsal angulation value as would be measured on a conventional lateral radiograph © Gillian Fraser and Braden Gammon.

4.2.5   Testing Procedure

The specimens were kept hydrated throughout testing using 0.9% normal saline, and closure of the skin envelope between implant exchanges. Kinematic data was gathered with the implant in the neutral (SW) position, and for the dorsal angulation deformities with the TFCC intact. Once testing of the intact state had concluded, the TFCC was sequentially divided. First, the ECU subsheath and superficial fibers of the radioulnar ligaments were sectioned off their ulnar styloid insertion. Then the deep fibers of the TFCC complex were divided from their attachment on the ulnar fovea (Figure 4.4).
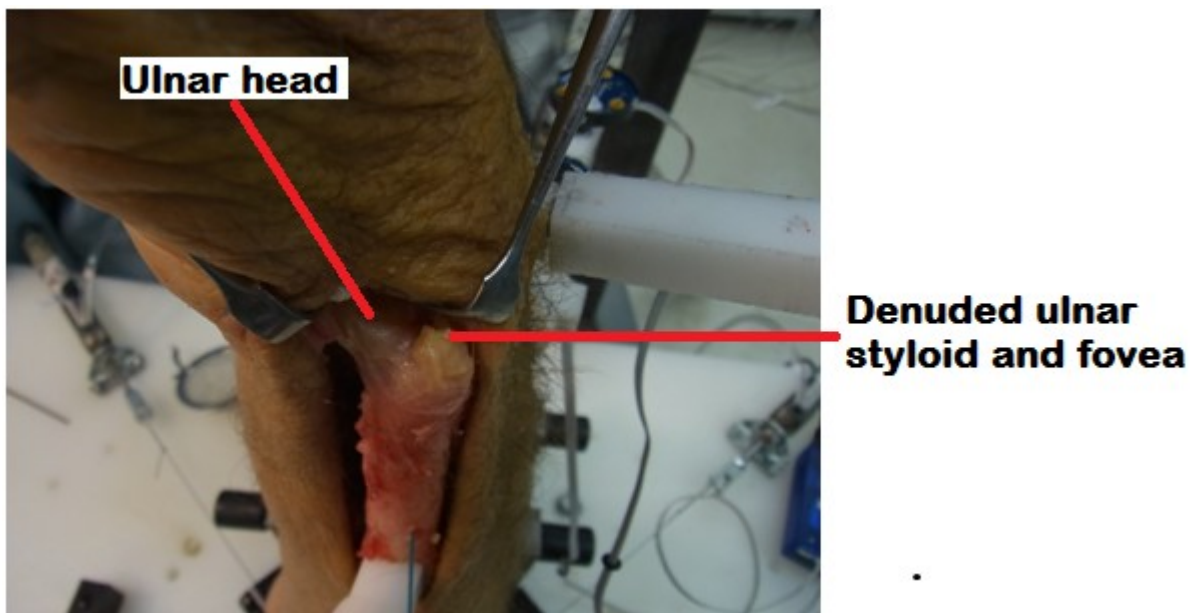
Figure 4.4 **A photo of the sectioned TFCC, with no residual fibers inserting on the ulnar styloid or fovea © Braden Gammon.**

Subsequently, all deformity testing was repeated for the TFCC insufficient state (Figure 4.4). At the conclusion of the testing protocol, the forearm was dissected and the bones were denuded of soft tissue. Landmarks on the distal radius, implant, proximal radius and ulna were digitized relative to the attached motion trackers. This permitted the creation of a three-dimensional anatomic coordinate system so the kinematic data could be transformed to describe the position of the radius relative to the ulna.

4.2.6　ICD Measurement Technique

The detailed protocol for measuring Inter-cartilage Distance is described in Chapter 3, Section 3.3.4. Figure 4.5 provides a flowchart summarizing the stages of data processing which follow kinematic data acquisition from the experimental phase and volumetric data acquisition from the denuded specimens.

Experimental procedure		Kinematic data gathered using optical tracking system during testing protocol
Fiducial markers attached		Nylon spheres implanted on radius (4.76 mm) and ulna (19 mm) ; digitized relative to trackers
Imaging procedure		Bone-cartilage volumetric data collected in air using GE Discovery CT750 HD scanner
Segmentation and bone surface modelling		CT image data manipulated in Mimics Ver. 15.1 to create cartilage models (-700 HU)
Bone model registration		Fiducial based registration used to reposition models based on anatomic coordinate system
Inter-cartilage Distance Algorithm		3-D models examined for areas of cartilage-cartilage overlap; contact area and centroid position analyzed

Figure 4.5 **A flowchart detailing the stages of post-experiment data processing for application of the Inter-cartilage Distance algorithm.**

4.2.7   Data Analysis

All 8 specimens were used for Inter-cartilage Distance contact analysis. The ICD algorithm was used to generate a contact patch and contact centroid for every 10° interval of forearm rotation. The optical tracking system was unable to capture the extremes of forearm rotation due to loss of tracker visualization, so an arc from -60 (60° of supination) to +40 (40° of pronation) was analyzed.

Centroid coordinate data from 8 specimens was also evaluated. An anatomical coordinate system was assigned to the sigmoid notch of the distal radius, with a point designated as its center. Contact centroid position relative to the sigmoid notch center was then calculated in mm, for both the proximal-distal (X) and volar-dorsal (Y) axes.

The effects of forearm rotation angle, distal radius deformity and TFCC sectioning on DRUJ contact area and contact centroid position were evaluated. A 3-way repeated measures ANOVA was performed, with independent variables of forearm rotation angle, distal radius deformity and TFCC condition.

To determine if the centroid pathways were more variable after TFCC sectioning, the standard deviation values for each 10° interval of forearm rotation were compared using a one-way repeated measures ANOVA for matched deformities. Both the proximal-distal and dorsal-volar axes were assessed.

Data imputation using a linear regression model was used to reconstitute missing contact area and centroid coordinate values. A Greenhouse-Geisser correction was applied. Statistical significance was set at p <0.05. Data presented is the mean DRUJ contact area ± standard deviation unless otherwise specified. We used a Bonferroni correction for multiple comparisons to compare main effects.

4.3   Results

There was no significant effect from deformity on contact area in the DRUJ (p=0.30). Forearm rotation angle had a significant effect on contact area (p=0.004), with measurements being highest between 10 to 30° of supination. TFCC sectioning caused a

significant decrease in contact area in the DRUJ (p=0.030), with a mean reduction of 11 ± 7 mm^2 between the TFCC intact and sectioned conditions across all variables (Figures 4.6 and 4.7).
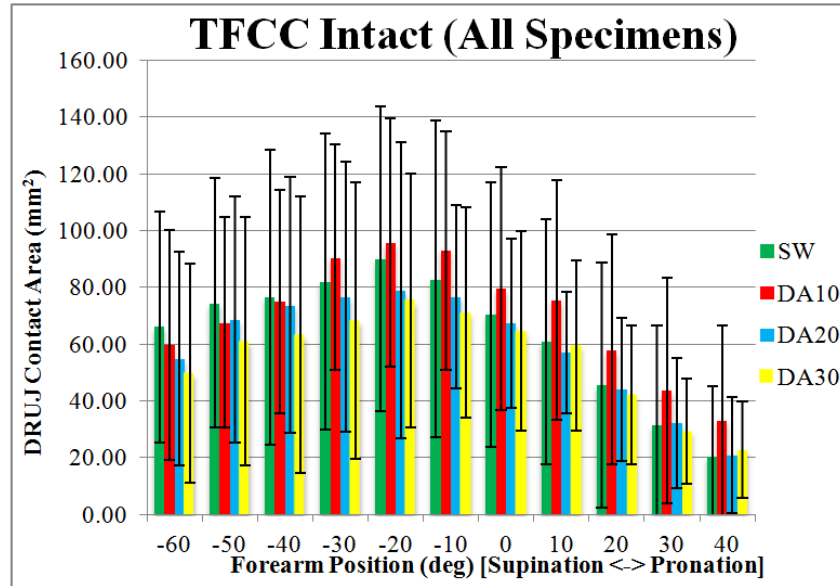
Figure 4.6 **Depicting the mean+1 SD of DRUJ contact area for the normal condition (SW) and with an increasing degree of dorsal angulation deformity (DA10/20/30). Measurements were made at 10° intervals of forearm rotation, from 60° of supination to 40° of pronation © Braden Gammon.**
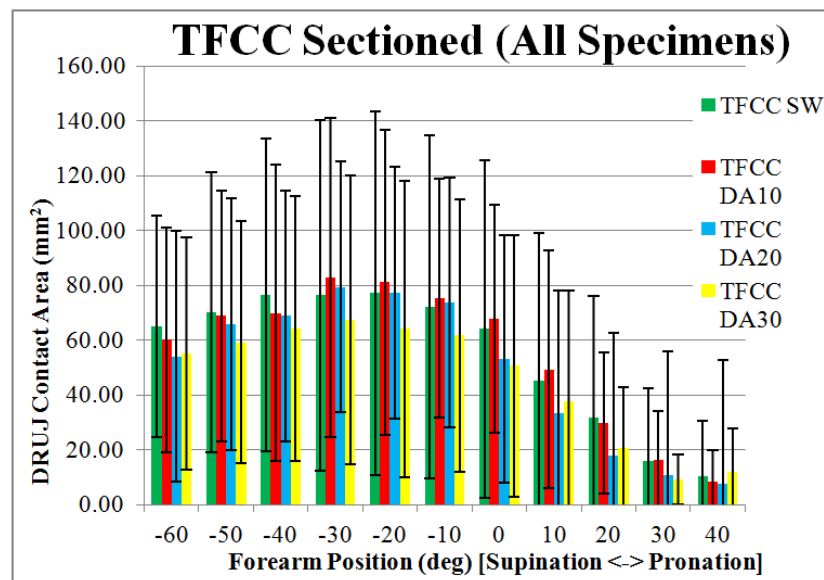
Figure 4.7 **Depicting the mean + 1 SD of DRUJ contact area after TFCC sectioning, for the normal condition (SW) and with an increasing degree of dorsal angulation deformity (DA10/20/30).**

Measurements were made at 10° intervals of forearm rotation, from 60° of supination to 40° of pronation © Braden Gammon.

The position of the contact centroid along the volar-dorsal axis moved volarly with supination for all variables (p<0.001). Deformity had a significant effect on the location of the contact centroid along this plane (p=0.043). Relative to the SW position, the mean centroid position moved 0.3±1 mm volar in 10° of dorsal angulation, 0.1±0.9 mm volar in 20° of dorsal angulation and 0.6±0.9 mm volar in 30° of dorsal angulation. There was no effect from sectioning the TFCC on the volar-dorsal position of the centroid (p=0.24). Variability of the centroid pathway was significantly increased along the volar-dorsal axis after TFCC sectioning (p<0.001), with a 16% increase in the magnitude of standard deviation values for each angle of forearm rotation across deformities.

The position of the contact centroid along the proximal-distal axis moved proximally with supination for all variables (p=0.043). Deformity did not have a significant effect on the location of the contact centroid along this plane (p=0.17). There was no effect from sectioning the TFCC on the proximal-distal position of the centroid (p=0.21). Variability of the centroid pathway was significantly increased along the proximal-distal axis after TFCC sectioning (p=0.004), with a 50% increase in the magnitude of standard deviation values for each angle of forearm rotation across deformities.
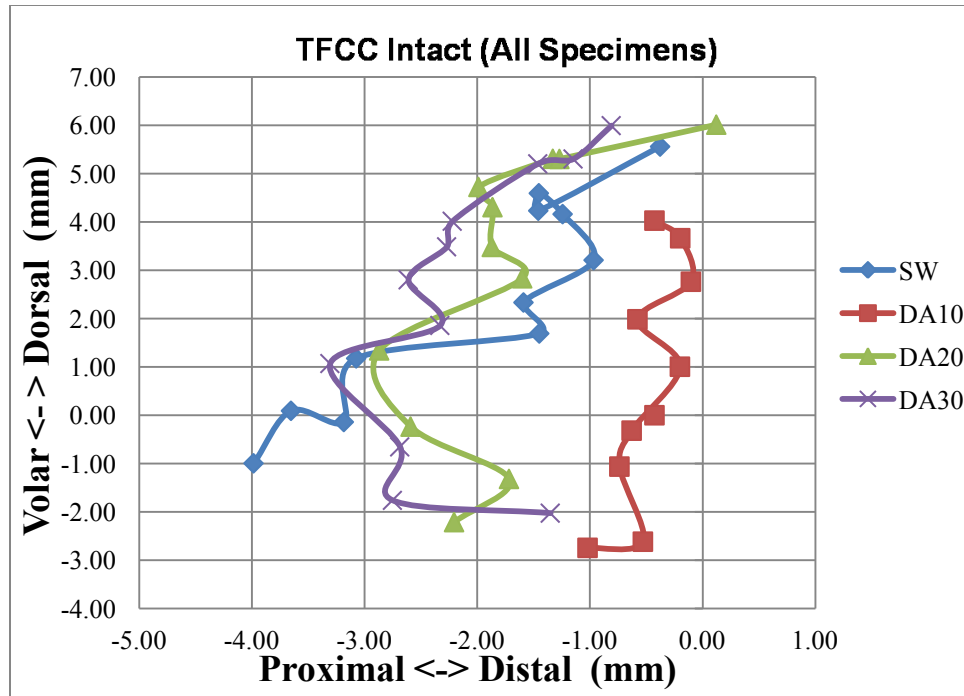
Figure 4.8 The position of the contact centroid on the face of the sigmoid notch during forearm rotation. Mean centroid position is displayed for TFCC intact specimens © Braden Gammon.
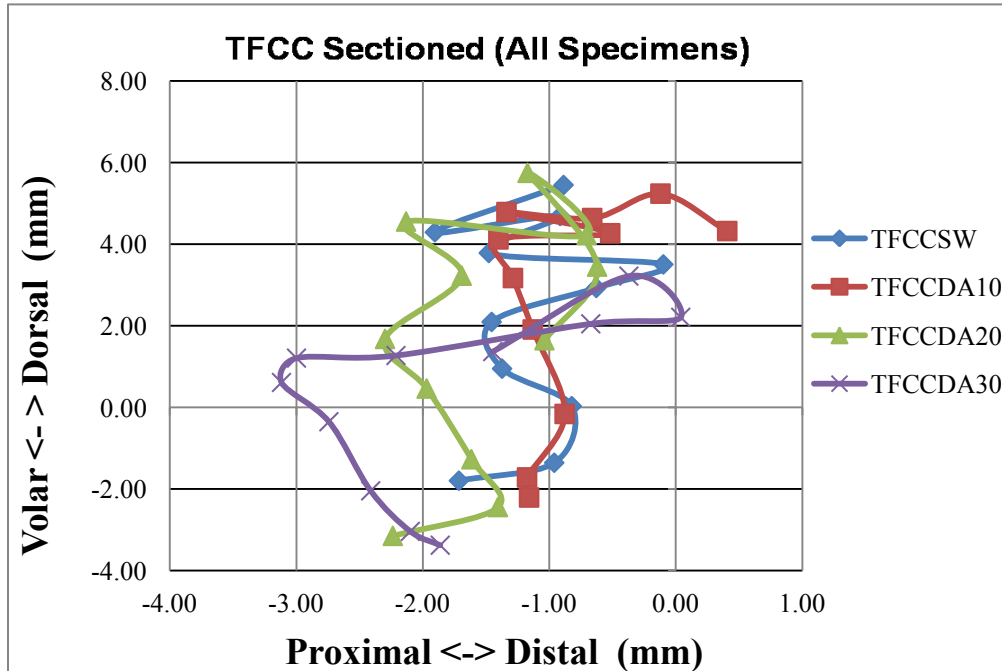
Figure 4.9 The position of the contact centroid on the face of the sigmoid notch during forearm rotation. Mean centroid position is displayed for TFCC sectioned specimens © Braden Gammon.

4.4   Discussion

This study demonstrated that contact area in the DRUJ is variable, and dependent on the angle of forearm rotation. Contact area was maximal between 10 to 30° of supination during the conditions tested. These findings are consistent with the literature, with reports indicating that the highest DRUJ contact area values occur across 10 to 30° of supination[24,25,26]. We noted that the contact centroid on the sigmoid notch moved volarly and proximally with progressive supination. This was also expected, and is in agreement with the published literature on DRUJ kinematics [27,28,29,30] and contact[31].

 Simulated malunion with dorsally angulated distal radius deformities influenced DRUJ contact.   Increasing dorsal angulation caused the contact centroid to move progressively more volar in the sigmoid notch. This was in keeping with our hypothesis, and relates to the distal radius being dorsally displaced relative to the ulnar head during forearm rotation[3,32].   Nishiwaki et al. also noted that the ulnar head moved distal relative to the sigmoid notch with increasing dorsal angulation deformity[32]. Interestingly, we did not find that the contact centroid moved distally with progressive dorsal angulation, with no change being noted along this axis. This may related to the type of deformity tested, and a more significant difference may have been seen with shortening or a combined type of simulated deformity. Alternatively, we may have been underpowered to detect a change along this axis.

We found no correlation between the amount of simulated distal radius deformity and contact area in the distal radioulnar joint. This finding was unexpected, given the sensitivity of this technique for subtle contact area changes[20] and the known effects of dorsal angulation deformity on DRUJ biomechanics[7,12,18,23,34,33,32]. It is possible that DRUJ contact area does not change with progressive dorsal angulation of the distal radius. Alternatively, the lack of difference in our study may relate to the arc of motion studied (60° of pronation to 40° of supination). Other authors have noted the greatest effect of deformity at the extremes of forearm rotation, with limitations in pronation[3] and supination[7] beyond 50° of rotation from increasing dorsal angulation. It is also possible that no difference from deformity was observed because of the type of deformity tested. Previous authors have noted more significant kinematic changes from shortening

compared with dorsal angulation[33] and combined deformities[23]. Using the same adjustable implant as in our study, Fraser et al. noted large deformities were accommodated before loss of forearm motion was evident, and with dorsal angulation deformities only in DA30 was pronation restricted to 65%. This normalized after sectioning of the TFCC. Finally, we may have been underpowered with a small sample size to show a statistically significant difference on contact area between deformity groups.

Our findings are interesting to contrast to *in vivo* studies of the DRUJ in the setting of distal radius malunion[18,34]. Moore and co-workers[34] noted that deformity did not alter kinematics appreciably, with no change in the location or orientation of the axis of forearm rotation, and no change in dorso-volar translation or radius translation along the axis of rotation. They theorized that soft tissue adaptation was responsible and that bony malalignment was constrained by the soft tissues. They postulated that DRUJ load and contact mechanics must be affected in turn. In their follow-up study, Crisco et al.[18] noted that deformity had a significant effect on DRUJ contact area, and that forearm rotation angle had no effect. They demonstrated less contact in malunited wrists (155 vs. 215 mm^2), with ulnar joint space area reduced by 25% in their interbone distance model and a contact centroid which moved more proximally. They found no effect on interbone joint spacing area (their proxy for joint contact area) during changes in forearm range of motion. This was in contrast to our findings, which showed a significant effect of forearm rotation angle on contact area, and did not demonstrate a change in DRUJ contact area with deformity. Moreover, unlike Crisco et al.[18] we noted no change in the position of the contact centroid along the proximal-distal axis with deformity, but did find that it displaced slightly volarly with progressive dorsal angulation. Their values for absolute contact area in normals were also significantly higher than in our study and those documented in the DRUJ by other authors using Tekscan[24,25,26]. There are multiple reasons that could explain the discrepancies: (1) Intercartilage distance is more accurate than interbone distance as the true cartilage thickness is accounted for in the bone-cartilage model, compared with interbone distance where an arbitrary number is used to create the proximity map. (2) Contact was measured off the ulna instead of the radius, as was used in our study. (3) Their technique involved extrapolating kinematics based off

multiple static positions and may have not captured accurate pathways through a range of motion. (4) They were evaluating multiplanar deformities which included shortening, as opposed to isolated dorsal angulation deformities as in our study. (5) Their measurements are based off a live population who have an almost complete active range of motion despite their chronic deformity. *In vitro* specimens are unable to compensate their soft tissue compliance for increasing levels of deformity.

Our study also examined the effect of the TFCC on contact area in the DRUJ. We demonstrated a significant effect of simulated TFCC rupture on contact area in the DRUJ, with a mean contact reduction of 11 ± 7 mm^2 after sectioning. This was to be expected, as once TFCC failure occurs, forces across the DRUJ relax considerably[13]. Multiple studies have corroborated the significant effect of TFCC insufficiency on the DRUJ. It is generally believed that the TFCC complex constrains the DRUJ up to a certain limit in the setting of distal radius deformity. Some authors have experienced that only moderate deformities can be reproduced with an intact TFCC complex. Pogue et al.[35] noted that the distal radius could be oriented to have an inclination of 10°, volar tilt of 0° and shortening of 4 mm without osteotomizing the ulnar styloid. Deformities beyond this required an osteotomy of the ulnar styloid base to release the TFCC which was functioning as a tether. Kihara et al.[3] found that some deformities beyond 10° of dorsal angulation could not be achieved without sectioning of the TFCC. Scheer et al.[36] noted that the distal radius fragment could only be angulated dorsally up to 22° of dorsal angulation. Beyond this, the deformity combined with a shearing and axial load to the wrist resulted in either TFCC failure or fracture at the base of the ulnar styloid. Torques required to achieve full pro-supination significantly decrease with a sectioned TFCC in the setting of dorsal angular malunion[7]. Fraser et al.[23] found that sectioning of the TFCC allowed for more extreme malpositions to be achieved, and no effect of distal radius deformity on forearm pronation was seen after sectioning. In light of the above, it is interesting then that no difference was found from TFCC sectioning on contact centroid position. In our study, after TFCC sectioning there was a 16% increase in the magnitude of standard deviation values for the contact centroid position along the dorsal-volar axis, and a 50% increase along the proximal-distal axis. This implies a dramatic increase in the variability of the

contact centroid pathway after sectioning of the TFCC. This variability likely explains why no significant difference was found.

The limitations of the current study include the inability for cadaveric specimens to undergo soft tissue adaptation, unlike the *in vivo* condition. Moreover, the results are less generalizable because only uniplanar deformity was tested, while malunion is usually comprised of combination of shortening, angulation, translation and rotation. The advantage of an *in vitro* method for studying contact area, compared with *in vivo* methods, are that test parameters are better controlled and effects of individual deformities can be isolated. Fewer assumptions are made for changes in kinematic pathways, as testing occurs continuously throughout an arc of motion. Finally, the cartilage models created from specimens CT scanned in air create excellent cartilage definition and more accurate models.

In conclusion, increasing dorsal angulation deformity has no apparent effect on contact area in the DRUJ, but causes the contact centroid position to displace slightly volarly. Simulated TFCC rupture reduces the DRUJ contact area, and significantly increases the variability of the contact centroid pathway during forearm rotation. Future directions include testing other deformities, including dorsal translation, combined deformities and volar deformities to increase the generalizability of the results.

4.5   References

1. Karl JW, Olson PR, Rosenwasser MP. The epidemiology of upper extremity fractures in the united states. *J Orthop Trauma.* 2015;29(8):242-4.

2. Bhattacharyya R, Morgan BS, Mukherjee P, Royston S. Distal radial fractures: the significance of the number of instability markers in management and outcome. *Iowa Orthop J.* 2014;34:118-22.

3. Kihara H, Palmer AK, Werner FW, Short WH, Fortino MD. The effect of dorsally angulated distal radius fractures on distal radioulnar joint congruency and forearm rotation. *J Hand Surg Am.* 1996;21(1):40-7.

4. Deshmukh SC, Shanahan D, Coulthard D. Distal radioulnar joint incongruity after shortening of the ulna. *J Hand Surg Br.* 2000;25(5):434-8.

5. Ishikawa J, Iwasaki N, Minami A. Influence of distal radioulnar joint subluxation on restricted forearm rotation after distal radius fracture. *J Hand Surg Am.* 2005;30(6):1178-84.

6. Fraser GS, Ferreira LM, Johnson JA, King GJ. The effect of multiplanar distal radius fractures on forearm rotation: in vitro biomechanical study. *J Hand Surg Am.* 2009;34(5):838-848.

7. Hirahara H, Neale PG, Lin Y, Cooney WP, An K. Kinematic and torque-related effects of dorsally angulated distal radius fractures and the distal radial ulnar joint. *J Hand Surg Am.* 2003;28(4):614-621.

8. Kazuki K, Kusunoki M, Yamada J, Yasuda M, Shimazu A. Cineradiographic study of wrist motion after fracture of the distal radius. *J Hand Surg Am.* 1993;18(1):41-6.

9. Tang JB, Ryu J, Omokawa S, Han J, Kish V. Biomechanical evaluation of wrist motor tendons after fractures of the distal radius. *J Hand Surg Am.* 1999;24(1):121-32.

10. LaRoque ES, Murray WM, Langley S, Hariri S, Levine BP, Ladd AL. Muscle moment arms in the first dorsal extensor compartment after radial malunion: a cadaver study. *J Bone Joint Surg Am*. 2008;90(9):1979-87.

11. Kihara H, Short WH, Werner FW, Fortino MD, Palmer AK. The stabilizing mechanism of the distal radioulnar joint during pronation and supination. *J Hand Surg Am*. 1995;20(6):930-6.

12. Saito T, Nakamura T, Nagura T, Nishiwaki M, Sato K, Toyama Y. The effects of dorsally angulated distal radius fractures on distal radioulnar joint stability: a biomechanical study. *J Hand Surg Br*. 2013;38(7):739-745.

13. Ferreira LM, Greeley GS, Johnson JA, King GW. Load transfer at the distal ulna following simulated distal radius fracture malalignment. *J Hand Surg Am*. 2015;40(2):217-23.

14. Prommersberger K, Pillukat T, Mühldorfer M, van Schoonhoven J. Malunion of the distal radius. *Arch Orthop Trauma Surg*. 2012;132(5):693-702.

15. Brogren E, Wagner P, Petranek M, Atroshi I. Distal radius malunion increases risk of persistent disability 2 years after fracture: a prospective cohort study. *Clin Orthop Relat Res*. 2013;471(5):1691-1697.

16. Cheng HS, Hung LK, Ho PC, Wong J. An analysis of causes and treatment outcome of chronic wrist pain after distal radial fractures. *Hand Surg.* 2008;13(1):1-10.

17. Baeyens J, van Glabbeek F, Goossens M, Gielen J, van Roy P, Clarys JP. In vivo 3D arthrokinematics of the proximal and distal radioulnar joints during active pronation and supination. *Clin Biomech*. 2006;21 Suppl 1:S9-12.

18. Crisco JJ, Moore DC, Marai GE, Laidlaw DH, Akelman E, Weiss AP, Wolfe SW. Effects of distal radius malunion on distal radioulnar joint mechanics - an in vivo study. *J Orthop Res*. 2007;25(4):547-555.

19. Xing SG, Chen YR, Xie RG, Tang JB. In vivo contact characteristics of distal radioulnar joint with malunited distal radius during wrist motion. *J Hand Surg Am.* 2015;40(11):2243-8

20. Willing R, Lapner M, Lalone EA, King GW, Johnson JA. Development of a computational technique to measure cartilage contact area. *J Biomech*. 2014;47(5):1193-7.

21. Gordon KD, Dunning CE, Johnson JA, King GJ. Influence of the pronator quadratus and supinator muscle load on DRUJ stability. *J Hand Surg Am*. 2003;28(6):943-950.

22. Certus O. Research-Grade Motion Capture. *Manufacturer's Manual*. 2011:1-8.

23. Fraser GS, Ferreira LM, Johnson JA, King GJ. The effect of multiplanar distal radius fractures on forearm rotation: in vitro biomechanical study. *J Hand Surg Am*. 2009;34(5):838-848.

24. Shaaban H, Giakas G, Bolton M, et al. Contact area inside the distal radioulnar joint: effect of axial loading and position of the forearm. *Clin Biomech.* 2007;22(3):313-318.

25. Nishiwaki M, Nakamura T, Nagura T, Toyama Y, Ikegami H. Ulnar-shortening effect on distal radioulnar joint pressure: a biomechanical study. *J Hand Surg Am*. 2008;33(2):198-205.

26. Malone PS, Cooley J, Morris J, Terenghi G, Lees VC. The biomechanical and functional relationships of the proximal radioulnar joint, distal radioulnar joint, and interosseous ligament. *J Hand Surg Br*. 2015;40(5):485-93

27. Ekenstam FA, Hagert CG. Anatomical studies on the geometry and stability of the distal radio ulnar joint. *Scand J Plast Reconstr Surg.* 1985;19(1):17-25.

28. Schuind F, An KN, Berglund L, Rey R, Cooney WP 3rd, Linscheid RL, Chao EY. The distal radioulnar ligaments: a biomechanical study. *J Hand Surg Am*. 1991;16(6):1106-14.

29. Linscheid RL. Biomechanics of the distal radioulnar joint. *Clin Orthop Relat Res.* 1992;(275):46-55.

30. King GJ, Ogston NG, McMurtry RY, Rubenstein JD. Computerized tomography of the distal radioulnar joint: correlation with ligamentous pathology in a cadaveric model. *J Hand Surg Am*. 1986;11(5):711-717.

31. Chen YR, Tang JB. In vivo gliding and contact characteristics of the sigmoid notch and the ulna in forearm rotation. *J Hand Surg Am*. 2013;38(8):1513-9.

32. Nishiwaki M, Welsh M, Gammon B, Ferreira LM, Johnson JA, King GJ. Distal radioulnar joint kinematics in simulated dorsally angulated distal radius fractures. *J Hand Surg Am*. 2014;39(4):656-663.

33. Adams BD. Effects of radial deformity on distal radioulnar joint mechanics. *J Hand Surg Am*. 1993;18(3):492-8.

34. Moore DC, Hogan KA, Crisco JJ, Akelman E, DaSilva MF, Weiss AC. Three-dimensional in vivo kinematics of the distal radioulnar joint in malunited distal radius fractures. *J Hand Surg Am.* 2002;27(2):233-42.

35. Pogue DJ, Viegas SF, Patterson RM, Peterson PD, Jenkins DK, Sweo TD, Hokanson JA. Effects of distal radius fracture malunion on wrist joint mechanics. *J Hand Surg Am*. 1990;15(5):721-7.

36. Scheer JH, Adolfsson LE. Pathomechanisms of ulnar ligament lesions of the wrist in a cadaveric distal radius fracture model. *Acta Orthop*. 2011;82(3):360-4.

5 SGPS General Discussion, Conclusions and Future Work

5.1 Overview

This chapter reviews the initial objectives and hypotheses presented in Chapter 1, and highlights important conclusions drawn from Chapters 2, 3 and 4. A general discussion and future directions for further enquiry are presented.

5.2 Objectives and Hypotheses

Inter-cartilage Distance is a tool developed to create proximity maps using cartilage models and fiducial-based registration. It has been validated in the elbow, and used successfully to characterize joint contact patterns in an *in vitro* model[9]. It has not previously been used to describe arthrokinematics at the DRUJ. The normal contact patterns between the sigmoid notch and ulnar head during forearm rotation are poorly understood, and less still is known about the secondary effects of distal radius deformity. This thesis fulfilled the following objectives:

1) To utilize the Inter-cartilage Distance algorithm to quantify joint contact at the DRUJ and compare this method to experimental techniques such as casting and Tekscan®.

2) To employ the Inter-cartilage Distance algorithm as a tool to measure normal *in vitro* contact patterns in the DRUJ during simulated forearm motion.

3) To quantify *in vitro* contact patterns in the DRUJ using Inter-cartilage Distance in simulated dorsally-angulated distal radial deformities.

5.3 Comparison of Inter-cartilage Distance as a method for assessing arthrokinematics of the DRUJ

Our hypothesis was that Inter-cartilage Distance would be effective at characterizing joint contact area when compared with other commonly employed techniques; casting and an interpositional scanner (Tekscan). The standard techniques are invasive, therefore their application in this study required the DRUJ capsule to be sectioned. Furthermore, only static positions could be examined. This study showed that ICD values for contact

area were higher than those measured with both Tekscan and casting. Reasons for this were discussed, including possible error in the cartilage models, registration or optical tracking. Conversely, Tekscan and casting may have had artificially lower values for contact area because they were interposed in the joint, likely altering alignment and possibly distorting the articular surface. Furthermore these standard techniques have errors in both sensor sensitivity and cast measurement. Finally this study was limited to a single specimen allowing for only a qualitative comparison between techniques. The ability of ICD to describe contact patterns non-invasively for dynamic *in vitro* models and its reproducibility made it the technique of choice for the subsequent studies in this thesis.

5.4   Arthrokinematics of the DRUJ measured using Inter-cartilage Distance (ICD) in an *in vitro* model

With Inter-cartilage Distance established as a reliable tool for characterizing joint contact patterns, we sought to investigate the arthrokinematics of the DRUJ throughout an arc of simulated forearm supination. Our hypotheses were: 1) the contact area and centroid location would change during forearm rotation; and 2) there would be a difference in the contact patterns between simulated active and passive motion.

In this study, we found the contact area was highest at 10° of supination, and there was more contact in supination compared with pronation. During simulated active forearm supination, the contact centroid moved 10.5±2.6 mm volarly and 5.7±2.4 mm proximally. This change in articular contact was consistent with the known volar and proximal translation of the ulna relative to the sigmoid notch during supination. We did not find that the method of producing forearm rotation (simulated active vs. passive motion) had an effect on DRUJ contact area or centroid position along the proximal-distal axis. The magnitude of displacement for the contact centroid along the volar-dorsal axis was significantly greater during simulated active motion compared with passive motion. This may relate to the muscle forces used to rotate the forearm during active motion. The higher degree of congruency at 10° of supination does have important clinical implications, and suggests that the forearm should be immobilized in this position

during situations where central contact in the DRUJ is important (eg. dorsal or volar rim fracture of the sigmoid notch).

5.5 The effect of dorsal angulation deformities on arthrokinematics of the DRUJ measured using Inter-cartilage Distance (ICD)

Having successfully characterized native DRUJ arthrokinematics using ICD, we sought to investigate the impact of distal radial deformities on contact patterns at this articulation using Inter-cartilage Distance. The effect of dorsally angulated distal radius malunions on the arthrokinematics of the DRUJ were investigated using an *in vitro* forearm model. We hypothesized that increasing dorsal angulation deformity would decrease the DRUJ contact area and displace the contact centroid volarly and distally at the sigmoid notch. We also evaluated the effect of concomitant TFCC rupture and hypothesized that TFCC rupture would further reduce DRUJ contact area and alter the contact centroid position.

This study confirmed that as the dorsal angulation deformity increased, the contact centroid was displaced volarly. The magnitude of movement for the contact centroid was larger than reported DRUJ kinematic values for displacement[10]. This is because traditional kinematics measure displacement between the circle center of the ulnar head and center of the sigmoid notch, while our study looked the surface kinematics of DRUJ. The combined rolling-sliding motion of the sigmoid notch on the ulnar head lengthened the pathway of motion.

No effect of dorsal angulation deformity was seen on DRUJ contact area or the contact centroid position along the proximal-distal axis. This was not unexpected given that dorsal angulation deformities were modelled and as such a change in radial length and therefore proximal-distal contact should have been minimal. Our results may also relate to an underpowered sample size to detect smaller differences, which may not be clinically important.

TFCC sectioning was noted to reduce DRUJ contact area, and significantly increase the variability of the contact centroid pathway, particularly along the proximal-distal axis.

This would be expected given the increase in instability and a reduction of joint compression which occurs after TFCC disruption[11].

This study successfully quantified the effect of dorsally angulated distal radial deformities on contact at the DRUJ. The data suggests that only small changes in DRUJ contact occur with isolated dorsal angulation deformities and may explain why the incidence of DRUJ arthritis is so low in patients with distal radial malunions of this type. This study also demonstrates that complete TFCC ruptures reduce joint contact and therefore splinting or surgical repair should be considered to prevent accelerated cartilage wear.

5.6   General Discussion

The differences between ICD, casting and Tekscan noted in Chapter 2 merit further investigation. We did not note a significant change in ICD values with load, while contact area increased with Tekscan and casting. This implies that there may be cartilage surface deformation that occurs, which is accounted for only by direct assessment.   Wan et al.[12] reported significant deformation of cartilage under load in the tibiotalar joint. At the DRUJ, it is possible that this deformation is occurring, but may not be significant enough to change the proximity of the forearm bones and optical tracking markers. Thus, the predicted contact from our ICD calculation may have remained unchanged under load as a result.

ICD values for contact area were also found to be larger than those for casting and Tekscan. In other studies using ICD and more specimens, there has been closer agreement in contact area values, and subsequent validation of the technique with casting[7,9]. The discrepancy between techniques is likely a result of our study being underpowered, as opposed to ICD routinely over-predicting contact.   This study would benefit from comparing techniques further using a higher number of specimens with variability in their joint morphology and cartilage thickness.

Though ICD may have its limitations, it is questionable whether casting should remain the gold standard for quantification of joint contact area. Direct interpositional

methods of contact assessment, such as casting and Tekscan, may underestimate the true area of contact. The introduction of casting material into the DRUJ involves sectioning the capsule proximally and dorsally, which reduces the forces across the joint even when sutured. Additionally, material interposed in the articulation likely contributes to its distraction and alters the configuration of the articulation. Casting can also be performed in two different ways: 1) with the material interposed into the joint which is subsequently loaded, extruding the cast material vs. 2) by layering cast material around an already loaded joint. It is unknown if the two techniques result in a different contact patch, though the latter could theoretically over-report contact if the cast material fails to infiltrate the border of cartilage-cartilage contact because of its surface tension.

Overall, these studies will be of value to the peer-reviewed literature. They further contribute to our understanding of cartilage contact mechanics in the DRUJ, both under normal conditions and in the setting of distal radial deformity. The use of non-invasive methodology is advantageous, as previous studies have required sectioning of the DRUJ capsule to assess contact, which inherently affects the biomechanics[1,2]. These are the first studies to examine arthrokinematics using a non-invasive *in vitro* model, as most of the literature to date has used *in vivo* methods[3,4,5,6]. The advantage of *in vitro* DRUJ testing is that many sub-types of deformity and be simulated and tested dynamically. This isolates the effect of each distal radius deformity biomechanically. The net effect of that particular deformity can then be fully appreciated, which distinguishes *in vitro* from *in vivo* testing, where live subjects often have complex and confounding multiplanar deformities[4,5,6]. *In vitro* methodology also captures kinematics throughout a range of forearm rotation, and does not incorporate assumptions about motion pathways. This again is in contradistinction to *in vivo* DRUJ methods, which capture only selected angles of forearm rotation and predict the model's contact pathway by extrapolation. Finally, the ICD technique utilizes a model which incorporates regional changes in cartilage thickness[7], unlike *in vivo* methods were the cartilage thickness is estimated[4,5].

In vitro methods for assessing DRUJ contact do have some limitations inherent to their use. Depending on the technique used to monitor forearm kinematics, assessment of the extremes of motion can be limited. The use of optical tracking limited our ability in

this regard due to line of sight challenges with marker dropout. This is of particular significance for assessing DRUJ contact in the setting of deformity, as other authors have noted the effect of deformity most at the extremes of forearm rotation[8]. Additionally, an *in vitro* DRUJ model only gives a representative glimpse of forearm biomechanics at the initial time point after deformity creation. Over time, the stabilizing structures of the DRUJ, including the TFCC, DRUJ capsule and interosseous membrane, will relax and will likely accommodate the deformity to some degree[4,5]. This may, in turn, change the cartilage contact mechanics in a time-dependent fashion. Finally, comparatively large variances were noted with the DRUJ contact mechanics described in Chapters 3 and 4. This phenomenon is another limitation of *in vitro* testing, and may relate to the heterogeneity in study specimens. Size or anatomic variability in the shape of the sigmoid notch/ ulnar head, gender, age and co-morbid TFCC degeneration, will all invariably affect DRUJ arthrokinematics.

5.7   Future Directions

The use of ICD for further investigation of DRUJ arthrokinematics holds great promise. Dorsal angulation deformities are but a small subset of the myriad of deformities which can occur at the distal radius after injury. Further work will include investigating DRUJ contact patterns in simulated dorsal translation, combined angulation/translation, radial shortening and volar deformities. This technique can also be used in other joints to improve our understanding of articular function and response to injury or surgery.

In the future, elements of this technique should be further refined. Higher resolution imaging methods, such as 7 Tesla MRI may allow for the generation of more accurate cartilage models without the need to disarticulate the joint after testing which is required when using CT scanning with air contrast. This will allow for a more accurate and non-invasive *in vivo* application of this technique. More research is required into methods to model and track the movement of soft tissue structures within the wrist. The triangular fibrocartilage complex plays a critical role in the stabilization of the DRUJ and ulnar carpus. Further investigation may reveal how the distal ulna interacts with the

TFCC during forearm rotation, and their arthrokinematics in normal and pathological conditions.

5.8　　References

1. Malone PS, Cooley J, Morris J, Terenghi G, Lees VC. The biomechanical and functional relationships of the proximal radioulnar joint, distal radioulnar joint, and interosseous ligament. *J Hand Surg Br*. 2015;40(5):485-93

2. Shaaban H, Giakas G, Bolton M, et al. Contact area inside the distal radioulnar joint: effect of axial loading and position of the forearm. *Clin Biomech.* 2007;22(3):313-318.

3. Chen YR, Tang JB. In vivo gliding and contact characteristics of the sigmoid notch and the ulna in forearm rotation. *J Hand Surg Am*. 2013;38(8):1513-9.

4. Moore DC, Hogan KA, Crisco JJ, Akelman E, DaSilva MF, Weiss AC. Three-dimensional in vivo kinematics of the distal radioulnar joint in malunited distal radius fractures. *J Hand Surg Am.* 2002;27(2):233-42.

5. Crisco JJ, Moore DC, Marai GE, Laidlaw DH, Akelman E, Weiss AP, Wolfe SW. Effects of distal radius malunion on distal radioulnar joint mechanics - an in vivo study. *J Orthop Res*. 2007;25(4):547-555.

6. Xing SG, Chen YR, Xie RG, Tang JB. In vivo contact characteristics of distal radioulnar joint with malunited distal radius during wrist motion. *J Hand Surg Am.* 2015;40(11):2243-8

7. Lalone EA, Willing RT, Shannon HL, King GW, Johnson JA. Accuracy assessment of 3D bone reconstructions using CT: an intro comparison. *Med Eng Phys*. 2015;37(8):729-38.

8. Fraser GS, Ferreira LM, Johnson JA, King GJ. The effect of multiplanar distal radius fractures on forearm rotation: in vitro biomechanical study. *J Hand Surg Am*. 2009;34(5):838-848.

9. Lalone EA, Peters TM, King GW, Johnson JA. Accuracy assessment of an imaging technique to examine ulnohumeral joint congruency during elbow flexion. *Comput Aided Surg*. 2012;17(3):142-152.

10. Nishiwaki M, Welsh M, Gammon B, Ferreira LM, Johnson JA, King GJ. Distal radioulnar joint kinematics in simulated dorsally angulated distal radius fractures. *J Hand Surg Am*. 2014;39(4):656-663.

11. Ferreira LM, Greeley GS, Johnson JA, King GW. Load transfer at the distal ulna following simulated distal radius fracture malalignment. *J Hand Surg Am*. 2015;40(2):217-23.

12. Wan L, Deasla R, Rubash H, Li G. Determination of in-vivo articular cartilage contact areas of human talocrural joint under weightbearing conditions. *Osteoarthritis Cartilage*. 2006;14(12):1294-1301.

Appendix 1: Glossary of Medical Terms and Abbreviations

Amputate	To remove the portion of a limb surgically
Anterior	Situated at or directed toward the front; opposite of posterior
Arthrokinematics	The specific movement of joint surfaces; the study of joint contact patterns
Articular	Pertaining to a joint
Articular cartilage	A specialized, fibrous connective tissue lining the surface of synovial joints.
Articular disc	A component of the TFCC (triangular fibrocartilage complex); it resembles a smooth disc which bridges the dorsal and volar radioulnar ligaments and is made of fibrocartilage
Articular surface	The end of the bone that forms a synovial joint; see articular cartilage
Articulate	To unite so as to form a joint
Articulation	A joint; the place of union or junction between two or more bones of the skeleton
Biceps (BIC)	A muscle in the upper arm which flexes and supinates the forearm
Cadaveric	Pertaining to a deceased human body preserved for anatomical study
Cancellous bone	Also known as trabecular bone, this type of bone is spongy or lattice-like
Capsular plication	To reduce the redundancy of joint capsule using suture

	material
Denude	To remove all muscle and soft tissue from a bone
Diaphysis	The shaft component of a long bone; comprised of solid, cortical bone
Distal	Farther from the center of the body
Distal radioulnar joint (DRUJ)	One of the two forearm pivot joints, located between the distal radius and ulna
DRUJ capsule	The envelope of tissue which surrounds the DRUJ; contains synovial fluid and imparts stability to the joint
Dorsal	Pertaining to the back; denoting a position toward the posterior surface
Electromyography (EMG)	The recording and study of the electrical properties of skeletal muscle
Epicondyle	A projection upon a bone; above its condyle
Excision	To remove by cutting
Extension	The movement by which the two ends of any jointed part are drawn away from each other; the bringing of a limb into or toward a straight condition
Extensor	Any muscle that extends a joint
Extensor carpi radialis longus (ECRL)	A dorsal forearm muscle that acts as an extensor and radial deviator of the wrist
Extensor carpi ulnaris (ECU)	A dorsal forearm muscle that acts as an extensor and ulnar deviator of the wrist

ECU Subsheath	Tissue which stabilizes the ECU and prevents it from subluxing out of it sheath; the floor forms part of the TFCC and provides further stability to the DRUJ
Fibrocartilage	Tissue with parallel, thick, compact collagenous bundles, separated by narrow clefts containing cartilage cells
Flexion	The movement by which the two ends of any jointed part are drawn towards one another; the bringing of a limb into or toward a bent condition
Flexor	Any muscle that flexes a joint
Flexor carpi radialis (FCR)	A volar forearm muscle that acts as an flexor and radial deviator of the wrist
Flexor carpi ulnaris (FCU)	A volar forearm muscle that acts as an flexor and ulnar deviator of the wrist
Humerus	Long bone of the upper arm
Incongruency	Pertaining to joints: when two cartilage surface geometries do not fit together precisely as their sizes and/or shapes do not match
Inferior	Situated below or directed downward; opposite of superior
Instability	A pathologic condition in which the there is an inability to maintain the normal relationship between the alignment of two joint surfaces
IBD	Inter-bone Distance
ICD	Inter-cartilage Distance
Interosseous Membrane (IOM)	A group of ligaments which joins together and stabilizes two long bones

In-vitro	In an artificial environment
In-vivo	Within the living body
Kinematics	The study of the motion of one body with respect to another, including its position and orientation
Lateral	Denoting a position farther from the median plane or midline of the body or a structure
Malunion	A fracture which has healed in a non-anatomic position; a term generally reserved for bony malposition with associated symptoms such as pain, limitation of motion and/or noticeable deformity
Ligament	A band of fibrous tissue connecting bones, serving to support and strengthen joints
Medial	Situated toward the midline of the body or a structure
Metaphysis	The flare of spongy bone at the end of the diaphysis of a long bone which supports the joint surface
Metacarpal-phalangeal (MP)	The joint between the proximal phalanx and metacarpal in the hand
Metacarpal	A bone in the hand; the thumb and each finger is supported by a metacarpal
Muscle	An organ which by contraction produces movement of a joint
Osteoarthritis	A degenerative joint disease characterized by cartilage degredation and loss; osteophytes and subchondral cysts may also be present
Osteotomy	Refers to bone being surgically cut

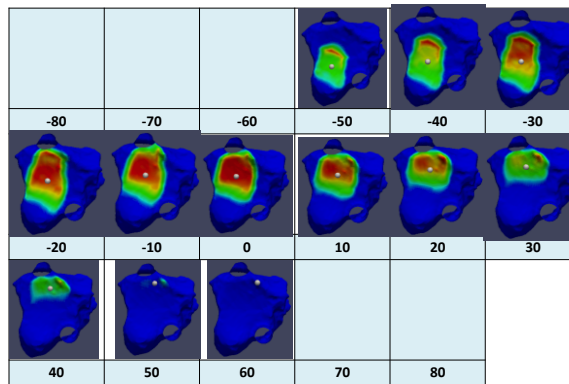|	
Physiological	Normal, not pathologic
Posterior	Directed towards, or situated at the back; opposite of anterior
Pronation	The act of rotating the forearm into a palm downward position
Pronator Quadratus (PQ)	A muscle connecting the radius and ulna in the distal forearm which is responsible for forearm pronation (palm down)
Pronator Teres (PT)	A muscle connecting the radius and ulna in the proximal forearm which is responsible for forearm pronation (palm down)
Proximal	Closer to the center of the body
Proximal radioulnar joint (PRUJ)	One of the two forearm pivot joints, located between the proximal radius and ulna
Radiocarpal joint	The articulation between the distal radius and carpus, including the scaphoid and lunate
Radioulnar	Pertaining to the radius and ulna
Radius	One of the two forearm bones, which is positioned laterally when viewed in the anatomic position. It is curved, and rotates around the ulna.
Range of motion (ROM)	The total arc of motion attained during a specific movement
Sagittal	The anteroposterior plane of the body; pertaining to the longitudinal vertical plane that divides the body into left and right sides
Sigmoid notch	A cartilage bearing concave surface on the distal radius that

	articulates with the distal ulna to make up the DRUJ
Subluxation	Incomplete or partial dislocation of a joint, because of a loss of stability and change in alignment of one or more surfaces
Superior	Situated above, or directed upwards; opposite of inferior
Supination	The act of rotating the forearm into a palm upward position
Supinator	A flat muscle, shaped like a rhomboid, which is found in the forearm and acts to position the forearm in supination
Supinator crest	A bony prominence located on the lateral aspect of the proximal ulna that serves as an insertion site for the lateral ulnar collateral ligament of the elbow
Suture	A stitch or series of stitches used to appose the edges of a surgical or traumatic wound; to apply such stitches
Tendon	A fibrous cord of connective tissue continuous with the fibres of a muscle which attach the muscle to bone or cartilage
Transverse	Extending from side to side; at right angles to the long axis
Triangular fibrocartilage complex (TFCC)	A hammock-shaped structure which supports the ulnar carpal bones during forearm rotation, and links the radius and ulna together at the DRUJ. Its components include: the distal radioulnar ligaments, articular disc, meniscus homologue and ECU subsheath.
Tuberosity	A projection usually found at the end of the bone for the attachment of the muscle or tendon; an elevation or protuberance
Ulna	One of the two forearm bones, which is positioned medially when viewed in the anatomic position. It is relatively straight, and does not move significantly with forearm

	rotation.
Ulnar dome	A cartilage bearing convex surface on the distal ulna that contacts the undersurface of the articular disc of the TFCC
Ulnar styloid	A bony prominence found at the most distal and medial aspect of the ulna, attachment point for the superficial radioulnar ligament fibers
Ulnar fovea	The insertion point on the distal ulna for the deep radioulnar ligament fibers
Ulnar seat	A cartilage bearing convex surface on the distal ulna that articulates with the sigmoid notch to make up the DRUJ
Ulnocarpal ligaments	Include the ulnolunate, ulnotriquetral and ulnocapitate ligaments, which attach to the volar radioulnar ligament and stabilize the ulnar carpus
Ulnocarpal joint	The articulation between the distal ulna and carpus, including the lunate and triquetrum
Valgus	Denoting a deformity in which the angulation is away from the mid-line of the body
Varus	Denoting a deformity in which the angulation of the part is toward the midline of the body
Volar	Pertaining to the sole or palm; indicating the flexor surface of the forearm, wrist, or hand

Appendix 2: Contact Maps for Specimens 1-8

Appendix 2 contains color contact maps for each of the 8 specimens used for Chapters 3 and 4. The specimens are depicted in sequence and each set includes the intact state and simulated deformities. Each plate displays the 10° intervals of forearm rotation that were captured and analyzed. The region in color demonstrates the size of the contact patch, and a white centroid is also shown at the geographic center of contact.

Appendix 2. 1 10-07029L Intact Active Supination © Braden Gammon

Appendix 2. 2 10-07029L Intact Passive Supination © Braden Gammon

10-07029L SW1 Active Supination

-80	-70	-60	-50	-40	-30
-20	-10	0	10	20	30
40	50	60	70	80	

Appendix 2. 3 10-07029L SW1 Active Supination © Braden Gammon

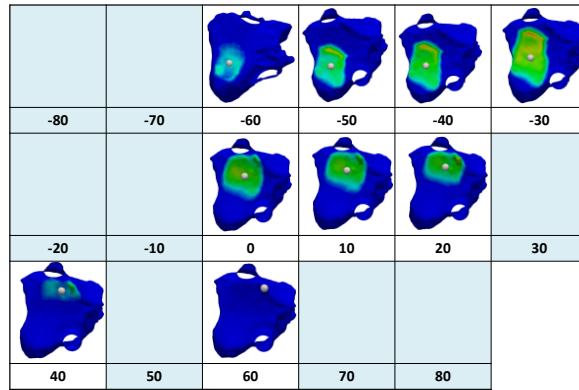**10-07029L** Dorsal Angulation 10 Degrees Active Supination

-80	-70	-60	-50	-40	-30
-20	-10	0	10	20	30
40	50	60	70	80	
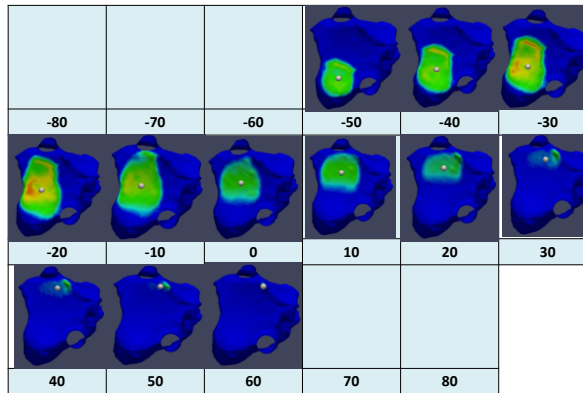
Appendix 2. 4 10-07029L Dorsal Angulation 10° Active Supination © Braden Gammon

10-07029L Dorsal Angulation 20 Degrees Active Supination

-80	-70	-60	-50	-40	-30
-20	-10	0	10	20	30
40	50	60	70	80	
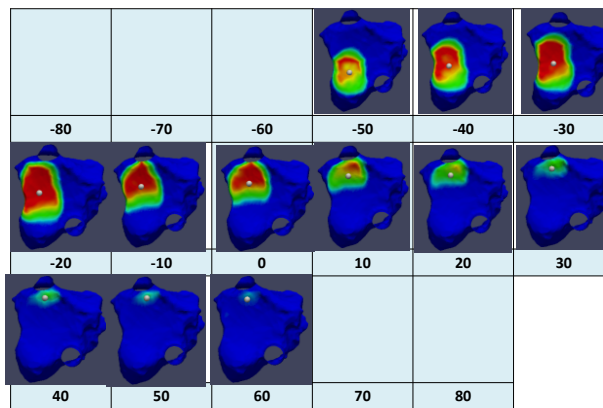
Appendix 2. 5 10-07029L Dorsal Angulation 20° Active Supination © Braden Gammon

10-07029L Dorsal Angulation 30 Degrees Active Supination

-80	-70	-60	-50	-40	-30
-20	-10	0	10	20	30
40	50	60	70	80	

Appendix 2. 6 10-07029L Dorsal Angulation 30° Active Supination © Braden Gammon

10-07029L TFCC Dorsal Angulation 10 Degrees Active Supination

-80	-70	-60	-50	-40	-30
-20	-10	0	10	20	30
40	50	60	70	80	

Appendix 2. 7 10-07029L TFCC Dorsal Angulation 10° Active Supination © Braden Gammon

10-07029L TFCC Dorsal Angulation 20 Degrees Active Supinated

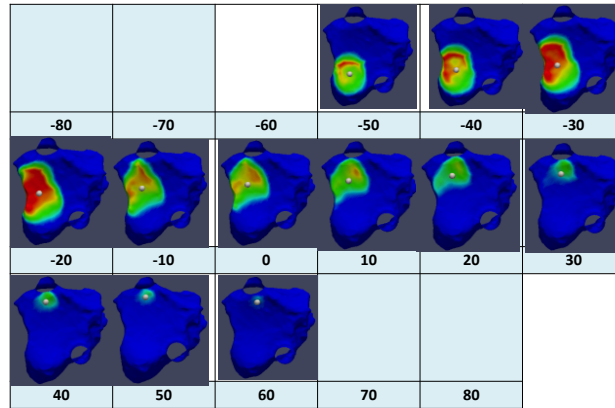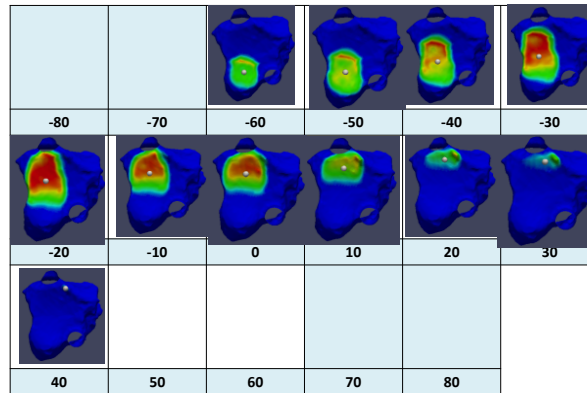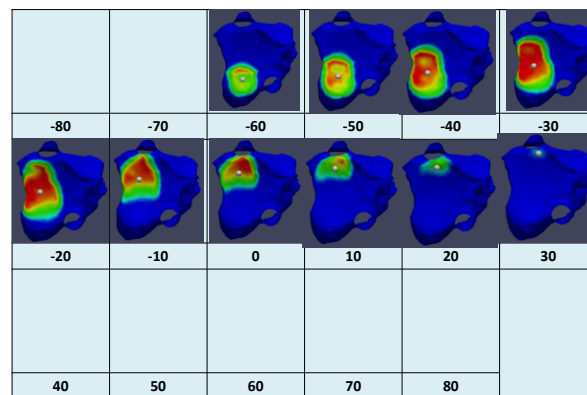| -80	-70	-60	-50	-40	-30
-20	-10	0	10	20	30
40	50	60	70	80	

Appendix 2. 8 10-07029L TFCC Dorsal Angulation 20° Active Supination © Braden Gammon

10-07029L TFCC Dorsal Angulation 30 Degrees Active Supinated

-80	-70	-60	-50	-40	-30
-20	-10	0	10	20	30
40	50	60	70	80	
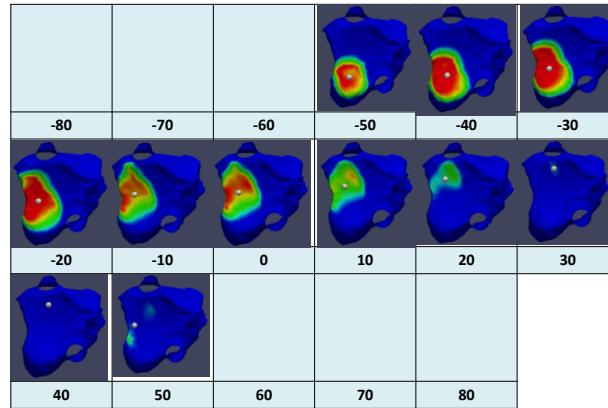
Appendix 2. 9 **10-07029L TFCC Dorsal Angulation 30° Active Supination © Braden Gammon**

11-03057L Intact Active Supination

-80	-70	-60	-50	-40	-30
-20	-10	0	10	20	30
40	50	60	70	80	
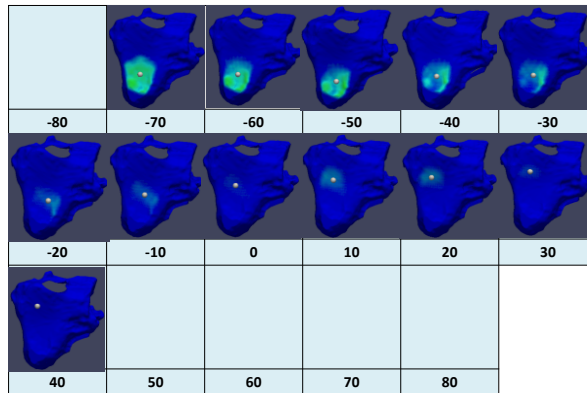
Appendix 2. 10 **11-03057L Intact Active Supination © Braden Gammon**

11-03057L Intact Passive Supination

-80	-70	-60	-50	-40	-30
-20	-10	0	10	20	30
40	50	60	70	80	

Appendix 2. 11 **11-03057L Intact Passive Supination © Braden Gammon**

11-03057L SW1_Active

-80	-70	-60	-50	-40	-30
-20	-10	0	10	20	30
40	50	60	70	80	
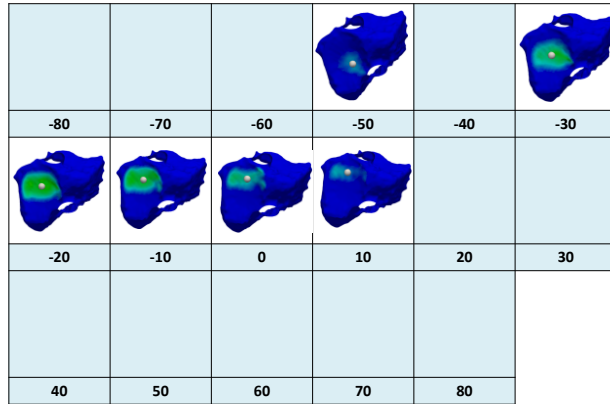
Appendix 2. 12 **11-03057L SW1 Active Supination © Braden Gammon**

11-03057L Dorsal Angulation 10 Degrees Active Supination

-80	-70	-60	-50	-40	-30
-20	-10	0	10	20	30
40	50	60	70	80	
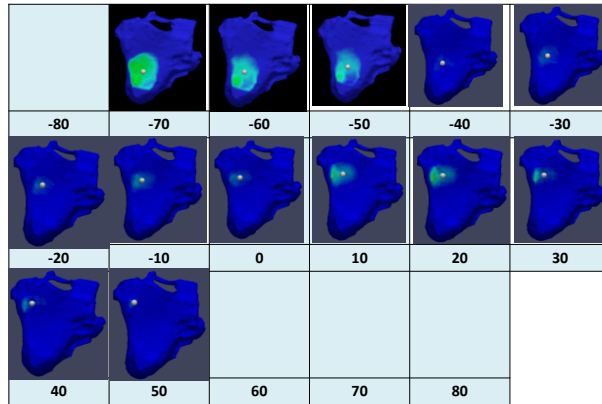
Appendix 2. 13 **11-03057L Dorsal Angulation 10° Active Supination © Braden Gammon**

11-03057L Dorsal Angulation 20 Degrees Active Supination

-80	-70	-60	-50	-40	-30
-20	-10	0	10	20	30
40	50	60	70	80	
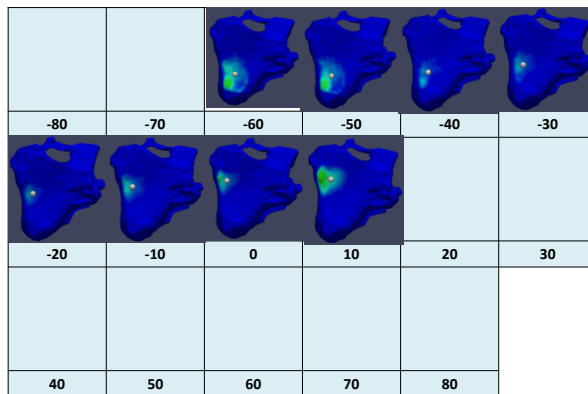
Appendix 2. 14 11-03057L Dorsal Angulation 20° Active Supination © Braden Gammon

11-03057L Dorsal Angulation 30 Degrees Active Supination

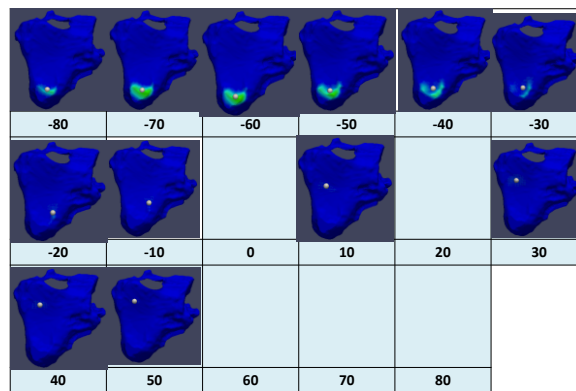| -80 | -70 | -60 | -50 | -40 | -30 |
| -20 | -10 | 0 | 10 | 20 | 30 |
| 40 | 50 | 60 | 70 | 80 | |
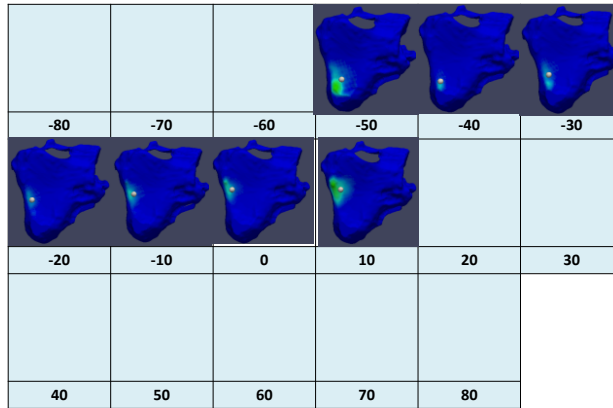
Appendix 2. 15 11-03057L Dorsal Angulation 30° Active Supination © Braden Gammon

11-03057L TFCC SW1 Active Supination

-80	-70	-60	-50	-40	-30
-20	-10	0	10	20	30
40	50	60	70	80	

Appendix 2. 16 11-03057L TFCC SW1 Active Supination © Braden Gammon

11-03057L TFCC Dorsal Angulation 10 Degrees Active Supination

-80	-70	-60	-50	-40	-30
-20	-10	0	10	20	30
40	50	60	70	80	

Appendix 2. 17 11-03057L TFCC Dorsal Angulation 10° Active Supination © Braden Gammon

11-03057L TFCC Dorsal Angulation 20 Degrees Active Supination
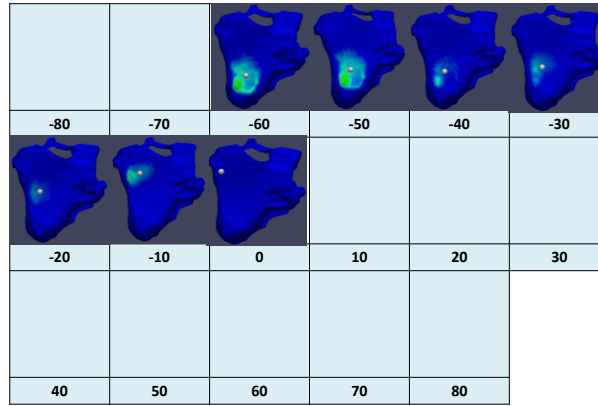
Appendix 2. 18 **11-03057L TFCC Dorsal Angulation 20° Active Supination © Braden Gammon**

11-03057L TFCC Dorsal Angulation 30 Degrees Active Supination

Appendix 2. 19 **11-03057L TFCC Dorsal Angulation 30° Active Supination © Braden Gammon**

125

11-10052L Intact Active Supination

Appendix 2. 20 11-10052L Intact Active Supination © Braden Gammon
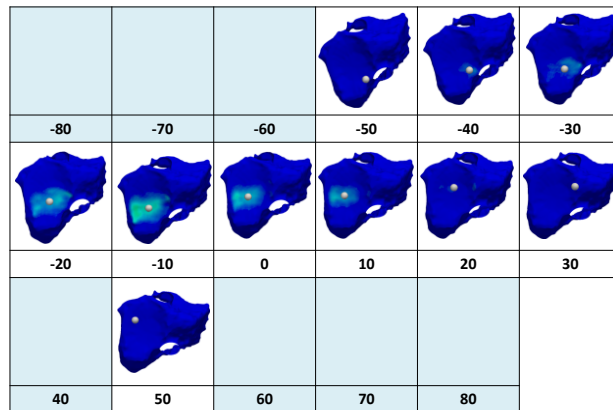
11-10052L Intact Passive Supination

Appendix 2. 21 11-10052L Intact Passive Supination © Braden Gammon

11-10052L SW1_active_supination

-80	-70	-60	-50	-40	-30
-20	-10	0	10	20	30
40	50	60	70	80	
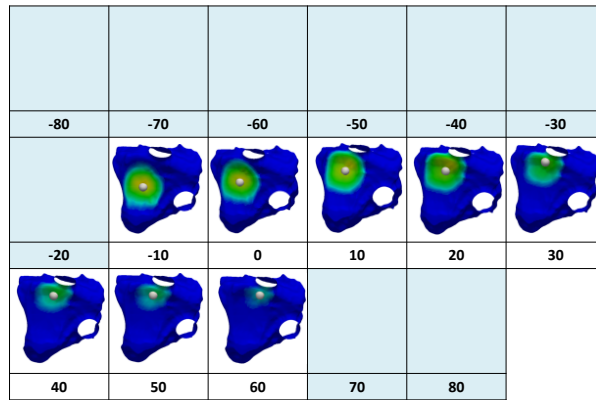
Appendix 2. 22 11-10052L SW1 Active Supination © Braden Gammon

11-10052L Dorsal Angulation 10 Degrees Active Supination

-80	-70	-60	-50	-40	-30
-20	-10	0	10	20	30
40	50	60	70	80	
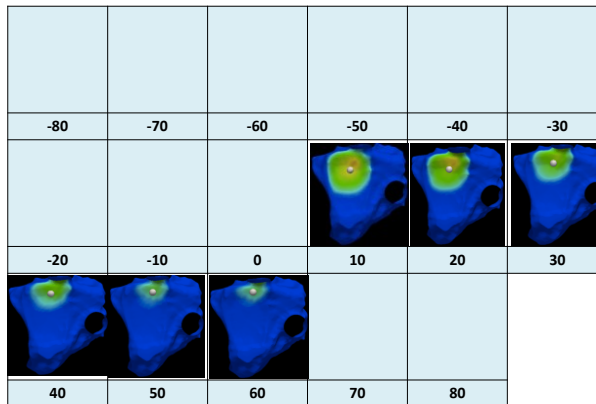
Appendix 2. 23 11-10052L Dorsal Angulation 10° Active Supination © Braden Gammon

11-10052L Dorsal Angulation 20 Degrees Active Supination

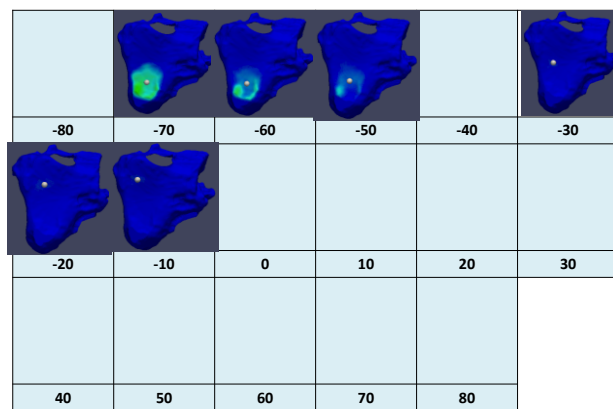| -80	-70	-60	-50	-40	-30
-20	-10	0	10	20	30
40	50	60	70	80	
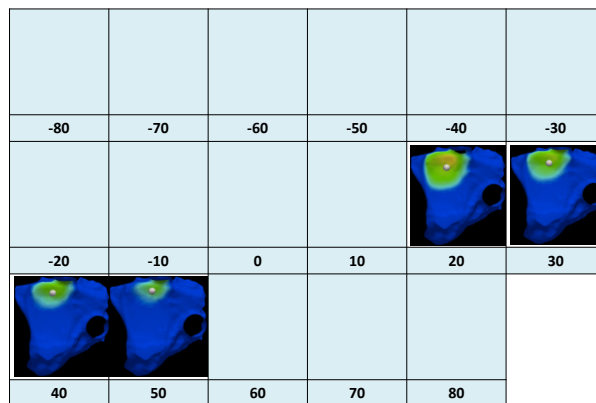
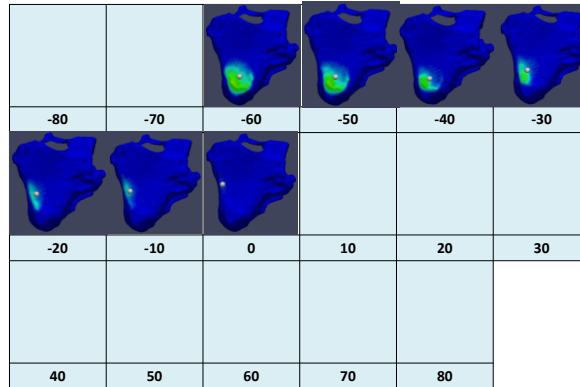**Appendix 2. 24 11-10052L** Dorsal Angulation 20° Active Supination © Braden Gammon

11-10052L Dorsal Angulation 30 Degrees Active Supination

-80	-70	-60	-50	-40	-30
-20	-10	0	10	20	30
40	50	60	70	80	

Appendix 2. 25 11-10052L Dorsal Angulation 30° Active Supination © Braden Gammon

11-10052L TFCC Dorsal Angulation 10 Degrees Active Supination

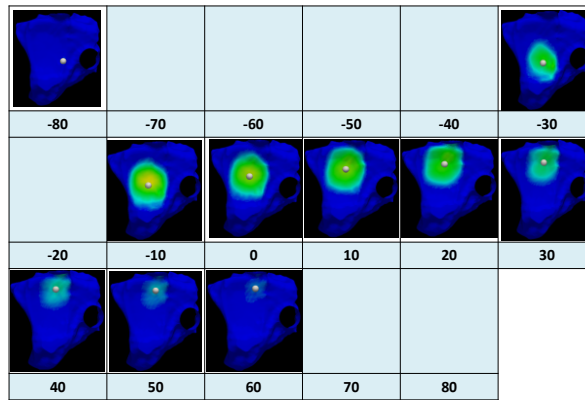| -80	-70	-60	-50	-40	-30
-20	-10	0	10	20	30
40	50	60	70	80	

Appendix 2. 26 11-10052L TFCC Dorsal Angulation 10° Active Supination © Braden Gammon

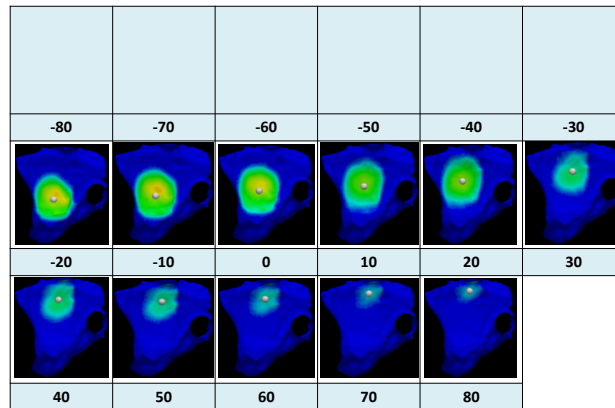11-10052L TFCC Dorsal Angulation 20 Degrees Active Supination

-80	-70	-60	-50	-40	-30
-20	-10	0	10	20	30
40	50	60	70	80	

Appendix 2. 27 11-10052L TFCC Dorsal Angulation 20° Active Supination © Braden Gammon

11-10052L TFCC Dorsal Angulation 30 Degrees Active Supination

-80	-70	-60	-50	-40	-30
-20	-10	0	10	20	30
40	50	60	70	80	

Appendix 2. 28 11-10052L TFCC Dorsal Angulation 30° Active Supination © Braden Gammon

11-12061L Intact Active Supination

-80	-70	-60	-50	-40	-30
-20	-10	0	10	20	30
40	50	60	70	80	

Appendix 2. 29 11-12061L Intact Active Supination © Braden Gammon

11-12061L Intact Passive Supination

-80	-70	-60	-50	-40	-30
-20	-10	0	10	20	30
40	50	60	70	80	

Appendix 2. 30 11-12061L Intact Passive Supination © Braden Gammon

11-12061L sw1_active

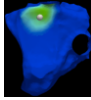| -80 | -70 | -60 | -50 | -40 | -30 |
| -20 | -10 | 0 | 10 | 20 | 30 |
| 40 | 50 | 60 | 70 | 80 | |
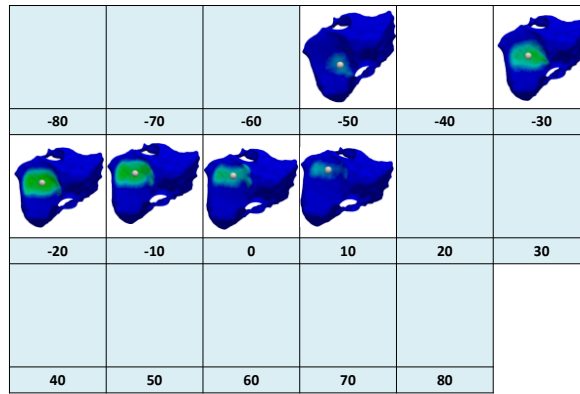
Appendix 2. 31 11-12061L SW1 Active Supination © Braden Gammon

11-12061L Dorsal Angulation 10 Degrees Active Supination

| -80 | -70 | -60 | -50 | -40 | -30 |
| -20 | -10 | 0 | 10 | 20 | 30 |
| 40 | 50 | 60 | 70 | 80 | |
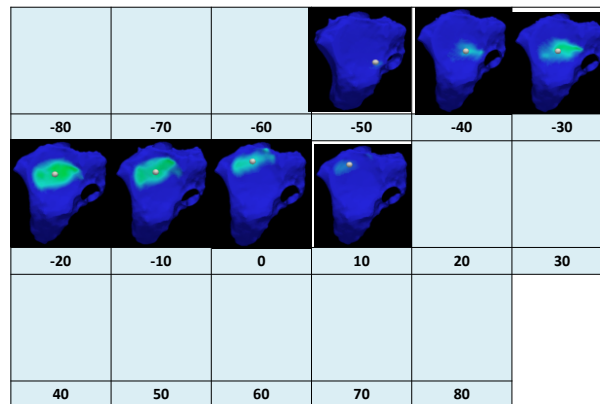
Appendix 2. 32 11-12061L Dorsal Angulation 10° Active Supination © Braden Gammon

11-12061L Dorsal Angulation 20 Degrees Active Supination

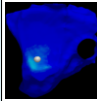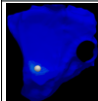| -80 | -70 | -60 | -50 | -40 | -30 |
| -20 | -10 | 0 | 10 | 20 | 30 |
| 40 | 50 | 60 | 70 | 80 | |
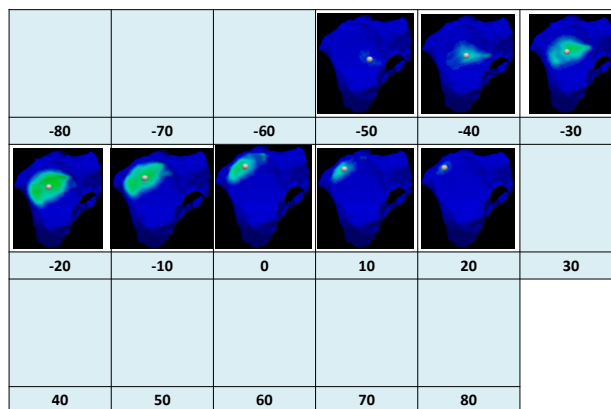
Appendix 2. 33 11-12061L Dorsal Angulation 20° Active Supination © Braden Gammon

11-12061L Dorsal Angulation 30 Degrees Active Supination

-80	-70	-60	-50	-40	-30
-20	-10	0	10	20	30
40	50	60	70	80	

Appendix 2. 34 11-12061L Dorsal Angulation 30° Active Supination © Braden Gammon

11-12061L TFCC SW1 Active Supination

-80	-70	-60	-50	-40	-30
-20	-10	0	10	20	30
40	50	60	70	80	

Appendix 2. 35 11-12061L TFCC SW1 Active Supination © Braden Gammon

11-12061L TFCC Dorsal Angulation 10 Degrees Active Supination

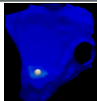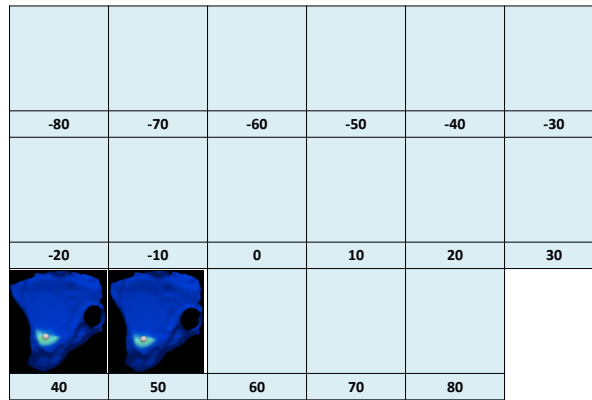| -80	-70	-60	-50	-40	-30
-20	-10	0	10	20	30
40	50	60	70	80	

Appendix 2. 36 11-12061L TFCC Dorsal Angulation 10° Active Supination © Braden Gammon

11-12061L TFCC Dorsal Angulation 20 Degrees Active Supination

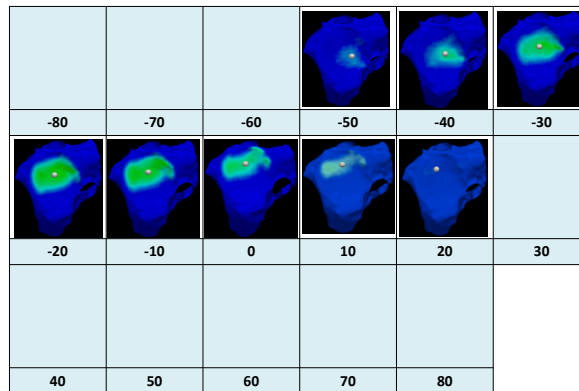| -80	-70	-60	-50	-40	-30
-20	-10	0	10	20	30
40	50	60	70	80	

Appendix 2. 37 11-12061L TFCC Dorsal Angulation 20° Active Supination © Braden Gammon

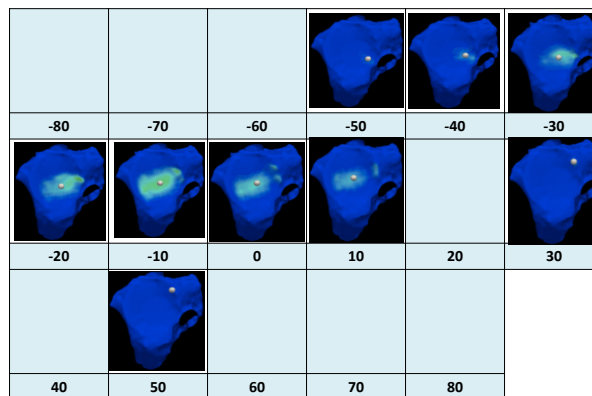11-12061L TFCC Dorsal Angulation 30 Degrees Active Supination

-80	-70	-60	-50	-40	-30
-20	-10	0	10	20	30
40	50	60	70	80	

Appendix 2. 38 11-12061L TFCC Dorsal Angulation 30° Active Supination © Braden Gammon

12-01004L Intact Active Supination

-80	-70	-60	-50	-40	-30
-20	-10	0	10	20	30
40	50	60	70	80	

Appendix 2. 39 12-01004L Intact Active Supination © Braden Gammon

12-01004L Intact Passive Supination

-80	-70	-60	-50	-40	-30
-20	-10	0	10	20	30
40	50	60	70	80	
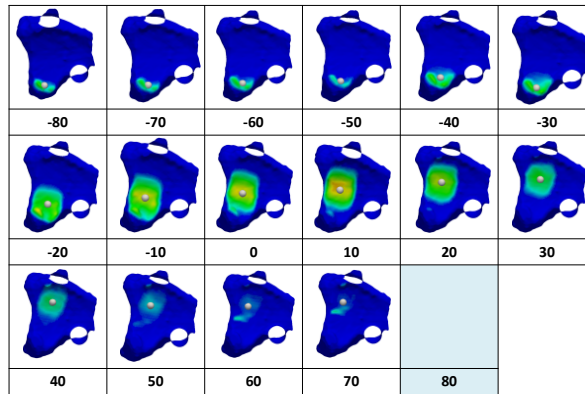
Appendix 2. 40 12-01004L Intact Passive Supination © Braden Gammon

12-01004L SW1 Active Supination

-80	-70	-60	-50	-40	-30
-20	-10	0	10	20	30
40	50	60	70	80	
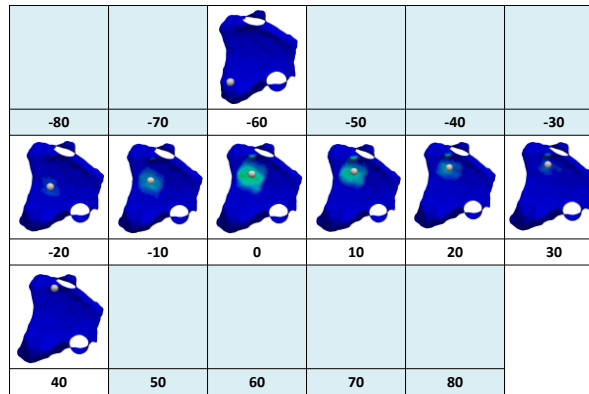
Appendix 2. 41 12-01004L SW1 Active Supination © Braden Gammon

12-01004L Dorsal Angulation 10 Degrees Active Supination

-80	-70	-60	-50	-40	-30
-20	-10	0	10	20	30
40	50	60	70	80	
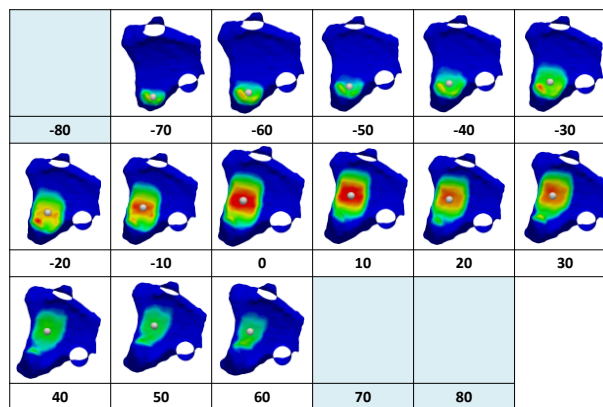
Appendix 2. 42 12-01004L Dorsal Angulation 10° Active Supination © Braden Gammon

12-01004L Dorsal Angulation 20 Degrees Active Supination

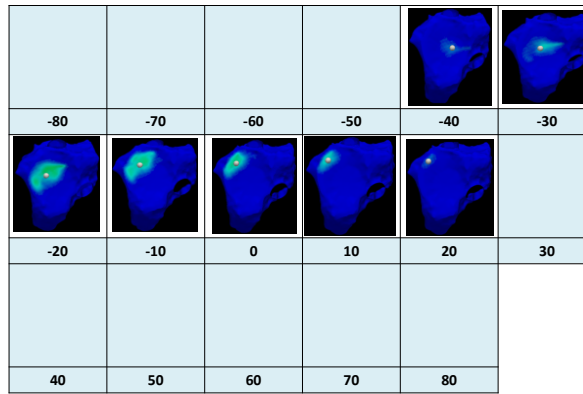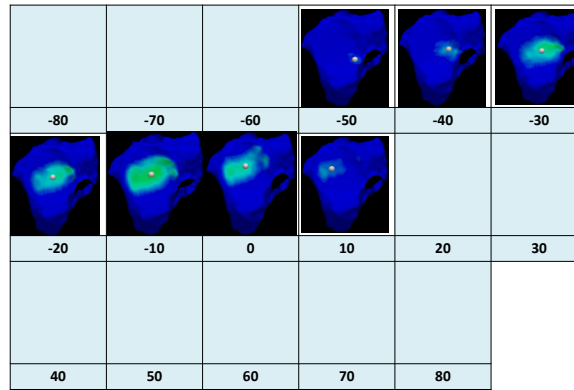| -80	-70	-60	-50	-40	-30
-20	-10	0	10	20	30
40	50	60	70	80	

Appendix 2. 43 12-01004L Dorsal Angulation 20° Active Supination © Braden Gammon

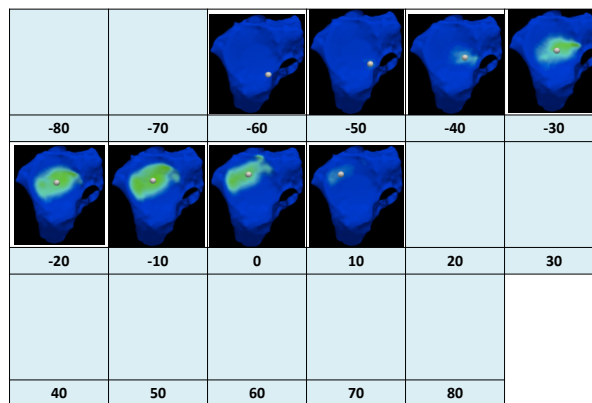**12-01004L** Dorsal Angulation 30 Degrees Active Supination

-80	-70	-60	-50	-40	-30
-20	-10	0	10	20	30
40	50	60	70	80	

Appendix 2. 44 12-01004L Dorsal Angulation 30° Active Supination © Braden Gammon

12-01004L TFCC SW1 Active Supination

-80	-70	-60	-50	-40	-30
-20	-10	0	10	20	30
40	50	60	70	80	

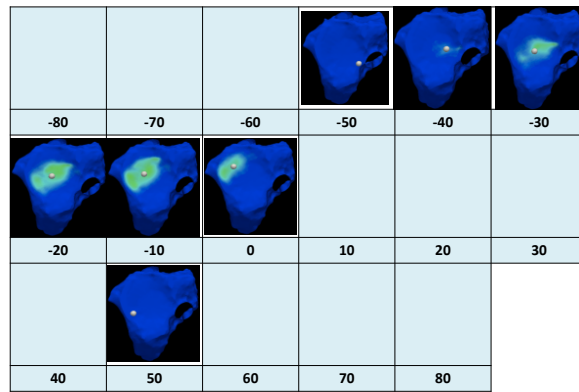**Appendix 2. 45 12-01004L** TFCC SW1 Active Supination © Braden Gammon

12-01004L TFCC Dorsal Angulation 10 Degrees Active Supination

-80	-70	-60	-50	-40	-30
-20	-10	0	10	20	30
40	50	60	70	80	

Appendix 2. 46 12-01004L TFCC Dorsal Angulation 10° Active Supination © Braden Gammon

12-01004L TFCC Dorsal Angulation 20 Degrees Active Supinated

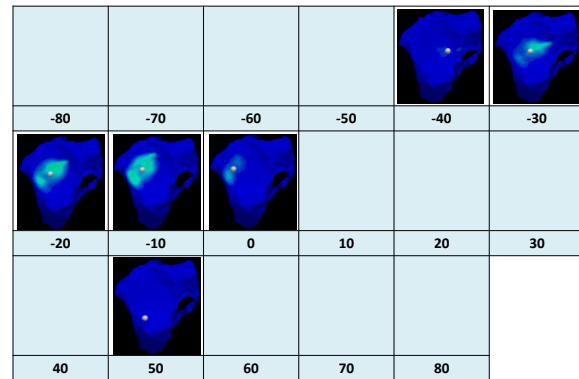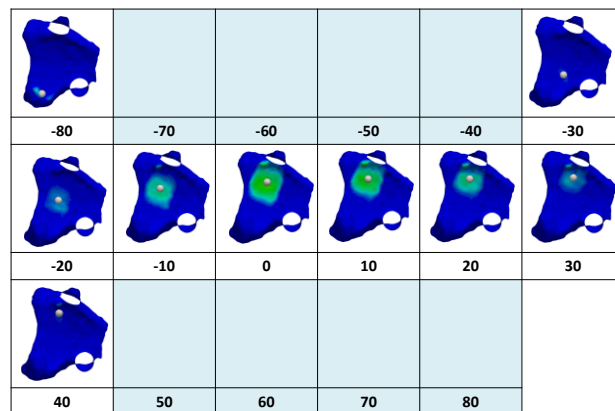| -80	-70	-60	-50	-40	-30
-20	-10	0	10	20	30
40	50	60	70	80	

Appendix 2. 47 12-01004L TFCC Dorsal Angulation 20° Active Supination © Braden Gammon

12-01004L TFCC Dorsal Angulation 30 Degrees Active Supinated

| -80	-70	-60	-50	-40	-30
-20	-10	0	10	20	30
40	50	60	70	80	

Appendix 2. 48 12-01004L TFCC Dorsal Angulation 30° Active Supination © Braden Gammon

12-01056L Intact Active Supination

-80	-70	-60	-50	-40	-30
-20	-10	0	10	20	30
40	50	60	70	80	

Appendix 2. 49 12-01056L Intact Active Supination © Braden Gammon

12-01056L Intact Passive Supination

-80	-70	-60	-50	-40	-30
-20	-10	0	10	20	30
40	50	60	70	80	

Appendix 2. 50 12-01056L Intact Passive Supination © Braden Gammon

12-01056L SW1 Active Supination

-80	-70	-60	-50	-40	-30
-20	-10	0	10	20	30
40	50	60	70	80	
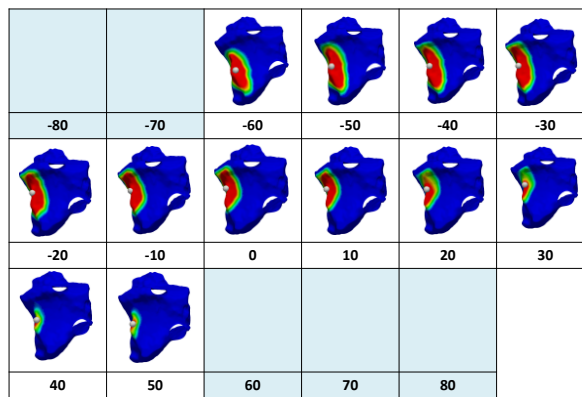
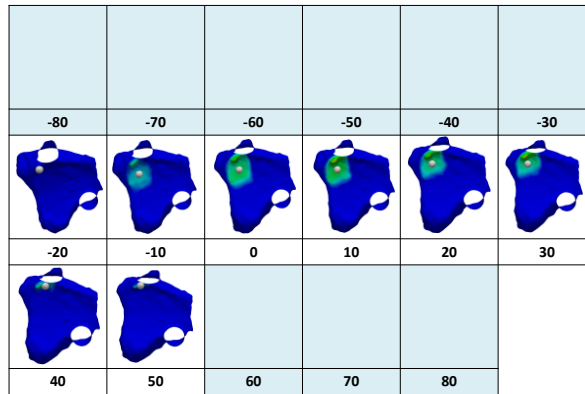**Appendix 2. 51 12-01056L SW1 Active Supination © Braden Gammon**

12-01056L Dorsal Angulation 10 Degrees Active Supination

-80	-70	-60	-50	-40	-30
-20	-10	0	10	20	30
40	50	60	70	80	
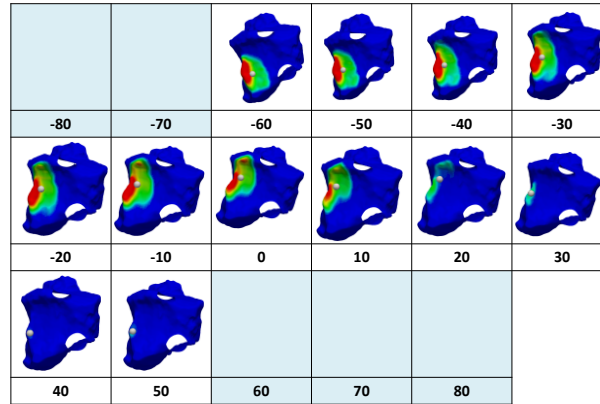
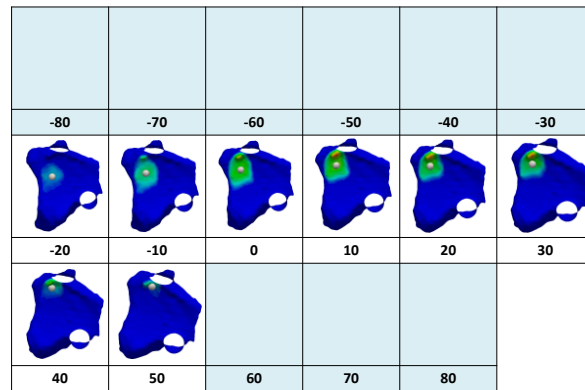**Appendix 2. 52 12-01056L Dorsal Angulation 10° Active Supination © Braden Gammon**

12-01056L Dorsal Angulation 20 Degrees Active Supination

-80	-70	-60	-50	-40	-30
-20	-10	0	10	20	30
40	50	60	70	80	

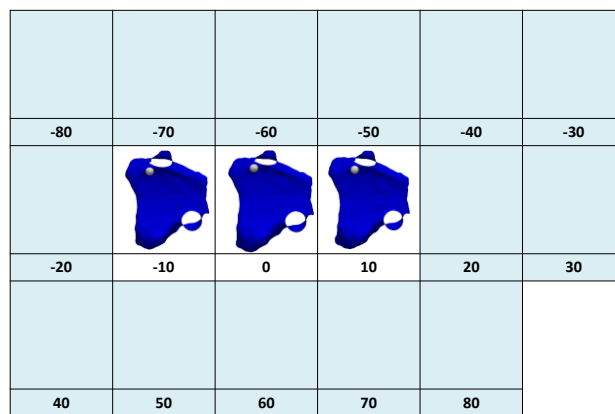**Appendix 2. 53 12-01056L Dorsal Angulation 20° Active Supination © Braden Gammon**

12-01056L Dorsal Angulation 30 Degrees Active Supination

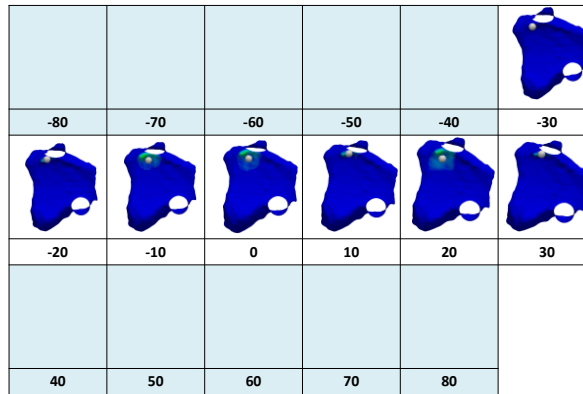|					
-80	-70	-60	-50	-40	-30
-20	-10	0	10	20	30
40	50	60	70	80	

Appendix 2. 54 12-01056L Dorsal Angulation 30° Active Supination © Braden Gammon

12-01056L TFCC SW1 Active Supination

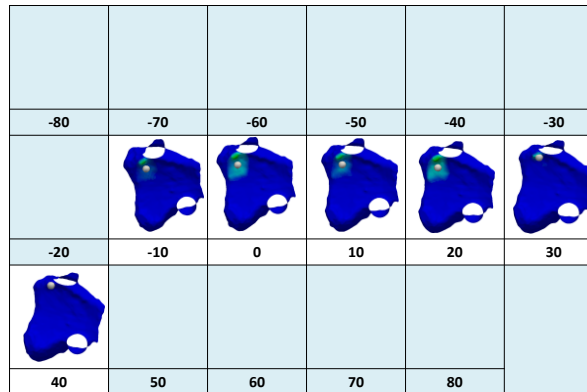|					
-80	-70	-60	-50	-40	-30
-20	-10	0	10	20	30
40	50	60	70	80	

Appendix 2. 55 12-01056L TFCC SW1 Active Supination © Braden Gammon

12-01056L TFCC Dorsal Angulation 10 Degrees Active Supination

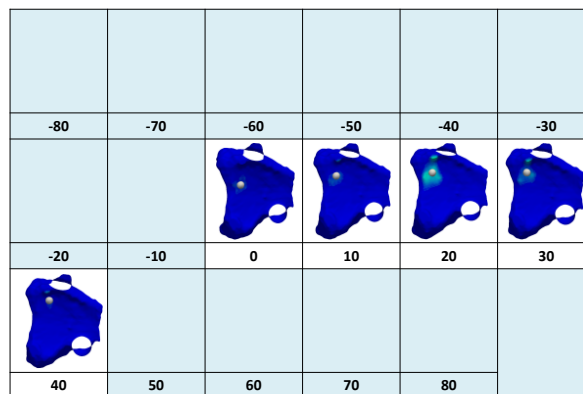|					
-80	-70	-60	-50	-40	-30
-20	-10	0	10	20	30
40	50	60	70	80	

Appendix 2. 56 12-01056L TFCC Dorsal Angulation 10° Active Supination © Braden Gammon

12-01056L TFCC Dorsal Angulation 20 Degrees Active Supinated

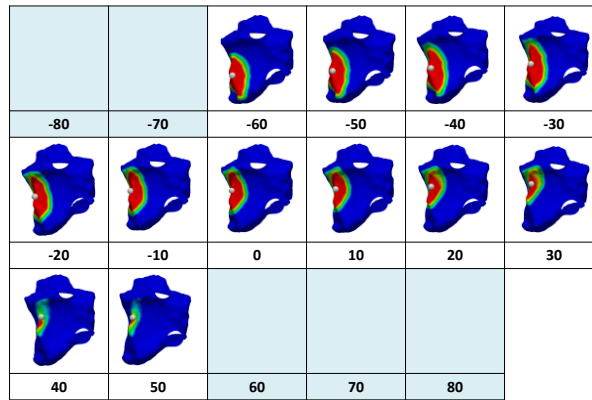|					
-80	-70	-60	-50	-40	-30
-20	-10	0	10	20	30
40	50	60	70	80	

Appendix 2. 57 12-01056L TFCC Dorsal Angulation 20° Active Supination © Braden Gammon

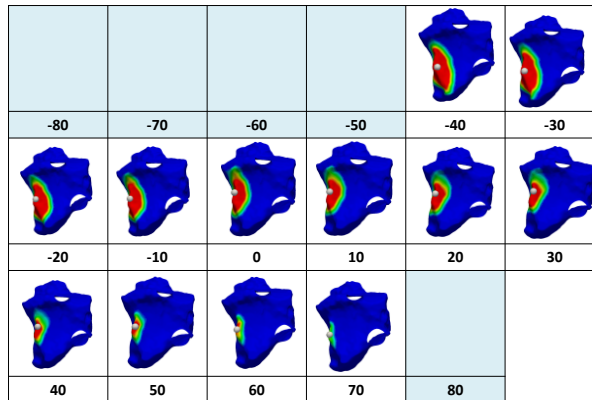12-01056L TFCC Dorsal Angulation 30 Degrees Active Supinated

-80	-70	-60	-50	-40	-30
-20	-10	0	10	20	30
40	50	60	70	80	

Appendix 2. 58 12-01056L TFCC Dorsal Angulation 30° Active Supination © Braden Gammon

12-06067L Intact Active Supination

|					
-80	-70	-60	-50	-40	-30
-20	-10	0	10	20	30
40	50	60	70	80	

Appendix 2. 59 12-02067L Intact Active Supination © Braden Gammon

12-06067L Intact Passive Supination

-80	-70	-60	-50	-40	-30
-20	-10	0	10	20	30
40	50	60	70	80	
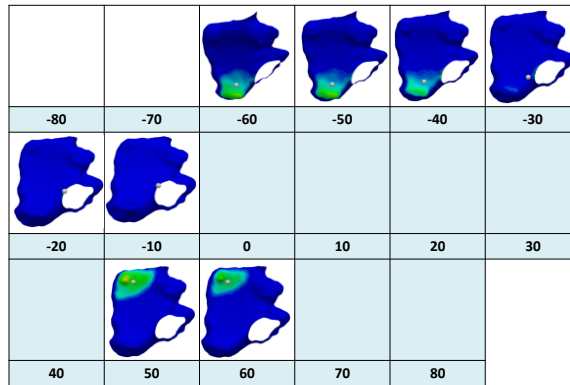
Appendix 2. 60 12-02067L Intact Passive Supination © Braden Gammon

12-06067L SW1 Active Supination

-80	-70	-60	-50	-40	-30
-20	-10	0	10	20	30
40	50	60	70	80	
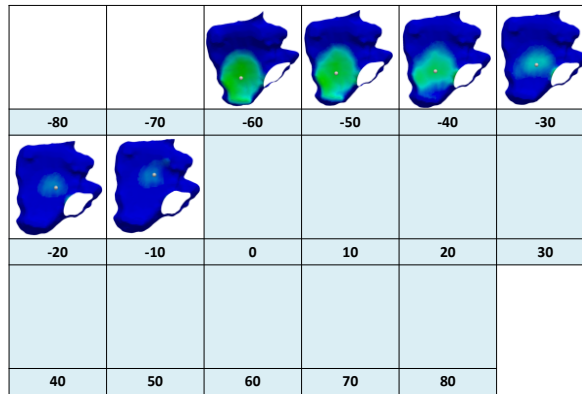
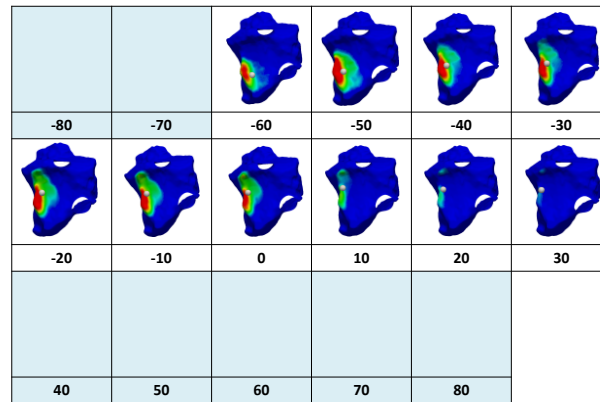**Appendix 2. 61 12-02067L SW1 Active Supination © Braden Gammon**

12-06067L Dorsal Angulation 10 Degrees Active Supination

-80	-70	-60	-50	-40	-30
-20	-10	0	10	20	30
40	50	60	70	80	
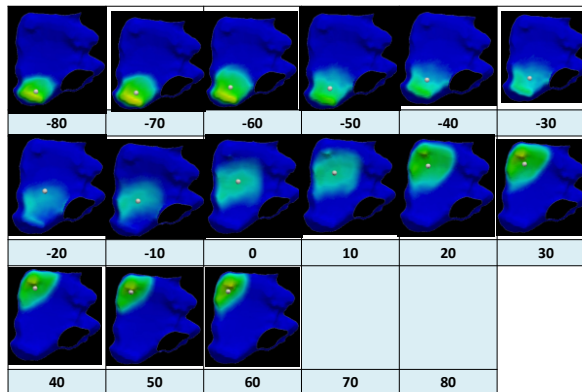
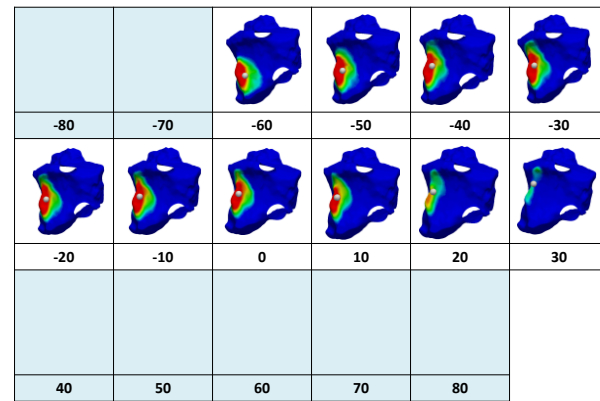**Appendix 2. 62 12-02067L Dorsal Angulation 10° Active Supination © Braden Gammon**

12-06067L Dorsal Angulation 20 Degrees Active Supination

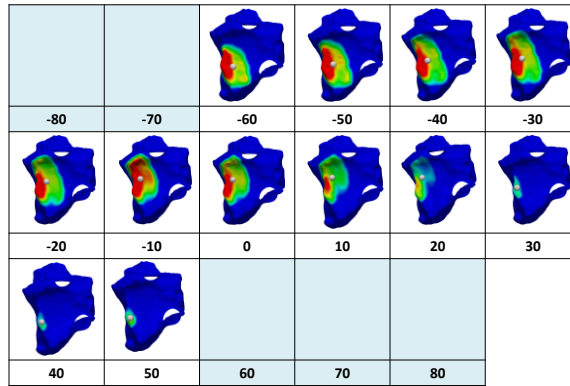|					
-80	-70	-60	-50	-40	-30
-20	-10	0	10	20	30
40	50	60	70	80	
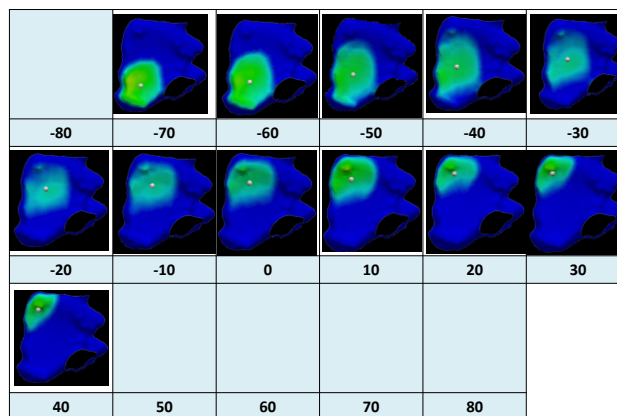
Appendix 2. 63 12-02067L Dorsal Angulation 20° Active Supination © Braden Gammon
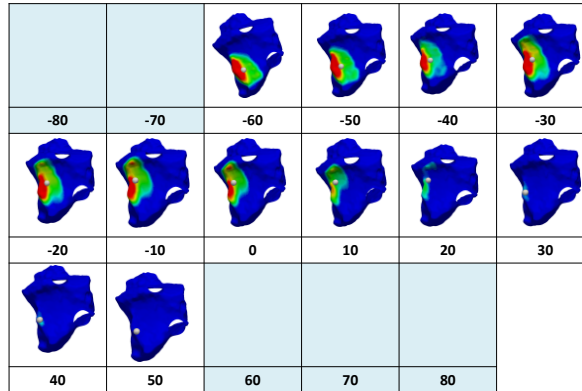
12-06067L Dorsal Angulation 30 Degrees Active Supination

-80	-70	-60	-50	-40	-30
-20	-10	0	10	20	30
40	50	60	70	80	

Appendix 2. 64 12-02067L Dorsal Angulation 30° Active Supination © Braden Gammon

12-06067L TFCC SW1 Active Supination

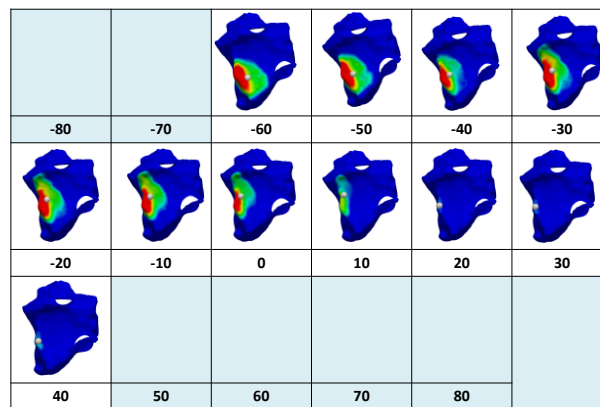| -80	-70	-60	-50	-40	-30
-20	-10	0	10	20	30
40	50	60	70	80	

Appendix 2. 65 12-02067L TFCC SW1 Active Supination © Braden Gammon

12-06067L TFCC Dorsal Angulation 10 Degrees Active Supination

-80	-70	-60	-50	-40	-30
-20	-10	0	10	20	30
40	50	60	70	80	

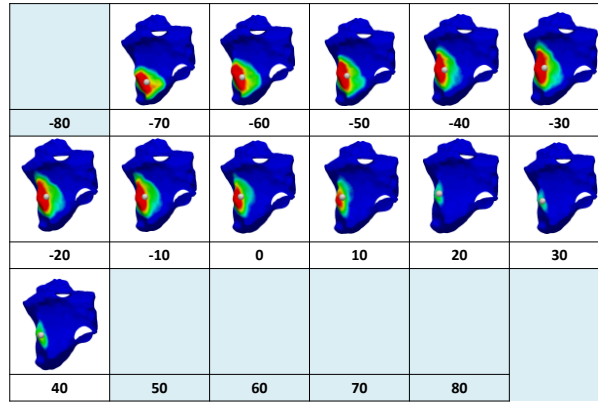**Appendix 2. 66 12-02067L** TFCC Dorsal Angulation 10° Active Supination © Braden Gammon

TFCC Dorsal Angulation 20 Degrees Active Supination

-80	-70	-60	-50	-40	-30
-20	-10	0	10	20	30
40	50	60	70	80	

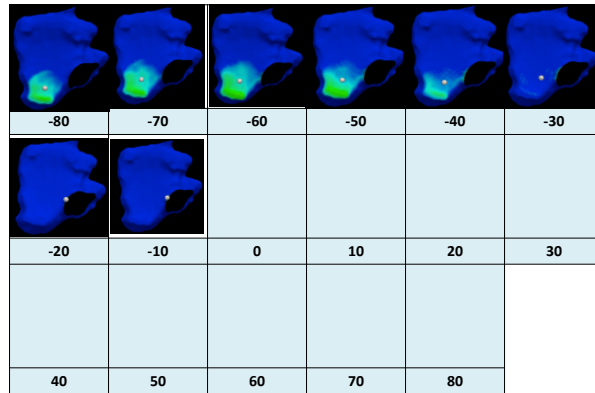**Appendix 2. 67 12-02067L** TFCC Dorsal Angulation 20° Active Supination © Braden Gammon

TFCC Dorsal Angulation 30 Degrees Active Supination

|					
-80	-70	-60	-50	-40	-30
-20	-10	0	10	20	30
40	50	60	70	80	

Appendix 2. 68 12-02067L TFCC Dorsal Angulation 30° Active Supination © Braden Gammon

Intact Active Supination

-80	-70	-60	-50	-40	-30
-20	-10	0	10	20	30
40	50	60	70	80	

Appendix 2. 69 12-09013L Intact Active Supination © Braden Gammon

12-09013L Intact Passive Supination

-80	-70	-60	-50	-40	-30
-20	-10	0	10	20	30
40	50	60	70	80	

Appendix 2. 70 12-09013L Intact Passive Supination © Braden Gammon

12-09013L SW1 Active Supination

-80	-70	-60	-50	-40	-30
-20	-10	0	10	20	30
40	50	60	70	80	
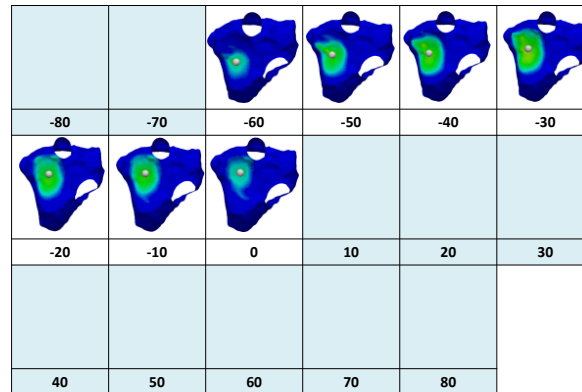
Appendix 2. 71 12-09013L SW1 Active Supination © Braden Gammon

12-09013L Dorsal Angulation 10 Degrees Active Supination

-80	-70	-60	-50	-40	-30
-20	-10	0	10	20	30
40	50	60	70	80	
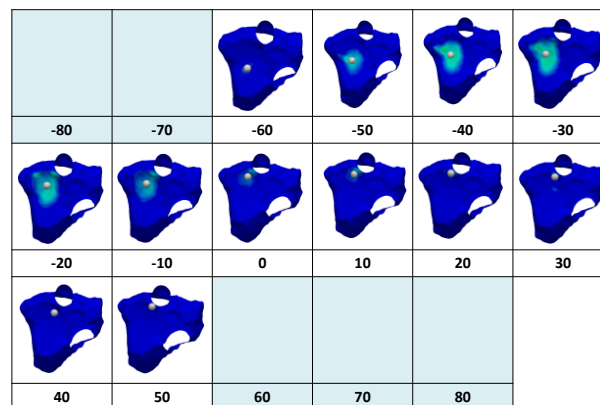
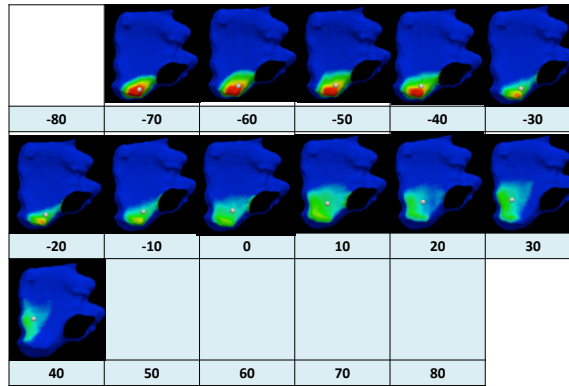**Appendix 2. 72 12-09013L** Dorsal Angulation 10° Active Supination © Braden Gammon

12-09013L Dorsal Angulation 20 Degrees Active Supination

-80	-70	-60	-50	-40	-30
-20	-10	0	10	20	30
40	50	60	70	80	
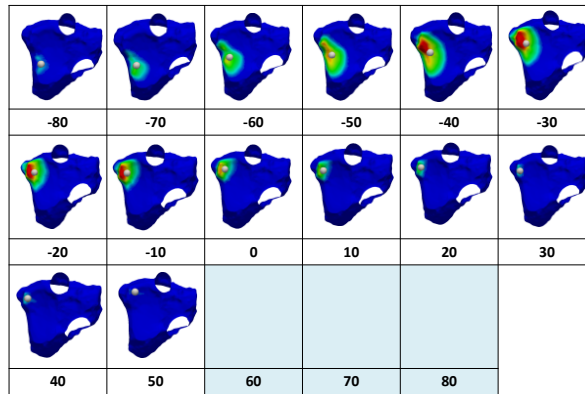
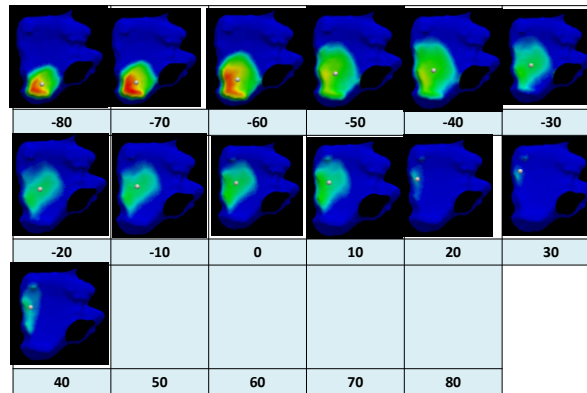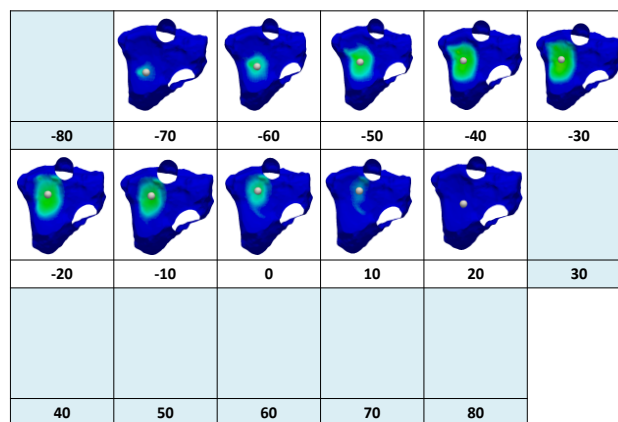**Appendix 2. 73 12-09013L** Dorsal Angulation 20° Active Supination © Braden Gammon

12-09013L Dorsal Angulation 30 Degrees Active Supination

-80	-70	-60	-50	-40	-30
-20	-10	0	10	20	30
40	50	60	70	80	

Appendix 2. 74 12-09013L Dorsal Angulation 30° Active Supination © Braden Gammon

12-09013L TFCC SW1 Active Supination

-80	-70	-60	-50	-40	-30
-20	-10	0	10	20	30
40	50	60	70	80	

Appendix 2. 75 12-09013L TFCC SW1 Active Supination © Braden Gammon

12-09013L TFCC Dorsal Angulation 10 Degrees Active Supination

-80	-70	-60	-50	-40	-30
-20	-10	0	10	20	30
40	50	60	70	80	

Appendix 2. 76 12-09013L TFCC Dorsal Angulation 10° Active Supination © Braden Gammon

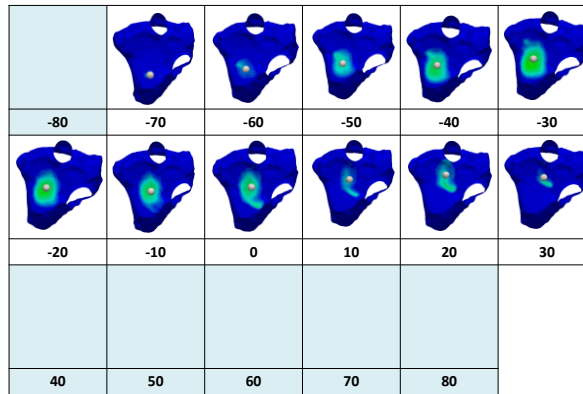**12-09013L** TFCC Dorsal Angulation 20 Degrees Active Supinated

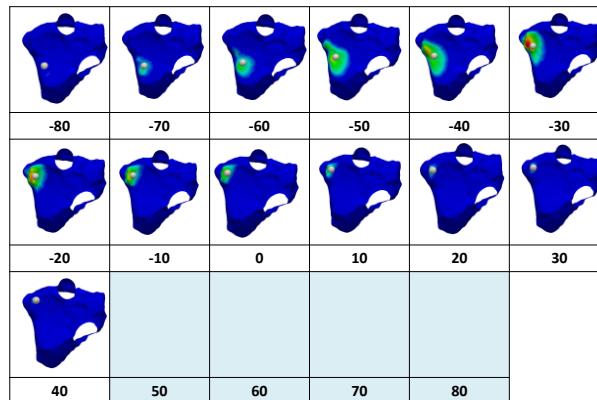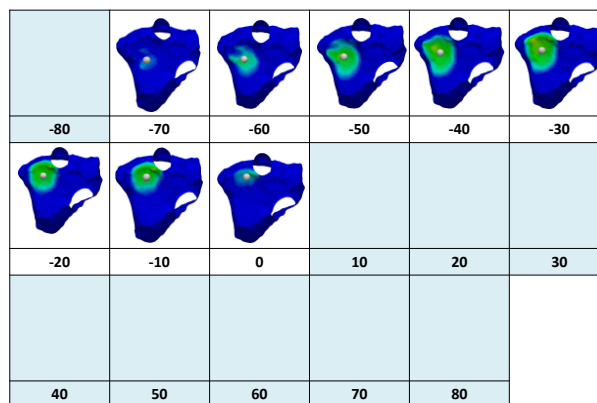| -80	-70	-60	-50	-40	-30
-20	-10	0	10	20	30
40	50	60	70	80	
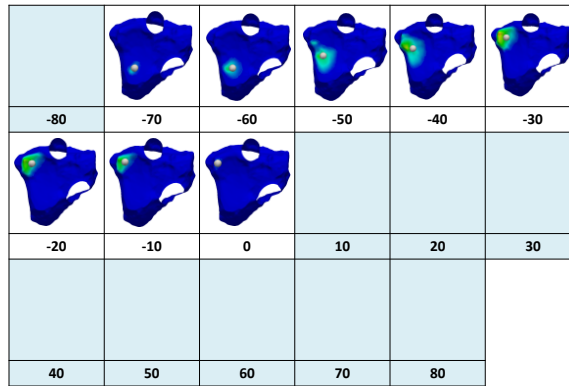
Appendix 2. 77 12-09013L TFCC Dorsal Angulation 20° Active Supination © Braden Gammon

12-09013L TFCC Dorsal Angulation 30 Degrees Active Supinated
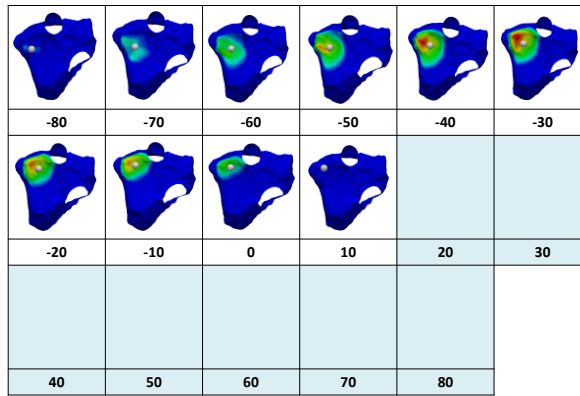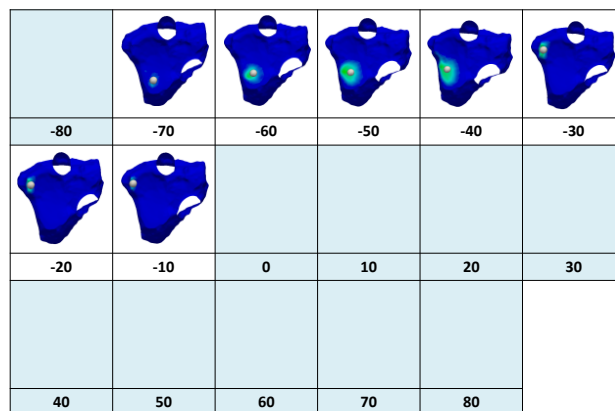

-80	-70	-60	-50	-40	-30
-20	-10	0	10	20	30
40	50	60	70	80	

Appendix 2. 78 12-09013L TFCC Dorsal Angulation 30° Active Supination © Braden Gammon

Dr. Braden Gammon, MD FRCS(C)
Assistant Professor, University of Ottawa
Hand and Wrist Surgery

EDUCATION

- **Master of Science (candidate), Medical Biophysics**   2012-2016
  Supervisors: Dr. Graham King, Dr. Jim Johnson
- **Hand and Upper Extremity Fellowship**   2012-2014
  Roth-McFarlane Hand and Upper Limb Center, London ON
- **Hand and Upper Extremity Fellowship**   2011-2012
  Queen's University, Kingston ON
- **Orthopedic Surgery Residency Program**   2006-2011
  Queen's University, Kingston ON
- **Doctor of Medicine (Graduate with Honors)**   2002-2006
  University of Toronto, Toronto ON
- **Bachelor of Science Program (3 of 4 years)**   1999-2002
  Faculty of Biology, Acadia University, Wolfville NS

AWARDS

- Best Basic Science Research Paper, William Ersil Resident   2009
  Research Day
- PAIRO Award for Excellence in Teaching Nominee   2008
- University of Toronto Wightman-Berris Golden   2006
  Stethoscope Award
- Honors Standing Years 1-4: Faculty of Medicine,   2002-2006
  University of Toronto

PUBLICATIONS

Peer Reviewed Articles:
- Nishiwaki M, Welsh MF, **Gammon B**, Ferreira LM, Johnson JA, King GJ. "Effect of Volarly Angulated Distal Radius Fractures on Forearm Rotation and Distal Radioulnar Joint Kinematics". Journal of Hand Surgery American. 2015 Nov;40(11):2236-42.
- Nishiwaki M, Welsh M, **Gammon B**, Ferreira LM, Johnson JA, King GJ. "Volar Subluxation of the Ulnar Head in Dorsal Translation Deformities of Distal Radius Fractures: An In-Vitro Biomechanical Study". Journal of Orthopedic Trauma. 2015 Jun;29(6):295-300.
- Nishiwaki M, Welsh M, **Gammon B**, Ferreira L, Johnson J, King G. "Distal Radioulnar Joint Kinematics in Simulated Dorsally Angulated Distal Radius Fractures". Journal of Hand Surgery American. 2014 April; 39(4):656-63.
- Ma B, Kunz M, **Gammon B**, Ellis R, Pichora D. "A Laboratory Comparison of Computer Navigation and Individualized Guides for Distal Radius Osteotomy".

International Journal of Computer Assisted Radiology and Surgery. 2014 July; 9(4):713-24.

- Smith EJ, Al-Sanawi HA, **Gammon B**, Ellis RE, Pichora DR. "Volume rendering of 3D fluoroscopic images for percutaneous scaphoid fixation: An in vitro study". Journal of Engineering in Medicine. 2013 April; 227(4):384-92.
- Smith EJ, Allan G, **Gammon B**, Sellens R, Ellis RE, Pichora DR. "Investigating the performance of a wrist-stabilization device for image-guided percutaneous scaphoid fixation". International Journal of Computer Assisted Radiology and Surgery. 2014 March; 9(2):155-64.
- **Gammon B**, Bicknell R. "Upper Extremity Blocks in Orthopaedic Surgery". Canadian Orthopedic Association Bulletin. 2012 Spring; 96: 25-26.
- Smith EJ, Al-Sanawi HA, **Gammon B**, St John PJ, Pichora DR, Ellis RE. "Volume Slicing of Cone-beam Computed Tomography Images for Navigation of Percutaneous Scaphoid Fixation". International Journal of Computer Assisted Radiolology and Surgery. 2012 May; 7(3): 433-44.
- Smith EJ, Oentoro A, Al-Sanawi H, **Gammon B**, St John P, Pichora DR, Ellis RE. Calibration and use of intraoperative cone-beam computed tomography: an in-vitro study for wrist fracture. Med Image Comput Comput Assist Interv. 2010;13 (Pt 3):359-66.

Book Chapters:

- **Gammon B**, Bicknell R. Athwal G. "Physical Examination of the Shoulder and Elbow". In *AAOS Comprehensive Review Guide, 2nd Ed*. Edited by Boyer M, Rosemont IL, 2014.
- **Gammon B**, King G. "Complications in Elbow Arthroscopy". In *ISAKOS Elbow Arthoscopy Booklet*. Edited by Pederzini L, Toronto: Springer, 2013.
- **Gammon B**, Orner A and Sue S. "Orthopaedics". In *The Toronto Notes 2006: MCCQE Review Notes & Lecture Series, 22nd ed*. Edited by Shiau C and Torren A, Toronto: Type and Graphics, 2006.

INVITED PRESENTATIONS

"Distal Radius Fracture Update" **B Gammon**. National Capital Orthopedic Association Annual Meeting. Montebello, QC.	2015
"Humerus Fractures" and "Carpal Fractures/Dislocations" **Gammon B**. Canadian Orthopaedic Resident Trauma Course, Kingston ON.	2012
"Managing Proximal Humeral Bone Loss in Reverse Total Shoulder Arthroplasty" **Gammon B,** Bicknell R. Association of Clinical Elbow and Shoulder Surgeons Annual Meeting, Palm Beach FL.	2011
"Upper Extremity Tumors: Principles of Diagnosis and Treatment" **Gammon B**. Queen's University Orthopedic QCare Conference, Kingston ON.	2011
"Long Head of Biceps Pathology: Tips and Tricks" **Gammon B,** Bicknell R. Canadian Orthopedic Association Annual Meeting, St. John's Nfld.	2011
"An Introduction to Fractures and How to Fix Them"	2009

Gammon B. Human Mobility Research Center Seminar Series, Kingston ON.

- "An Assessment of Sport-Specific Educational Deficits and Their Impact on Young Baseball Players" **B Gammon**, E Boynton. University of Toronto Community Health Seminar Series, Toronto ON.   2004

CURRENT RESEARCH

- "Design and validation of a novel Distal Radioulnar Joint Arthrometer for the assessment of in vivo translation and instability" **B Gammon**, Louati H, D'Sa H.   2014-present
- "The Effects of Multiplanar Distal Radius Fractures on DRUJ Arthrokinematics using Intercartilage Distance" **Gammon B**, E Lalone, Willing R Nishiwaki M, Johnson J, King G   2012-present
- "The Effects of Multiplanar Distal Radius Fractures on Carpal Kinematics" Nishiwaki M, Welsh M, **Gammon B,** Ferreira L, Johnson J, King G   2012-present
- " The Effect of Radial Head Excision on Ulnohumeral Joint Forces and Kinematics" Ng J, **Gammon B**, Nishiwaki M, Athwal GS, Johnson J, King G   2012-present

COURSES ATTENDED

- National Capital Orthopedic Association, Montebello QC   • 2015
- ASSH Annual Meeting, Seattle   • 2015
- Interagency Advisory Panel on Research Ethics: Introduction to the Tricouncil Policy Statement: Ethical Conduct for Research Involving Human Subjects 2 (TCPS)   • 2015
- ASSH Annual Meeting, Boston   • 2014
- ASSH Annual Meeting, San Francisco   • 2013
- Mayo Clinic Disorders of the Wrist, Rochester MN   • 2013
- Mayo Clinic Microvascular Surgery Skills Training Course, Rochester MN   • 2013
- Philadelphia Hand Surgery Symposium, Philadelphia PA   • 2013
- Arthrex Hand and Wrist Fellow's Course, Naples FL   • 2012
- Joints Canada Shoulder Course, Montreal QC   • 2012
- COA Annual Meeting, St. John's NF   • 2011
- Canadian Orthopedic Resident Forum, Calgary AB   • 2011
- Ste. Justine Pediatric Review Course, Montreal QC   • 2011
- CORR Trauma Review Course, Toronto ON   • 2010
- AO Pelvic and Acetabular Fracture Management Course,   • 2010
- Toronto ON   •
- Canadian Orthopedic Residents Trauma Course, Kingston ON   • 2010
- COA Basic Science Course, Winnipeg MB   • 2009
- American Academy of Orthopedic Surgeons (AAOS) Annual Meeting, Las Vegas NV   • 2008
- COA Annual Meeting, Halifax NS   • 2008

• University of Toronto Upper Limb Update, Toronto ON	• 2008
• University of Toronto Foot and Ankle Update, Toronto ON	• 2007
• AO Basic Fracture Course	• 2007
• Advanced Trauma Life Support (ATLS)	• 2006
• Advanced Cardiac Life Support (ACLS)	• 2006

PROFESSIONAL MEMBERSHIPS

• Royal College of Physicians and Surgeons of Canada	2011-present
• College of Physicians and Surgeons of Ontario	2006-present
• Canadian Orthopedic Association	2006-present
• Canadian Medical Association	2002-present
• Ontario Medical Association	2002-present
• American Society for Surgery of the Hand – Candidate Member	2011-present
• American Academy of Orthopedic Surgeons	2006-present

COMMITTEES AND POST-GRADUATE TEACHING EXPERIENCE

• Hand and Wrist Rotation Director, Division of Orthopedics	2014-present
• Resident Training Committee Member, Division of Orthopedics	2015-present 2014-present
• Resident Mentorship Program, Division of Orthopedics	2014-present
• Hand Rounds Co-Chair, Division of Plastic and Orthopedic Surgery	2015-present
• OR Efficiency Committee, Riverside Campus, The Ottawa Hospital	2014-present
• LINK Student Supervisor, Department of Surgery	2014-present
• Undergraduate Surgical Education Committee, Department of Surgery	2014-present
• Associate Orthopedic Surgeon (occasional coverage): Ottawa Senators, National Hockey League Players Association	2014
• CUSP Committee, Riverside Campus, The Ottawa Hospital	
• Clinical Clerk Casting Seminar, *University of Western Ontario*	2012
• Canadian Orthopedic Resident Trauma Course 2012: Table Instructor, *Queen's University*	2012
• Clinical Clerk Expanded Clinical Skills Seminar: Examining the Upper Extremity, *Queen's University*	2012
• Canadian Orthopedic Resident Trauma Course 2011: Table Instructor, *Queen's University*	2011
• Clinical Clerk Seminar Series: Hand Surgery, *Queen's University*	2011
• Family Medicine Casting Seminar, *Queen's University*	2010-2011

Conference Presentations

- Canadian Orthopedic Association Annual Meeting (COA) Quebec City 2016 (podium)

Title: The Effect of Radial Head Resection on Load Transfer in the Ulnohumeral Joint: An Experimental Biomechanical Study
Authors: Jennifer Ng, Masao Nishiwaki, Braden Gammon, George Athwal, Graham King, James Johnson

- Canadian Orthopedic Association Annual Meeting (COA) Quebec City 2016 (podium)

Title: The Effect of Muscle Loading and Forearm Rotation on Distal Radioulnar Joint Cartilage Contact Mechanics
Authors: Braden Gammon, Emily Lalone, Ryan Willing, Masao Nishwaki, Graham King, James Johnson

- Orthopedic Research Society (ORS) Orlando FL, 2016 (podium)

Title: Carpal Kinematics During Simulated Wrist Motion
Authors: Helen Stoesser, Clare Padmore, Masao Nishiwaki,Braden Gammon, Emily Lalone, Dan Langohr, Graham King, James Johnson.

- Orthopedic Research Society (ORS) Orlando FL, 2016 (podium)

Title: The Effects of Distal Radius Deformities on Wrist Kinematics - An In-vitro Biomechanical Study
Authors: Clare Padmore, Helen Stoesser, Masao Nishiwaki, Braden Gammon, Dan Langohr, Emily Allen Lalone, James A. Johnson, Graham King

- American Society for Surgery of the Hand Annual Meeting (ASSH) Seattle 2015 (e-poster)

Title: Distal radioulnar joint kinematics in simulated volarly angulated distal radius fractures
Authors: Masao Nishiwaki, Mark Welsh, Braden Gammon, Louis M. Ferreira, James A. Johnson, Graham J.W. King

- Canadian Orthopedic Association Annual Meeting (COA) Vancouver 2015 (poster)

Title: The Effect of Active and Passive Flexion on Elbow Joint Loading
Authors: Jennifer Ng, Masao Nishiwaki, Braden Gammon, Mark Welsh, George Athwal, Graham King, James Johnson.

- International Wrist Investigator's Workshop (podium)

Title: The Effect of Volarly Angulated Distal Radius Fractures on Forearm Rotation: *In Vitro* Biomechanical Study
Authors: Masao Nishiwaki, Mark Welsh, Braden Gammon, Louis M. Ferreira, James A. Johnson, Graham J.W. King

- American Society for Surgery of the Hand Annual Meeting (ASSH) Boston 2014 (e-poster)

Title: The Effect of Dorsal Translation in Dorsally Angulated Distal Radius Fractures on Distal Radioulnar Joint Kinematics
Authors: Masao Nishiwaki, Mark Welsh, Braden Gammon, Louis Ferreira, James Johnson, Graham King

- Orthopedic Research Society (ORS) New Orleans 2014/ASES Combined Meeting (Poster)

Title: The Effect of Muscle Activation and Joint Position on Elbow Joint Forces
Authors: Jennifer Ng, Masao Nishiwaki, Braden Gammon, Mark Welsh, George Athwal,

Graham King, James Johnson.
- Japanese Orthopedic Association Annual Meeting (JOA) 2014 (Podium)

Title: Distal Radioulnar Joint Kinematics in Simulated Dorsally Angulated and Translated Distal Radius Fractures
Authors: Masao Nishiwaki, Mark Welsh, Braden Gammon, Louis Ferreira, James Johnson, Graham King
- Canadian Orthopedic Association Annual Meeting (COA) 2012 (Poster)

Title: Navigation of guidewire placement using volume slicing of 3D cone-beam computed tomography (CBCT) images for percutaneous scaphoid fixation
Authors: Erin Smith, Hesham Al-Sanawi, Braden Gammon, Paul St John, David Pichora, Randy Ellis.
- Canadian Orthopedic Association Annual Meeting (COA) 2011 (Poster)

Title: Percutaneous Scaphoid Fixation using Computer-assisted Navigation with Intraoperatively-acquired Images
Authors: Hesham Al-Sanawi, Braden Gammon, Rick Sellens, Paul St. John, Erin Smith, David Pichora, Randy Ellis.